Technische Universität München

Physik Department

Theoretische Physik T37

Polyelectrolytes in Electric Fields

Sebastian Fischer

Vollständiger Abdruck der von der Fakultät für Physik der Technischen Universität München zur Erlangung des akademischen Grades eines

Doktors der Naturwissenschaften (Dr. rer. nat.)

genehmigten Dissertation.

Vorsitzender:		Univ.-Prof. Dr. F. Simmel
Prüfer der Dissertation:	1.	Univ.-Prof. Dr. R. Netz
	2.	Univ.-Prof. Dr. M. Zacharias

Die Dissertation wurde am 08. 10. 2009 bei der Technischen Universität München eingereicht und durch die Fakultät für Physik am 10. 11. 2009 angenommen.

Contents

1. Introduction

Polyelectrolytes (PEs) are polymers bearing ionizable groups that dissociate when dissolved in a polar solvent [1]. The resultant charges on the PE chains are neutralized by released counterions which distribute in the solution. Both the complex conformation of the PE chains as well as the spatial arrangement of the counterions is determined by a delicate balance of energy an entropy. In this connection, the relevant energy scale of the order of thermal energy $k_B T$ entails high sensitivity of PE solutions to weak external perturbations paradigmatic for soft matter systems [2, 3].

PEs are water soluble. Within industrial applications this allows for cheap, non-toxic and environment friendly polymer processing. A prominent example illustrating the hydrophilicity of PEs are supersorbers based on cross-linked polyacrylic acid, a synthetic PE. In baby diapers the liquid uptake of such polyacrylic acid-based PE networks amounts to 30 times their own weight [4]. Another sample application is the solubilization of β-carotin using gelatin, a biological PE, as a coating [5]. Suspended β-carotin particles lend the yellow color to a number of popular soft-drinks. Further industrial applications use PEs as thickeners, gelling agents, flocculants, glues and coatings, among others [1].

Apart from their industrial importance, PEs play an outstanding role as building blocks of biological matter. With actin filaments, intermediate filaments, and microtubules, the three major components of the eukaryotic cytosceleton are protein-based PEs. Their PE character turns out to be essential for non-specific electrostatic binding of associated proteins, for instance kinesin binding to microtubules [6]. Even more vital in its double sense is the PE nature of DNA [7]. In case of double-stranded DNA, dissociation of the phosphate groups gives rise to a linear charge density of 1 e/0.17 nm, one of the highest linear charge densities found in nature! DNA interacts sensitively with its ionic environment. In contrast to physiological conditions where DNA takes on a random-coil configuration, DNA condenses into a toroidal shape in the presence of multivalent ions. Electrostatics govern the unspecific binding of DNA-associated proteins, e.g. repressor proteins, to the DNA backbone, and the wrapping of DNA around oppositely charged histones.

PE dynamics can be controlled by external electric fields. This rather trivial statement conveys sheer inexhaustible possibilities for the electric manipulation of PE materials. For example, upon application of an external electric field a PE gel can undergo a more than 100-fold volume change [8], the wetting properties of a PE coated surface can be varied from hydrophilic to hydrophobic [9], and the contrast of an electrophoretic display (so called e-paper) can be switched [10]. On a more basic level, the response of a PE solution under the action of an electric field allows for the characterization of its constituents. In this connection, two set-ups are of importance: *Electrophoresis* is a working horse for the characterization of PEs with respect to their migration speed subject to a static electric field, with a broad range of applicability in biology, chemistry, medicine, pharmaceutics, physics and related subjects. For instance, electrophoresis made a decisive contribution to the deciphering of the human genome [11]. *Dielectric spectroscopy* permits non-invasive characterization of PE solutions with respect to their frequency dependent polarizability in an alternating electric field. In principle, from the dielectric spectrum information about the conformation of individual PE chains as well as the structure of the PE solution can be obtained.

While the engineering aspect of PE solutions in static or alternating electric fields is highly developed, understanding is still limited from a theoretical physics point of view. This limitation is due to the long-range nature of electrostatic and hydrodynamic interactions coupling the dynamics of PE chains and counterions in an intricate fashion. As a consequence, only partial success can be ascribed to analytical approaches which, moreover, are restricted to simple model systems. Today, in view of the growing availability of large-scale computing facilities, computer simulations present a valuable approach to the response of PE solutions in electric fields, which becomes apparent in an increasing number of related.

Outline

The aim of the present thesis is to gain new insights into PE dynamics in external electric fields by means of mesoscale Brownian Dynamics (BD) simulations and analytical calculations. Mesoscale simulations provide a powerful tool to bridge the gap between microscopic time and length scales covered by atomistic Molecular Dynamics (MD) simulations and the relevant time and length scales of industrial and biological processes. With regard to PE solutions, atomistic details of PE chains and counterions are abandoned in favor of a coarse-grained effective description. Where hydrodynamic interactions are

important, smart solvent models have to be applied in order to keep the computational cost at reasonable level. Within BD simulations this can be accomplished using an efficient implicit solvent model which introduces long-range correlations in the equations of motion [12]. The BD simulations technique has successfully been applied in connection with static [13–15] and dynamic [16–19] properties of PE solutions.

Throughout this thesis we address two main subjects: (1) the dielectric response of salt-free PE solutions in Chapter 3 and (2) the electrophoretic response of salt-free and salt-containing PE solutions in Chapters 4, 5, and 6. Thereby, special emphasis is put on the counterion dynamics which is crucial for the understanding of either phenomenon. The so-called *counterion condensation* at strongly charged PEs divides the counterion distribution around a PE chain into tightly bound *condensed counterions* and loosely bound *uncondensed counterions*. These two counterion populations not only differ with respect to their static properties but also with respect to their dynamics. We use a coarse-grained description for the PE solution, where PE monomers and ions are represented as charged spheres. The BD simulation technique shortly reviewed in Chapter 2 is our method of choice for the calculation of PE and ion dynamics. Complementary scaling arguments and analytical calculations are provided, which add to the interpretation of our simulation results.

To our knowledge, the simulations of the dielectric response of flexible PE chains in salt-free solution presented in Chapter 3 is the first systematic study of the frequency dependent dielectric susceptibility over various PE concentrations and lengths by means of computer simulations. Both condensed and uncondensed counterions are characterized by a different dielectric response, a common assumption within the interpretation of experimental data, proven by our simulation results. In contrast to experiment we observe two dispersions due to condensed counterions at the largest and smallest relaxation times. We show that the relaxation process with the smallest relaxation time is due to the relaxation of condensed counterions at a single PE chain, while the relaxation process with the largest relaxation time is related to the correlated relaxation of condensed counterions.

Motivation for our study of PE electrophoresis in Chapter 4 is taken from recent experiments [20, 21] which highlight the important influence of the discrete nature of the charge distribution on PE chains. We discuss the electrophoretic response of an extended PE segment of varying charge architecture in the spirit of the cell model of PE solutions [22]. This picture relies on the observation, that PE chains assume locally straight conformations due to electrostatic repulsion between like-charged monomers.

For low electric fields, we show that the influence of the monomer-to-counterion size ratio and the charge separation indeed can be substantial, where the influence of the charge separation is strongly anisotropic. If the external electric field is directed parallel to the PE segment, counterions experience the corrugated potential due to the discrete charge distribution on the PE chain, which effects strong electrofriction. If the external electric field is directed perpendicular to the PE segment, counterions experience an effective PE potential where the corrugation is averaged out. In this case, renormalization of the PE charge due to counterion condensation reduces the electrophoretic response. We emphasize the importance of hydrodynamic interactions, which increase the electrophoretic response due to the *hydrodynamic entraining* effect. In fact, hydrodynamic interactions between PE chain and counterions may be so strong that counterions are dragged along with the PE chain, albeit at different velocity. In high electric fields, the PE electrophoretic response increases similar to the Wien effect in simple strong electrolyte solutions [23]. Under parallel field direction, condensed counterions are found to *evaporate* into the bulk.

The calculation of the relaxation effect for counterions at fixed charge distributions in Chapter 5 is intimately connected with some of the simulation results discussed in Chapter 4. We review the theoretical framework due to Jackson and Coriell [24] which leads to upper and lower bounds to the counterion mobility as functionals of the equilibrium electrostatic potential. We further present numerical evaluations of these functionals based on electrostatic potentials from Poisson-Boltzmann (PB) theory and counterion condensation (CC) theory. By comparison with BD simulations we show, that for a homogeneous charge distribution the CC theory underestimates the counterion mobility under parallel field direction, whereas agreement is near-to-perfect for perpendicular field direction. This shortcoming of CC theory is rooted in the assumption that condensed counterions are immobilized on the PE chain, irrespective of field direction. At the present state, neither PB nor CC theory are able to predict charge architecture effects. As a proof of principle, we evaluate upper and lower bounds to the counterion mobility using the electrostatic potential from strong coupling (SC) theory. PE-counterion electrofriction is captured nicely within the SC approach under parallel field direction. The SC theory fails for perpendicular field direction since it overestimates PE-counterion interactions. We show, that useful approximations to the counterion mobility in high electric fields can be obtained using an expression similar to Jackson and Coriell's upper bound.

Our last project, presented in Chapter 6, dealing with the salt-concentration dependent mobility of DNA in aqueous salt solution serves two purposes: (1) We proof that choosing the right coarse-graining parameters experimental salt-dependent DNA mobilities can be reproduced within BD simulations of the cell model introduced in Chapter 4. (2) We show that the counterion mobility changes sign as a function of salt concentration. For low salt conditions counterions stick to and move along with the DNA. For high salt conditions the motion decouples and counterions and DNA move in opposite directions. This counterion-mobility anomaly is captured by an analytic theory developed here for weakly charged chains based on the electrostatically screened hydrodynamic interaction tensor.

We give a summary and brief outlook in Chapter 7.

2. Coarse-grained polyelectrolyte dynamics

In the present Chapter, we shortly review the Brownian Dynamics (BD) simulation technique used in the subsequent projects.

In our hydrodynamic simulations, monomers and counterions are modeled as charged soft spheres whose positions $\boldsymbol{r}_i$ evolve according to the position Langevin equation [12]

$$\dot{\boldsymbol{r}}_i(t) = -\sum_j \mathbf{M}_{ij}(r_{ij}) \cdot \nabla_{\boldsymbol{r}_j} U\left(\{\boldsymbol{r}_k\}, t\right) + \boldsymbol{\xi}_i(t), \tag{2.1}$$

where $\boldsymbol{r}_i$ is the position vector of particle i, and $r_{ij} = |\boldsymbol{r}_i - \boldsymbol{r}_j|$ is the distance between particles i and j. The thermal coupling between particles and implicit solvent (characterized by viscosity η and permittivity ϵ) is provided through Gaussian white noise as specified by its moments $\langle \boldsymbol{\xi}_i(t) \rangle = \mathbf{0}$ and $\left\langle \boldsymbol{\xi}_i(t) \boldsymbol{\xi}_j(t') \right\rangle = 2\mathrm{k_B} T \delta(t - t') \mathbf{M}_{ij}(r_{ij})$. Under free-draining dynamics the hydrodynamic coupling of the dynamics of different particles is neglected. The mobility tensor $\mathbf{M}_{ij}(r_{ij})$ is diagonal where its entries are given by the Stokes mobility of a sphere with radius a_i,

$$\boldsymbol{M}_{ij}(r_{ij}) = \frac{\delta_{ij}}{6\pi\eta a_i}. \tag{2.2}$$

Here δ_{ij} denotes the Kronecker delta. Under non-draining dynamics the hydrodynamic coupling is included via the Rotne-Prager-Yamakawa mobility tensor [25, 26]. For non-overlapping particles of radii a_i, a_j the mobility tensor reads

$$\mathbf{M}_{ij} = \frac{1}{8\pi\eta r_{ij}} \left[\left(1 + \frac{a_i^2 + a_j^2}{3 r_{ij}^2} \right) \mathbf{I} + \left(1 - \frac{a_i^2 + a_j^2}{r_{ij}^2} \right) \frac{\boldsymbol{r}_{ij} \boldsymbol{r}_{ij}}{r_{ij}^2} \right], \quad r_{ij} > a_i + a_j \tag{2.3}$$

with $\boldsymbol{r}_{ij} = \boldsymbol{r}_i - \boldsymbol{r}_j$ and $r_{ij} = |\boldsymbol{r}_{ij}|$. Whereas Eq. (2.3) also holds for dissimilar sized particles, $a_i \neq a_j$, its counterpart for overlapping particles [25],

$$\mathbf{M}_{ij} = \frac{1}{6\pi\eta a}\left[\left(1 - \frac{9r_{ij}}{32a}\right)\mathbf{I} + \left(\frac{3}{r_{ij}}32a\right)\frac{\boldsymbol{r}_{ij}\boldsymbol{r}_{ij}}{r_{ij}^2}\right], \quad a_i = a_j = a \tag{2.4}$$

is only true for particles of equal size. The mobility tensor defined in Eqns. (2.3) and (2.4) is positive definite which ensures the dynamics to be dissipative.

The interaction potential $U = U_{\mathrm{LJ}} + U_{\mathrm{C}} + U_{\mathrm{S}} + U_{\mathrm{ext}}$ entering the Langevin equation Eq. (2.1) consists of: (1) A truncated, shifted Lennard-Jones potential,

$$\frac{U_{\mathrm{LJ}}}{\mathrm{k_B}T} = \begin{cases} \frac{\epsilon}{\mathrm{k_B}T}\sum_{\langle ij\rangle}\left[\left(\frac{\sigma_{ij}}{r_{ij}}\right)^{12} - 2\left(\frac{\sigma_{ij}}{r_{ij}}\right)^{6} + 1\right] & r_{ij} \leq \sigma_{ij} \\ 0 & r_{ij} > \sigma_{ij} \end{cases} \tag{2.5}$$

that prevents electrostatic collapse of opposite charges. Here $\sigma_{ij} = a_i + a_j$ and ϵ define the soft-core distance and repulsion. (2) An unscreened Coulomb potential,

$$\frac{U_{\mathrm{C}}}{\mathrm{k_B}T} = \ell_{\mathrm{B}}\sum_{\langle ij\rangle}\frac{q_i q_j}{r_{ij}}, \tag{2.6}$$

where q_i stands for a particle's charge valency and $\ell_{\mathrm{B}} = \mathrm{e}^2/4\pi\epsilon_{\mathrm{r}}\epsilon_0\mathrm{k_B}T$ is the Bjerrum distance at which two unit charges interact with thermal energy k_BT ($\ell_{\mathrm{B}} = 7.2\,\text{Å}$ in water at 20 °C). (3) A harmonic spring potential,

$$\frac{U_{\mathrm{S}}}{\mathrm{k_B}T} = \frac{K}{2}\sum_{\langle ij\rangle}(r_{ij} - \sigma_{ij})^2, \tag{2.7}$$

acting between adjacent monomers which ensures chain connectivity, and whose stiffness is controlled by the spring constant K. (4) A constant external electric potential (cf. Chapters 4, 5, and 6) with field strength $|\boldsymbol{E}_0| = E_0$,

$$\frac{U_{\mathrm{ext}}}{\mathrm{k_B}T} = -\frac{\mathrm{e}}{\mathrm{k_B}T}\sum_i q_i\,\boldsymbol{r}_i\cdot\boldsymbol{E}_0, \tag{2.8}$$

or a time-periodic external electric potential (cf. Chapter 3) with radial frequency ω and field strength $|\boldsymbol{E}_0| = E_0$,

$$\frac{U_{\mathrm{ext}}}{\mathrm{k_B}T} = -\frac{\mathrm{e}}{\mathrm{k_B}T}\sum_i q_i\,\boldsymbol{r}_i\cdot\boldsymbol{E}_0\cos(\omega t). \tag{2.9}$$

The numerical integration of the Langevin equation Eq. (2.1) is implemented using a discretization time step Δ. For convenience, we go over to dimensionless variables by scaling length, charge, energy and time with counterion radius a_{ct}, elementary charge e, thermal energy $\mathrm{k_B}T$, and $a_{\mathrm{ct}}^2/\mu_0\mathrm{k_B}T$, respectively, where $\mu_0 = 1/6\pi\eta a_{\mathrm{ct}}$ denotes the Stokes mobility of a counterion of hydrodynamic radius a_{ct}. Accordingly, we have $\tilde{\boldsymbol{r}}_i = \boldsymbol{r}_i/a_{\mathrm{ct}}$ for the position vectors, $\tilde{U} = U/\mathrm{k_B}T$ for the potential energy, and $\tilde{\Delta} = (\mu_0\mathrm{k_B}T/a_{\mathrm{ct}}^2)\Delta$ for the discretization time step. Throughout simulations we use $\epsilon/\mathrm{k_B}T = 5$ for the softcore repulsion, $Ka_{\mathrm{ct}}^2 = 100$ for the spring constant, and $\tilde{E}_0 = \mathrm{e}a_{\mathrm{ct}}E_0/\mathrm{k_B}T = 0.03 - 0.05$ for the amplitude of the external electric field. The large value of the spring constant Ka_{ct}^2 yields a narrow bond-length distribution. The electric field strength $\tilde{E}_0$ is chosen on the one hand small enough to meet the linear response condition, on the other hand large enough to guarantee adequate configuration space sampling at reasonable computational cost. The scaled discretization time step is set to $\tilde{\Delta} = 0.002$. Production runs cover $\sim 10^8 - 10^9$ time steps.

3. Dielectric response in salt-free polyelectrolyte solutions

In PE solutions, the structure of the counterion atmosphere is determined by the balance of long-range electrostatic attraction to and entropic repulsion from the PE chain. A convenient measure for the strength of electrostatic interactions as compared to entropy is provided by the so-called *Manning parameter* [27]

$$\xi_{\mathrm{M}} = \frac{|q_{\mathrm{ct}} q_{\mathrm{m}}| \mathrm{e}^2}{4\pi\epsilon\epsilon_0 \mathrm{k_B} T b}\,, \tag{3.1}$$

which compares the distance $|q_{\mathrm{ct}} q_{\mathrm{m}}| \mathrm{e}^2 / 4\pi\epsilon\epsilon_0 \mathrm{k_B} T$ at which the electrostatic attraction between a counterion of valency q_{ct} and a charged monomer of valence q_{m} equals thermal energy $\mathrm{k_B} T$ with the charge separation b on the PE chain. (Here we denote the elementary charge by e, the relative solvent permittivity by ϵ, the vacuum permittivity by ϵ_0, and the Boltzmann constant by $\mathrm{k_B}$.) For a weakly charged PE characterized by $\xi_{\mathrm{M}} < 1$ the counterion population forms a diffuse atmosphere. For a strongly charged PE characterized by $\xi_{\mathrm{M}} > 1$ the counterion population breaks up into a fraction accumulating close to the PE chain and a fraction forming the diffuse atmosphere. The former are commonly referred to as *condensed*, the latter as *uncondensed counterions*. Note that ξ_{M} denotes the locus of a true phase transition in the thermodynamic limit [28, 29].

Application of a time-dependent external electric field $\boldsymbol{E}(t)$ perturbs the equilibrium counterion distribution, thereby inducing a fluctuating dipole density $\boldsymbol{P}(t)$. For a linear medium the average time-dependent dipole density follows from the convolution of the external electric field with the time-dependent dielectric susceptibility $\chi(t)$

$$\langle \boldsymbol{P}(t) \rangle = \epsilon_0 \int_{-\infty}^{t} \mathrm{d}t' \chi(t - t')\, \boldsymbol{E}(t'), \tag{3.2}$$

where $\langle \cdot \rangle$ denotes an ensemble average. The time-dependent dielectric susceptibility $\chi(t)$ is a scalar in case of an isotropic medium, and a second rank tensor in case of an anisotropic medium. In frequency space Eq. (3.2) simplifies to

$$\langle \boldsymbol{P}(\omega) \rangle = \epsilon_0 \, \chi(\omega) \, \boldsymbol{E}(\omega), \tag{3.3}$$

by virtue of the convolution theorem. Here ω is the radial frequency, and $\chi(\omega) = \chi'(\omega) + \mathrm{i}\chi''(\omega)$ is the complex frequency-dependent dielectric susceptibility. Due to causality real part $\chi'(\omega)$ and imaginary part $\chi''(\omega)$ of the dielectric susceptibility are interrelated via the Kramers-Kronig relations [30, 31]. In general, the induced dipole density in a PE solution can be decomposed into different dielectric relaxation processes according to

$$\langle \boldsymbol{P}(\omega) \rangle = \epsilon_0 \sum_i \Delta\chi_i(\omega) \, \boldsymbol{E}(\omega), \tag{3.4}$$

where $\Delta\chi_i(\omega)$ stands for the incremental frequency-dependent dielectric susceptibility due to the i-th dielectric relaxation process. (In what follows we drop the label "incremental" for the sake of better readability.) Each dielectric relaxation process is characterized by its *relaxation time* τ_i and its static dielectric susceptibility or *relaxation strength* $\Delta\chi_i^{(0)} \equiv \Delta\chi_i(\omega \to 0)$ related to the speed of the build-up and the strength of the induced dipole moment. The analysis of an experimentally recorded dielectric spectrum is commonly done through fitting of phenomenological relaxation functions. By means of a suitable model the fit parameters relaxation time τ_i and strength $\Delta\chi_i^{(0)}$ then can be related to dynamics and structure of the PE solutions.

As compared to simple salt solutions, PE solutions reveal a high dielectric susceptibility. In aqueous solutions of strongly charged PEs such as DNA, PSS, or PAA, to name but a few, one generally discriminates among three dominating relaxation processes; while one of them is due to water relaxation, the other two are on account of counterion relaxation. The relaxation of water is observed at about $\omega = 17 \times 10^9$ Hz where the large permittivity ($\epsilon_{\mathrm{H_2O}} = 80.1$ at 20 °C) results from the considerable permanent dipole moment of individual water molecules. (We note in passing that the presence of PEs only moderately decreases the water permittivity and shifts the relaxation time.) Processes ascribed to counterion relaxation divide into a low-frequency (LF) process at frequencies around $10^3 - 10^5$ Hz and a high-frequency (HF) process at frequencies around $10^6 - 10^8$ Hz [32–42]. Under most experimental

conditions the relaxation strength $\Delta\chi_{\mathrm{HF}}^{(0)}$ of the HF process is found to be stronger than that of the LF process $\Delta\chi_{\mathrm{LF}}^{(0)}$.

In dilute PE solutions, *i.e.* when the average distance between PEs is larger than the average PE extension, the HF process as well as the LF process depend on both PE concentration c_{p} and molecular weight N_{m}. In detail, the strength of the HF process $\Delta\chi_{\mathrm{HF}}^{(0)}$ increases with PE concentration and molecular weight, while the relaxation time τ_{HF} decreases with PE concentration and increases with molecular weight [33, 34, 36, 39, 42]. Similarly, the strength of the LF relaxation process $\Delta\chi_{\mathrm{LF}}^{(0)}$ increases with PE concentration and molecular weight, the relaxation time τ_{LF} is independent of PE concentration and increases with molecular weight [34, 37, 39, 43, 44]. The rate of increase of relaxation strength as well as relaxation time with PE concentration or molecular weight is higher for the LF process than for the HF process. Regarding the relaxation time, this makes a merger of HF and LF process possible. When going from dilute to semi-dilute PE solutions a crossover behavior of the HF process is observed [32, 33, 35]. In this regime, the strength of the HF process $\Delta\chi_{\mathrm{HF}}^{(0)}$ becomes independent of PE concentration and molecular weight, and the relaxation time τ_{HF} decreases with PE concentration and is similarly independent of molecular weight [33, 35, 36, 42]. For the less extensively studied LF process no crossover behavior has been observed.

It is largely agreed, that the relaxation of *uncondensed counterions* correlates with the HF dispersion [32–34, 38–41]. This concept is back-upped by comparison of experimental data against scaling relations for the molecular weight and concentration dependence of relaxation time τ_{HF} and strength $\Delta\chi_{\mathrm{HF}}^{(0)}$ [32, 33, 39–41]. Assuming the characteristic length of the HF relaxation process to be given by the PE correlation length ξ_{p} [32, 33, 39–41, 45] these scaling relations for instance capture the crossover behavior when going from dilute to semi-dilute PE solutions. Additional information gathered from frequency-domain electric birefringence measurements indicates that the HF process is due to uncondensed counterions relaxing *perpendicular* to the PE chain [46].

Less consensus prevails on the origin of the LF process. While some authors claim the relaxation of *condensed counterions* to constitute the LF process [33, 34, 36], recent publications dispute the clear-cut discrimination between contributions of condensed and uncondensed counterions in the LF regime [39–41]. Within the scaling approach, the characteristic length of the LF process is assumed to be given by the average end-to-end distance R of a PE chain [33, 34, 39], or the length of a PE correlation blob [39–41]. As opposed to the HF process, it is understood that counterions relax *parallel*

to the PE chain [46]. Since most publications on the dielectric response of PE solutions focus on the HF process due to intrinsic experimental difficulties when measuring at low frequencies, scaling expressions for relaxation time τ_{LF} and strength $\Delta\chi_{\mathrm{LF}}^{(0)}$ of the LF process derived by Bordi *et al.* [47] for both dilute and semi-dilute solutions could only provisionally be verified [34, 47].

To date, most theories address the calculation of the dielectric response of the condensed counterions parallel to a single PE chain [48–58]. On the one hand this is owing to the fact that the substantial contribution of the uncondensed counterions simply had been overlooked in the infancy of dielectric spectroscopy, on the other hand owing to the intimidating complexity of the PE solution which makes any theoretical description a formidable task. As a matter of fact, we know of only one theory which holds true for the dielectric response of condensed as well as uncondensed counterions, parallel or perpendicular to the PE chain [59–61]. Although valuable qualitative insight has been gained from numerical solutions of this model, an extensive quantitative comparison with experiment has not been tried. Moreover, long-range electrostatic interactions can be substantial even in dilute PE solutions which makes the focus on a single PE chain with its counterion atmosphere look questionable [52]. A first step including interactions between different PE chain-counterion atmosphere complexes indicate strong quantitative if not qualitative differences as compared to theories considering one single PE chain with its counterion atmosphere [62]. In order to get a flavor of the current state of the art we review some of the cornerstones of the theories for the dielectric response of PE solutions below.

The challenges awaiting theoretical models of dielectric relaxation in PE solutions are high. In the first place, a successful model has to capture the sheer magnitude of the static dielectric response. In the second place, the scaling with PE concentration, molecular weight, and PE charge density has to be met, as well as the dependence on the concentration of added salt. In the third place, the frequency dependence of the dielectric response has to be considered. And finally one has to account for the effect of solvent flow. Within the simplest approach the PE chain is considered as a discretely or uniformly charged rod, and the dielectric susceptibility is determined from the parallel response of an effective one-dimensional condensed counterion density along the rod with respect to the external electric field, or equivalently from the equilibrium fluctuations of the effective one-dimensional condensed counterion density. In both cases it is assumed that condensed counterions polarize but do not conduct, which allows for the application of equilibrium statistical mechanics in the former case. Neglecting counterion-counterion interactions, within Mandel's theory the condensed counterion density

results from the association of individual counterions at charged sites on the PE chain [48]. Here the probability of counterion association at a particular charged site follows from a local free energy which depends on the external electric field. The resulting dielectric susceptibility is proportional to the PE length L_0 cubed,

$$\chi_{\parallel}^{(0)} = \frac{q_{\mathrm{ct}}^2 \mathrm{e}^2}{12\epsilon_0 \mathrm{k_B} T b} \frac{\theta L_0^3}{V}, \tag{3.5}$$

where counterions and monomers are assumed to have the same valency $|q_{\mathrm{ct}}| = |q_{\mathrm{m}}|$, θ denotes the fraction of condensed counterions, and V the volume accessible to one PE chain of contour length $L_0 = bN_{\mathrm{m}}$, monomer number N_{m}, and charge spacing b. Note that electrostatic interactions between the PE chain and its counterions enter Eq. (3.5) only implicitly through the fraction of condensed counterions, which acts as a free parameter. Under the assumption of diffusive relaxation of condensed counterions, Mandel complements his theory with a heuristic expression for the relaxation time,

$$\tau_{\parallel} = \frac{\zeta_{\mathrm{cc}} L_0^2}{12 \mathrm{k_B} T}, \tag{3.6}$$

where ζ_{cc} is the friction coefficient of a condensed counterion. In an attempt to explain the two distinct dispersions in the dielectric spectrum, in a follow-up van der Touw and Mandel considered a PE chain made up of rod-like subunits as a model for a flexible PE chain [57]. In this case the dielectric response consists of contributions due to counterion relaxation over a subunit and counterion relaxation over the PE extension where the former process is regarded as fast as compared to the latter. Within this picture, counterion relaxation over a subunit thus correlates with the HF process, whereas counterion relaxation over the PE extension correlates with the LF process. One salient shortcoming of Mandel's model due to the neglect of counterion-counterion interactions is the proportionality of the dielectric susceptibility $\chi_{\parallel}^{(0)}$ to the fraction of condensed counterions θ which contrasts with experiment where the dielectric susceptibility saturates with the fraction of condensed counterions. The relaxation strength as calculated from Eq. (3.5) has been reported to be nearly two orders of magnitude too high as compared to experiments, which is ascribed to the neglect of counterion-counterion repulsion [63, 64].

Including the counterion-counterion interaction potential $\phi(r)$ Oosawa [54, 55] calculated the dielectric response of condensed counterions at a uniformly charged rod from the equilibrium fluctuations of the condensed counterion density by virtue of the fluctuation-dissipation theorem [65]. Within

this framework the complex dielectric susceptibility follows from the superposition of different relaxation modes as

$$\chi_{\parallel}(\omega) = \sum_{k=1}^{\infty} \frac{\Delta\chi_k^{(0)}}{1 + \mathrm{i}\omega\tau_k} \,. \tag{3.7}$$

The dielectric susceptibility of the k-th mode is given by

$$\Delta\chi_k^{(0)} = \frac{q_{\mathrm{ct}}^2 \mathrm{e}^2}{12 \mathrm{k_B} T b} \frac{\theta L_0^3}{V} \frac{6/\pi^2}{k^2 \left(1 + \theta |q_{\mathrm{ct}}| N \phi_k / \mathrm{k_B} T\right)} \,, \tag{3.8}$$

and the corresponding relaxation time reads

$$\tau_k = \frac{\zeta_{\mathrm{cc}}}{\mathrm{k_B} T} \left(\frac{L_0}{2\pi k}\right)^2 \left(1 + \theta |q_{\mathrm{ct}}| N \phi_k / \mathrm{k_B} T\right) \,, \tag{3.9}$$

where $\phi_k = \int_0^{L_0} \mathrm{d}r \, \phi(r) \cos(2\pi k r / L_0) / L_0$ is the Fourier transform of the interaction potential. The superposition of different relaxation modes in Eq. (3.7) provides a viable explanation for the experimentally observed broad relaxation spectrum. In the absence of counterion-counterion interactions the static dielectric susceptibility $\chi_{\parallel}^{(0)}$ calculated from Eq. (3.7) reduces to Mandel's solution Eq. (3.5). In the presence of counterion-counterion interactions $\chi_{\parallel}^{(0)}$ saturates for large fractions of condensed counterions $\theta \to 1$. In addition to the quadratic length dependence, the relaxation times Eq. (3.9) do also depend on the fraction of condensed counterions θ. Counterion-counterion interactions suppress fluctuations of the condensed counterion density and tend to slow down the relaxation. For a discretely charged rod similar expressions have been derived by Minakata *et al.* [53] and Warashina and Minakata [66].

In an alternative approach, Manning incorporates electrostatic interactions into Mandel's model within the framework of counterion condensation theory [27, 49–51]. This comprises an explicit expression for the fraction of condensed counterions

$$\theta = 1 - \frac{1}{\xi_{\mathrm{M}}} \,. \tag{3.10}$$

Under excess salt conditions, the dielectric susceptibility reads

$$\chi_{\parallel}^{(0)} = \frac{q_{\mathrm{ct}}^2 \mathrm{e}^2}{12 \epsilon_0 \mathrm{k_B} T b} \frac{\theta}{1 - 2 q_{\mathrm{ct}}^2 \xi_{\mathrm{M}} \theta \ln(\kappa b)} \frac{L_0^3}{V} \,, \tag{3.11}$$

where the Debye-Hückel screening length κ^{-1} scales with the salt concentration c_s as $\kappa^2 \propto c_s$. The dielectric susceptibility according to Manning resembles the dielectric susceptibilities found within the Oosawa model Eq. (3.8) except for the contribution from the counterion-counterion interactions. The dielectric susceptibility is reduced due to Debye-Hückel screening of electrostatic interactions between condensed counterions. Manning predicts the dielectric susceptibility to increase with salt concentration, in contrast to experimental observations where the dielectric susceptibility decreases [34, 56, 67, 68]. If we accept Manning's assumptions to be correct, this failure suggests that the dielectric response of a PE solution for a greater part is determined by contributions different from the parallel response of the condensed counterions, which feature the appropriate salt concentration dependence.

We complete our survey over theories for the parallel dielectric response of condensed counterion with recent work by Mohanty and Zhao [69] within the framework of statistical mechanics of inhomogeneous systems. Depending on the direct correlation function of the uniform condensed counterion phase the dielectric susceptibility interpolates between L_0^2 and L_0^3 dependence.

As pointed out by Fixman [60], the theoretical description of dielectric relaxation within the framework of equilibrium statistical mechanics is inadequate in so for as it neglects the ionic conductivity. Setting out from the Smoluchowski equation for the dynamics of co- and counterions at a charged cylinder, Fixman derives an expression for the parallel dielectric susceptibility in the thin double layer approximation which accounts for the leakage of counterions through the double layer [59]. This model predicts a dependence on the PE length that crosses over from L_0^3 to L_0 depending on parameters. For weak screening $\kappa L_0 < 1$ numerical solutions of the model equations for arbitrary double layer width reveal that parallel and perpendicular dielectric relaxation are of the same order of magnitude [61]. Under the same conditions the contributions from the diffuse counterion atmosphere outweighs the contribution from the condensed counterions. Fixman is the first to note that convection of counterions can greatly magnify the dielectric response of a PE solution.

Another work that highlights the importance of the contribution of the diffuse counterion atmosphere is due to Rau and Charney who treat electrostatic interactions on the linear Debye-Hückel level [70]. They find a parallel dielectric susceptibility whose PE length and salt concentration dependence exhibits a crossover from $\chi_\parallel^{(0)} \propto \kappa^{-1.2} L_0^{1.8}$ for weak screening ($\kappa L_0 \lesssim 10$) to $\chi_\parallel^{(0)} \propto \kappa^{-2} L_0$ for strong screening ($\kappa L_0 \gtrsim 10$). Experiments by Hogan *et al.* who report quadratic length and inverse Debye-Hückel screening length dependence at low salt concentration support Rau and Charney's

model [71]. In the spirit of a two phase model the Rau and Charney model [72] for the parallel dielectric response of the diffuse counterion atmosphere is combined with Manning's model [49–51] for the parallel dielectric response of the condensed counterions in Ref. [72].

Despite years of considerable effort, from a theoretical physicists point of view our understanding of dielectric relaxation is still limited. At this point stochastic simulations of model PE solutions can be of value, both to gain insight into the dynamics of PE solutions on length and time scales inaccessible to experiment, and as a well-defined testing ground for theory. Every method has its limitation, though. With regard to simulation studies this means, that due to limited computational resources most studies on the dielectric response of PE solutions were confined to a single short PE chain and its counterions with salt added occasionally.

The relaxation of counterions at a rodlike PE following the switching on of an external electric field is considered by Yoshida and Kikuchi [73] using Monte Carlo simulations. They report relaxation times estimated from a fit of a single exponential to the build-up of the induced dipole moment which increase with PE length. these results have to be taken with caution, though, since field strength as well as monomer concentration are chosen rather high.

A similar simulation protocol is followed by Grycuk *et al.* and Antosiewicz and Porschke [16, 17] based on Brownian Dynamics simulations of a rodlike PE with co- and counterions, with or without hydrodynamic interactions. The outcome of this study underlines the importance of the perpendicular response which, though smaller than the parallel response, cannot be neglected. The consideration of hydrodynamic interactions leads to a smaller dielectric response.

In a series of publications Washizu and Kikuchi calculate the dielectric response of a rodlike PE chain with or without added salt from the equilibrium fluctuations of the dipole density generated by means of Monte-Carlo simulations [74–77]. Their analysis of the partial dielectric response of condensed or uncondensed counterions parallel or perpendicular to the PE chain lead to a couple of groundbreaking statements: (1) Condensed and uncondensed counterion differ significantly in their dielectric response, where the contribution of the condensed counterions is small as compared to the contribution of the uncondensed counterions. The latter follows from the volume accessible to the counterions which is considerably smaller for the condensed counterions. (2) The perpendicular response is small as compared to the parallel response, but of the same order of magnitude. Further, Washizu and Kikuchi find the partial dielectric susceptibility of the condensed counterions to be independent of PE concen-

tration and proportional to the second power of the molecular weight, whereas the partial dielectric susceptibility of the uncondensed counterions decreases with PE concentration and is proportional to the first to second power of the molecular weight. Upon addition of salt the distribution of uncondensed counterions is compressed, the dielectric susceptibility decreases. The dielectric susceptibility weakly increases with salt concentration, which reflects the decreased resistance to distortion of the condensed layer already explained by Manning [49].

Brownian Dynamics simulations of the dielectric response of short semiflexible PEs in salt solution are contributed by Schlagberger and Netz [19]. Hydrodynamic interactions are included, and the dielectric response of condensed and uncondensed counterions parallel and perpendicular with respect to the external electric field are calculated. The authors report the dielectric susceptibility to be a non-monotonous function of the salt concentration. For dilute PE solutions in the limit of strong screening $\kappa L_0 \gg 1$ parallel as well as perpendicular dielectric susceptibility rise with the third power of the PE length in accord with Fixman and Jagannathan [61]. Under the same conditions the parallel dielectric susceptibility of the condensed counterions grows with the third power of the PE length, while the perpendicular dielectric susceptibility grows linearly with the PE length.

Outline

In this Chapter we present BD simulations of the cell model of PE solutions in a time-varying external electric field. For a flexible PE chain in the simulation cell we consider two protocols: (1) varying PE concentration at fixed PE length and (2) varying PE length at fixed PE concentration. Thereby, the PE concentrations are always below the overlap concentration, *i.e.* the PE solution is dilute.

As expected, we observe two relaxation processes, which are analyzed using phenomenological fitting functions of Cole-Cole type. As opposed to experiment we find the LF response to be stronger than the HF response. Comparison of the fit parameters with scaling predictions for relaxation strength and relaxation time due to Ito *et al.* [33] and Bordi *et al.* [47], cf. Section 3.1, suggests correlation of the LF process with the relaxation of uncondensed counterions, whereas the HF process follows the scaling prediction characteristic for the condensed counterions, in contrast to experiment. We unambiguously check this assertion by separately measuring the relaxation of condensed and uncondensed counterions and find near to perfect confirmation. Relaxation strengths and relaxation times obtained from BD simulations at fixed PE length and varying PE concentration nicely agree with the scaling predictions.

At fixed PE concentration and varying PE length deviations from the scaling predictions are visible. Relaxation parallel to the PE axis is stronger than relaxation perpendicular to the PE axis, in accord with simulations of the dielectric response of stiff PEs in salt solution [19]. However, for a flexible PE the difference between parallel and perpendicular relaxation is less pronounced than for a stiff PE. Moreover, due to chain crumpling on small length scales the PE length dependence of the dielectric susceptibility of the condensed counterions is independent of directions, in contrast to the scaling predictions which assume a stiff PE.

In order to explain the apparent interchange of LF and HF process as compared to experiment we study the dependence of the dielectric susceptibility on the number of PEs in the simulation cell. In doing so, we keep PE concentration and length fixed. The dielectric susceptibility decreases with PE number due to overlap of counterion atmospheres. We observe a third dispersion at frequencies lower than the LF process. This low-low-frequency (LLF) process is connected with the correlated relaxation of condensed counterions, and corresponds to the low-frequency process observed within experiment.

3.1. Phenomenological description and scaling predictions

3.1.1. Phenomenological description

In the linear response limit the time-dependent dielectric susceptibility can be obtained from the equilibrium fluctuations of the dipole density [31],

$$\chi(t) = -\frac{V}{3\epsilon_0 \mathrm{k_B} T} \left\langle \boldsymbol{P}^2 \right\rangle_0 \frac{\mathrm{d}\Phi_\mathrm{P}(t)}{\mathrm{d}t}, \tag{3.12}$$

where $\langle \cdot \rangle_0$ denotes an equilibrium average at zero field $\boldsymbol{E} = \boldsymbol{0}$, and V the sample volume. Here we introduced the dipole correlation function

$$\Phi_\mathrm{P}(t) = \frac{\langle \boldsymbol{P}(t) \cdot \boldsymbol{P}(0) \rangle_0}{\left\langle \boldsymbol{P}^2 \right\rangle_0}, \tag{3.13}$$

which, in a strict sense, is only defined for times $t > 0$ owing to causality. In frequency space the corresponding expression for the complex frequency dependent dielectric susceptibility reads

$$\chi(\omega) = \frac{V}{3\epsilon_0 \mathrm{k_B} T} \left\langle \boldsymbol{P}^2 \right\rangle_0 \left[1 - \mathrm{i}\omega\, \Phi_\mathrm{P}(\omega)\right], \tag{3.14}$$

with the (one-sided) Fourier transform of the dipole correlation function $\Phi_{\mathrm{P}}(\omega) = \int_0^\infty \mathrm{d}t\, \Phi_{\mathrm{P}}(t) \mathrm{e}^{-\mathrm{i}\omega t}$. Both Eq. (3.12) and Eq. (3.14) are formulations of the fluctuation-dissipation theorem; the energy dissipation as expressed by the dielectric susceptibility is related to the time derivative of the equilibrium dipole fluctuations. This becomes more obvious when considering the imaginary part of the dielectric susceptibility,

$$\chi''(\omega) = -\frac{V}{3\epsilon_0 \mathrm{k_B} T} \left\langle \boldsymbol{P}^2 \right\rangle_0 \mathrm{Re}[\omega\, \Phi_{\mathrm{P}}(\omega)]\,, \tag{3.15}$$

which is proportional to the energy density dissipated during one cycle of the external electric field,

$$\Delta W = 4\pi\epsilon_0 E_0^2\, \chi''(\omega)\,. \tag{3.16}$$

Technically speaking, the dipole correlation function determines the dielectric response. In the simplest case, the dipole correlation function follows an exponential decay,

$$\Phi_{\mathrm{P}}(t) = \mathrm{e}^{-t/\tau} \tag{3.17}$$

where τ is the relaxation time. The corresponding frequency-dependent dielectric susceptibility Eq. (3.14) is

$$\chi(\omega) = \frac{\chi^{(0)}}{1 + \mathrm{i}\omega\tau} = \chi^{(0)} \left[\frac{1}{1 + (\omega\tau)^2} - \frac{\mathrm{i}\omega}{1 + (\omega\tau)^2} \right] \tag{3.18}$$

with the shorthand notation $\chi^{(0)} = V \left\langle \boldsymbol{P}^2 \right\rangle_0 / 3\epsilon_0 \mathrm{k_B} T$ for the static dielectric susceptibility. Exponential relaxation is also known as Debye-relaxation, with Eq. (3.18) being derived in the context of orientational relaxation of permanent molecular dipoles [78]. Upon separation of the complex dielectric susceptibility into real part $\chi'(\omega)$ and imaginary part $\chi''(\omega)$ we can identify some characteristic features pertaining to relaxation spectra in general; (1) The real part $\chi'(\omega)$ is a monotonically decreasing function of the radial frequency ω, the charged entities do not have the time to follow the external electric field once the frequency ω is larger than the characteristic frequency $2\pi/\tau$. (2) The imaginary part $\chi''(\omega)$ exhibits a broad peak centered around the characteristic frequency $2\pi/\tau$ where energy dissipation is maximum.

As a rule, the dielectric response of PE solutions does not obey a single exponential decay with a single relaxation time, but can be modeled by a superposition of exponentials with a continuous distribution of relaxation times,

$$\Phi_{\mathrm{P}}(t) = \int_0^\infty \mathrm{d}\tau\, g(\tau)\, \mathrm{e}^{-t/\tau}\,. \tag{3.19}$$

For the relaxation time distribution function $g(\tau)$ (as well as for the dipole correlation function $\Phi_{\mathrm{P}}(t)$ and $\Phi_{\mathrm{P}}(\omega)$, respectively) a veritable zoo of expressions have been proposed. The essential differences as compared to Eqns. (3.17) and (3.18) are the introduction of stretched exponential or inverse power-law decays in the time domain, and the change of broadness and skewness in the frequency domain.

In the frequency domain, the most general expression for the dielectric susceptibility is provided by the Havriliak-Negami function [79, 80]

$$\chi(\omega) = \frac{\chi(0)}{[1+(\mathrm{i}\omega\tau)^\alpha]^\beta} \tag{3.20}$$

with $0 < \alpha, \beta < 1$. On a logarithmic frequency scale, the exponent α controls the slope of the real part $\chi\prime(\omega)$ and peak width of the imaginary part $\chi\prime\prime(\omega)$ of the dielectric susceptibility, whereas the exponent β controls the skewness with respect to the characteristic frequency $2\pi/\tau$. For $\alpha = 1$ and $\beta = 1$ Eq. (3.20) reduces to the Debye relaxation function Eq. (3.18). In the time domain, the corresponding dipole relaxation function can be expressed in terms of Fox functions [81]. In our analysis we will adopt the somewhat simpler, amply used Cole-Cole function [82]

$$\chi(\omega) = \frac{\chi(0)}{1+(\mathrm{i}\omega\tau)^\alpha} \tag{3.21}$$

which results from setting $\beta = 1$ in the Havriliak-Negami function Eq. (3.20). As compared to the Havriliak-Negami function Eq. (3.20) on a logarithmic frequency scale the Cole-Cole function Eq. (3.21) preserves the symmetry of the Debye relaxation function Eq. (3.18). The time domain expression for the corresponding dipole relaxation function is given by the Mittag-Leffler function [81], which interpolates between stretched exponential decay at short times $t \ll \tau$ and inverse power-law decay at long times $t \gg \tau$. The Mittag-Leffler function is the solution of the fractional relaxation equation, which arises in systems displaying some form of disorder [83].

While the heuristic modeling of experimental data is well developed, there remains a yawning gap as to the microscopic origin of the phenomenological expressions. For example the relation of the

exponents α and β in the Havriliak-Negami function Eq. (3.20) to microscopic properties of the PE solution is completely obscure.

3.1.2. Scaling predictions

The scaling approach due to Ito and coworkers [33] rests upon the assumption that counterion relaxation proceeds uncorrelatedly and diffusively. Starting point is the fluctuation-dissipation theorem Eq. (3.14) for the static dielectric susceptibility. If the number of counterions in a volume Δ^3 surrounding a PE chain is N_{ct}, then counterion number fluctuations of order $\sqrt{N_{\mathrm{ct}}}$ induce dipole fluctuations of order $\left\langle \boldsymbol{P}^2 \right\rangle \propto N_{\mathrm{ct}} \mathrm{e}^2 \Delta^2$. In this context Δ denotes a characteristic length in the PE solution which will be specified below. With this crude approximation for the dipole fluctuations the scaling relation for the static dielectric susceptibility reads

$$\Delta\chi \propto N_{\mathrm{ct}} \frac{\ell_{\mathrm{B}} \Delta^2}{V} . \tag{3.22}$$

Provided counterion relaxation is diffusive, the scaling relation for the relaxation time follows as

$$\tau \propto \frac{\zeta_{\mathrm{ct}} \Delta^2}{\mathrm{k_B} T} . \tag{3.23}$$

Where ζ_{ct} is the friction coefficient of a counterion. What have we gained so far? We traced both the static dielectric susceptibility and the relaxation time back to some characteristic length Δ of the PE solution. In what follows, we identify the characteristic lengths associated with fluctuations of uncondensed and condensed counterions, and propose corresponding scaling relations. We restrict our discussion to dilute PE solutions, extensions to semi-dilute PE solutions can be found in Refs. [33, 47].

Uncondensed counterions

We adopt the PE correlation length $\Delta \propto \left(V/N_{\mathrm{p}}\right)^{1/3}$ [84] where N_{p} is the number of PEs in the volume V as the characteristic length linked to the relaxation of uncondensed counterions. The underlying picture is the following: Inter-chain electrostatic repulsion induces liquid-like correlations among PE chains. Uncondensed counterions consequently explore a spatially periodic electrostatic potential which inherits its periodicity from PE correlations. (Within scattering experiments the PE correlation length can be determined from the position of the first peak in the static structure factor.)

The number of uncondensed counterions is fixed by the number of charged groups on the PE chain, $N_{\mathrm{uc}} \propto (1-\theta) N_{\mathrm{m}}$, with the fraction of condensed counterions θ. Introducing the overlap monomer concentration $c_{\mathrm{m}}^{*} = N_{\mathrm{m}}/R^3$, where $R \propto a_{\mathrm{m}} N_{\mathrm{m}}$ for PEs of monomer size a_{m} whose extension grows linearly with the monomer number, we obtain from Eq. (3.22)

$$\Delta\chi_{\mathrm{uc}} \propto \frac{(1-\theta)\,\ell_{\mathrm{B}}}{a_{\mathrm{m}}}\, N_{\mathrm{m}}^{0} \left(\frac{c_{\mathrm{m}}}{c_{\mathrm{m}}^{*}}\right)^{1/3} \tag{3.24}$$

for the static dielectric response. Likewise for the relaxation time we get

$$\tau_{\mathrm{uc}} \propto \frac{\zeta_{\mathrm{ct}} a_{\mathrm{m}}^{2}}{\mathrm{k_B} T}\, N_{\mathrm{m}}^{2} \left(\frac{c_{\mathrm{m}}}{c_{\mathrm{m}}^{*}}\right)^{-2/3} . \tag{3.25}$$

One comment is in order. We tacitly assumed isotropy of the PE solution on the scale of the correlation length. Strictly speaking, this holds for very dilute solutions only, where the PE correlation length is much larger than the PE extension. As the PE concentration approaches the overlap concentration we accordingly expect deviations from scaling. On the other hand, the range of applicability of the scaling relations Eqns. (3.24) and (3.25) might as well extend to the case of strong anisotropy of the dielectric response as known from experiment, as long as it captures the properties of the dominant contribution.

Condensed counterions

The latter comment particularly applies to the relaxation of condensed counterions which are confined to a strongly anisotropic volume close to the PE chain. Similar as before, the number of condensed counterions is proportional to the monomer number, $N_{\mathrm{cc}} \propto \theta\, N_{\mathrm{m}}$. However we have to consider relaxation parallel and perpendicular to the PE chain separately. In the former case the characteristic length is given by the PE extension $\Delta \propto a_{\mathrm{m}} N_{\mathrm{m}}$, leading to the scaling relations [47]

$$\Delta\chi_{\mathrm{cc},\parallel} \propto \frac{\theta\,\ell_{\mathrm{B}}}{a_{\mathrm{m}}}\, N_{\mathrm{m}}^{0} \left(\frac{c_{\mathrm{m}}}{c_{\mathrm{m}}^{*}}\right)^{1} \tag{3.26}$$

and

$$\tau_{\mathrm{cc},\parallel} \propto \frac{\zeta_{\mathrm{ct}} a_{\mathrm{m}}^{2}}{\mathrm{k_B} T}\, N_{\mathrm{m}}^{2} \left(\frac{c_{\mathrm{m}}}{c_{\mathrm{m}}^{*}}\right)^{0} . \tag{3.27}$$

The relaxation perpendicular to the PE axis is associated with the PE width, $\Delta \propto a_\mathrm{m}$, in that case

$$\Delta\chi_{\mathrm{cc},\perp} \propto \frac{\theta\,\ell_\mathrm{B}}{a_\mathrm{m}}\,N_\mathrm{m}^{-2}\left(\frac{c_\mathrm{m}}{c_\mathrm{m}^*}\right)^1 \tag{3.28}$$

and

$$\tau_{\mathrm{cc},\perp} \propto \frac{\zeta_\mathrm{ct} a_\mathrm{m}^2}{\mathrm{k_B}T}\,N_\mathrm{m}^0\left(\frac{c_\mathrm{m}}{c_\mathrm{m}^*}\right)^0 . \tag{3.29}$$

Note that on the scaling level the difference between Eqns. (3.26), (3.27) on the one hand and Eqns. (3.28), (3.29) on the other hand lies in the PE length dependence alone. While the static dielectric susceptibility in the parallel case is length independent, it decreases with length in the perpendicular case. Conversely, the relaxation time in parallel direction increases with length while it is length independent in perpendicular direction.

Similar PE concentration and length dependence of the static dielectric susceptibility of condensed counterions parallel and perpendicular to the PE axis can be extracted from the model due to Schlagberger and Netz [19]. For parallel relaxation the scaling relations agree with Ozawa's models [54].

Critique and perspectives

The experimental verification of the scaling relations derived above faces one major challenge. In order to ultimately sort out which relaxation mode correlates with uncondensed or condensed counterions and parallel or perpendicular direction, it is not sufficient to compare measurements with scaling relations. In this respect the correlation of measurements with scaling relations provides evidence, but no proof, that the assumed physical picture is correct. In case of the relaxation direction, complementary birefringence experiments allow for the discrimination of different directions (albeit without gauge). But there is no counterion specific parameter allowing for the discrimination of uncondensed and condensed counterions.

The scaling predictions derived above do not account for the corrugation of the electrostatic potential experienced by the counterions on length scales larger than the PE correlation length. In fact, we expect a relaxation mechanism to be of importance, where counterions cross potential barriers separating different PE chains. In a bistable potential, this overbarrier relaxation process is known to depend on the barrier height and dominates the low-frequency response, in contrast to relaxation in the individual potential wells which is barrier-height independent and characteristic for the high-frequency

response [85]. Indeed, within multi-PE simulations we find that the lowest frequency relaxation process is obviously related to barrier crossing.

3.2. Model and measurements

We consider N_p PE chains of N_m charged monomers of radius $a_\mathrm{m} = a_\mathrm{ct}$, and $N_\mathrm{ct} = N_\mathrm{m}$ counterions of radius a_ct, confined in a cubic cell of volume V. The overall cell is electroneutral,

$$q_\mathrm{m} N_\mathrm{m} N_\mathrm{p} + q_\mathrm{ct} N_\mathrm{ct} = 0 \tag{3.30}$$

where $q_\mathrm{m} = +1$ and $q_\mathrm{ct} = -1$ denote the charge valency of a monomer or counterion, respectively. Periodic boundary conditions are implemented via the minimum image convention [86].

All particles evolve according to the Langevin equation Eq. (2.1), where the hydrodynamic coupling is accounted for via the Rotne-Prager-Yamakawa tensor Eqns. (2.3) and (2.4). We apply a time-periodic external electric potential,

$$\frac{U_\mathrm{ext}}{\mathrm{k_B}T} = -\frac{\mathrm{e}}{\mathrm{k_B}T} \sum_i q_i \, \boldsymbol{r}_i \cdot \boldsymbol{E}_0 \cos(\omega t), \tag{3.31}$$

where $\boldsymbol{E}_0 = E_0 \, \hat{\mathbf{e}}_z$ denotes the field strength.

Within simulations, the fluctuating dipole density $\Delta\boldsymbol{P}(t)$ due to N particles of charge q_i at position $\boldsymbol{r}_i(t)$ in a cell of volume V can be calculated according to

$$\Delta\boldsymbol{P}(t) = \frac{1}{V}\frac{1}{N} \sum_{i,j=1}^{N} q_i \left[\boldsymbol{r}_i(t) - \boldsymbol{r}_j(t)\right] . \tag{3.32}$$

The dipole density calculated this way is explicitly independent of the choice of the origin. Likewise, partial fluctuating dipole densities $\Delta\boldsymbol{P}_\mathrm{cc}(t)$, $\Delta\boldsymbol{P}_\mathrm{uc}(t)$ for condensed or uncondensed counterions follow from Eq. (3.32) by constraining the summation to the respective counterion subpopulation, hence

$$\Delta\boldsymbol{P}_\mathrm{cc}(t) = \frac{1}{V}\frac{1}{N} \sum_{i,j=1}^{N_\mathrm{m}+\theta N_\mathrm{c}} q_i \left[\boldsymbol{r}_i(t) - \boldsymbol{r}_j(t)\right] \tag{3.33}$$

and

$$\Delta\boldsymbol{P}_\mathrm{uc}(t) = \frac{1}{V}\frac{1}{N} \sum_{i,j=1}^{N_\mathrm{m}+(1-\theta)N_\mathrm{c}} q_i \left[\boldsymbol{r}_i(t) - \boldsymbol{r}_j(t)\right] . \tag{3.34}$$

We have $\Delta \boldsymbol{P}(t) = \Delta \boldsymbol{P}_{\mathrm{cc}}(t) + \Delta \boldsymbol{P}_{\mathrm{uc}}(t)$. Note that the partial dipole densities Eqns. (3.33) and (3.34) are still independent of the choice of the origin.

Specializing to a time-periodic field $\boldsymbol{E}(t) = E_0 \cos(\omega t)\, \hat{\mathbf{e}}_z$ the frequency dependent dielectric susceptibility $\Delta\chi(\omega)$ follows as

$$\Delta\chi(\omega) = \frac{2}{\epsilon_0 E_0} \left\langle \Delta P_z(\omega) \right\rangle , \tag{3.35}$$

where the frequency dependent dipole density $\left\langle \Delta P_z(\omega) \right\rangle$ follows from the Fourier-transform

$$\left\langle \Delta P_z(\omega) \right\rangle = \frac{1}{T} \int_0^T \mathrm{d}t \, \left\langle \Delta P_z(t) \right\rangle \, \mathrm{e}^{-\mathrm{i}\omega t} . \tag{3.36}$$

Expressed through dimensionless quantities we find for real part $\Delta\chi\prime(\tilde{\omega})$ and imaginary part $\Delta\chi\prime\prime(\tilde{\omega})$ of the frequency-dependent dielectric susceptibility

$$\Delta\chi\prime(\tilde{\omega}) = 16\pi\xi_{\mathrm{M}}\epsilon_{\mathrm{H_2O}} \frac{1}{\tilde{T}} \int_0^{\tilde{T}} \mathrm{d}\tilde{t} \, \left\langle \Delta\tilde{P}_z(\tilde{t}) \right\rangle \cos(\tilde{\omega}\tilde{t}) \tag{3.37}$$

and

$$\Delta\chi\prime\prime(\tilde{\omega}) = 16\pi\xi_{\mathrm{M}}\epsilon_{\mathrm{H_2O}} \frac{1}{\tilde{T}} \int_0^{\tilde{T}} \mathrm{d}\tilde{t} \, \left\langle \Delta\tilde{P}_z(\tilde{t}) \right\rangle \sin(\tilde{\omega}\tilde{t}) \tag{3.38}$$

The analysis of the dielectric spectrum obtained from simulations follows the assumption of two distinct relaxation processes – which we refer to as low-frequency (LF) and high-frequency (HF) process – as commonly observed in experiment. As discussed in Section 3.1 we model the spectrum via two Cole-Cole functions

$$\Delta\chi(\tilde{\omega}) = \frac{\Delta\chi^{(0)}_{\mathrm{LF}}}{1 + (\mathrm{i}\tilde{\omega}\tilde{\tau}_{\mathrm{LF}})^{\alpha_{\mathrm{LF}}}} + \frac{\Delta\chi^{(0)}_{\mathrm{HF}}}{1 + (\mathrm{i}\tilde{\omega}\tilde{\tau}_{\mathrm{HF}})^{\alpha_{\mathrm{HF}}}} , \tag{3.39}$$

where the parameters $\Delta\chi^{(0)}_{\mathrm{LF}}$, $\tilde{\tau}_{\mathrm{LF}}$ and α_{LF} ($\Delta\chi^{(0)}_{\mathrm{HF}}$, $\tilde{\tau}_{\mathrm{HF}}$ and α_{HF}) denote strength, relaxation time, and stretching exponent of the LF (HF) relaxation process. Fitting of Eq. (3.39) to the simulation data is done through a weighted non-linear least squares fit. Both real and imaginary part of the dielectric susceptibility are fitted simultaneously.

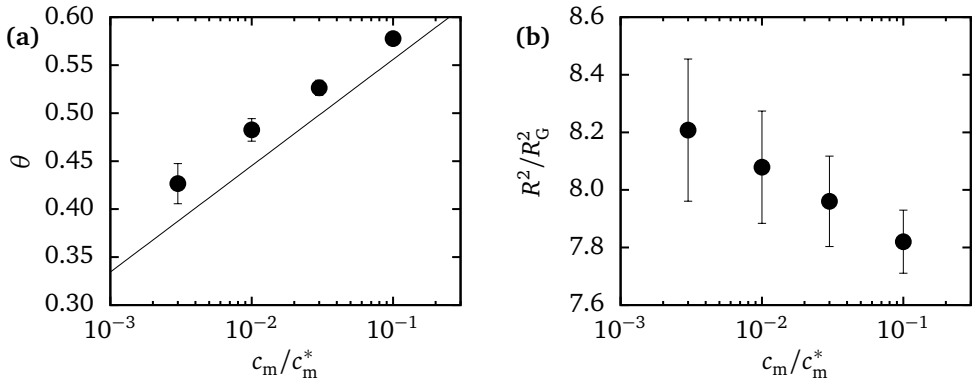

Figure 3.1.: Simulations at fixed monomer number $N_m = 16$ and various scaled monomer concentrations c_m/c_m^*. (a) Fraction of condensed counterions θ (symbols) as a function of the scaled monomer concentration c_m/c_m^*, together with the theoretical prediction Eq. (3.40) (line). (b) Ratio of the average squared end-to-end distance and the average squared radius of gyration R^2/R_G^2 as a function of the scaled monomer concentration c_m/c_m^*.

3.3. Results and Discussion

3.3.1. Fixed length, variable scaled monomer concentration

We perform simulations of a single PE chain with monomer number $N_m = 16$ and $N_{ct} = N_m$ neutralizing counterions. The scaled PE monomer concentration $c_m/c_m^* = (2a_m N_m)^3/V$ is varied over the range $c_m/c_m^* = 0.003 - 0.1$. The Manning parameter is fixed at $\xi_M = 3$ as applicable to typical synthetic PEs.

Counterion condensation and PE conformation

Netz [18] presents a Flory-type argument for the fraction of condensed counterions θ in salt-free PE solutions which accounts for both finite PE length and concentration,

$$\theta = 1 - \frac{1}{\xi_M}\left[1 + \frac{\ln(c_m/c_m^*)}{\ln(L_0/a_m)}\right]. \tag{3.40}$$

In the derivation of Eq. (3.40) the PE chain is assumed to be fully extended. According to Eq. (3.40), the fraction of condensed counterions θ increases logarithmically with scaled monomer concentration and decreases inverse-logarithmically with PE contour length. The scaled monomer concentration dependence of the fraction of condensed counterions θ is stronger than the PE length dependence. A similar relation has been worked out by Ramanathan and Woodbury [87, 88]. In simulations, the fraction of condensed counterions θ is defined as the fraction of counterions within a distance $5a$ from

the center of a monomer. Comparison of theory Eq. (3.40) and simulation is almost quantitative, cf. Fig. 3.1, which is remarkable in view of our *ad hoc* definition of the fraction of condensed counterions.

The variation of the fraction of condensed counterions with scaled monomer concentration has important consequences for the conformation of a PE chain, as condensed counterions shield the electrostatic repulsion between charged monomers. We characterize the PE conformation via the ratio of the average squared end-to-end distance and the average squared radius of gyration R^2/R_G^2. The average squared end-to-end distance is defined as

$$R^2 = \left\langle \left(\boldsymbol{r}_{N_m} - \boldsymbol{r}_1 \right)^2 \right\rangle , \tag{3.41}$$

and the average squared radius of gyration as

$$R_G^2 = \left\langle \frac{1}{N_m} \sum_{i=1}^{N_m} \left(\boldsymbol{r}_i - \boldsymbol{r}_{com} \right)^2 \right\rangle , \tag{3.42}$$

where $\boldsymbol{r}_{com} = \sum_{i=1}^{N_m} \boldsymbol{r}_i / N_m$ is the center of mass of a PE chain. For a flexible chain in a theta solvent one expects $R^2/R_G^2 = 6$, for a flexible chain in a good solvent $R^2/R_G^2 \approx 6.3$, and for rodlike chains $R^2/R_G^2 = 12$. In agreement with previous simulations [89, 90] we find $7.8 < R^2/R_G^2 < 8.2$ which corresponds to extended, but not rodlike conformations, cf. Fig. 3.1. The extended PE conformation arises from electrostatic repulsion between charged monomers, which is regulated by the fraction of condensed counterions θ. An increasing fraction of condensed counterions with scaled monomer concentration, cf. Fig. 3.1, mitigates the electrostatic repulsion between charged monomers, eventually shrinking the PE chain extension as manifest in the variation of the ratio R^2/R_G^2 with scaled monomer concentration.

Dielectric response

We analyze the complex dielectric susceptibility $\Delta\chi(\tilde{\omega})$ through simultaneously fitting a sum of two CC-functions Eq. (3.39) to real part $\Delta\chi'(\tilde{\omega})$ and imaginary part $\Delta\chi''(\tilde{\omega})$ as described above. In Fig. 3.2 a) and b) where we show real part and imaginary part of the dielectric susceptibility as a function of the dimensionless radial frequency $\tilde{\omega}$ of the external electric field, full fitting results appear as solid lines, contributions of the individual CC-functions for scaled monomer density $c_m/c_m^* = 0.003$ as broken lines. Note that the fits are satisfactory albeit not perfect, as the peak height in the imaginary

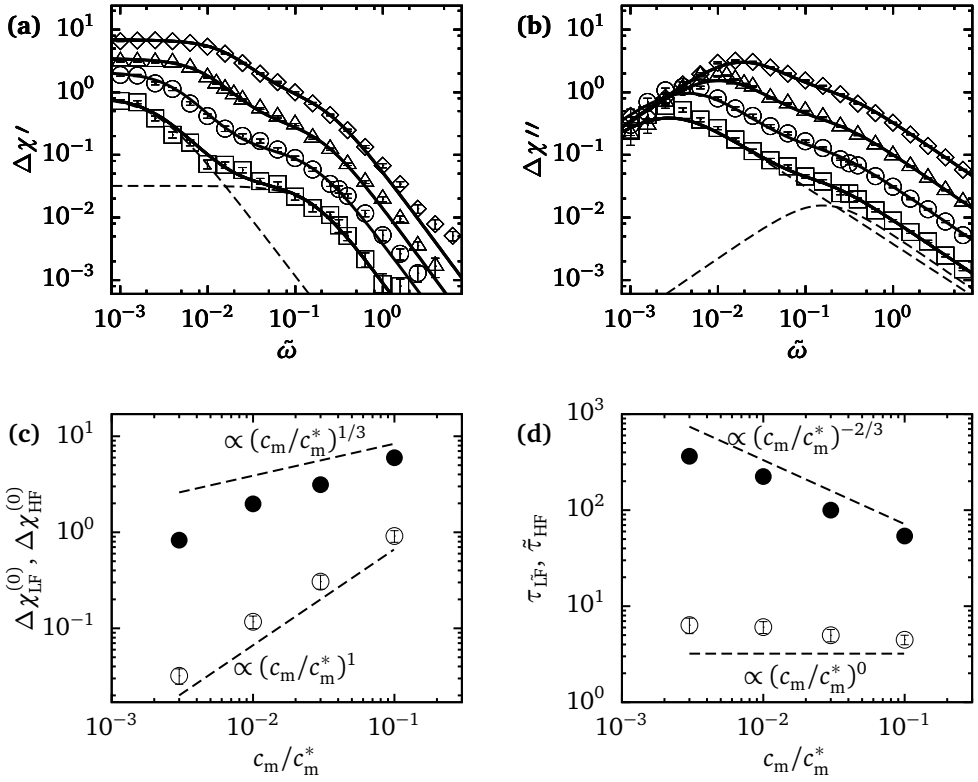

Figure 3.2.: Simulations for fixed monomer number $N_{\rm m} = 16$ and variable scaled monomer concentration $c_{\rm m}/c^*_{\rm m} = 0.003, 0.01, 0.03, 0.1$. (a) Real part of the dielectric susceptibility $\Delta\chi\prime(\tilde{\omega})$ as a function of the radial frequency $\tilde{\omega}$ as obtained from simulations ($c_{\rm m}/c^*_{\rm m} = 0.1$ – diamonds, $c_{\rm m}/c^*_{\rm m} = 0.03$ – triangles, $c_{\rm m}/c^*_{\rm m} = 0.01$ – circles, $c_{\rm m}/c^*_{\rm m} = 0.003$ – squares). The dielectric susceptibility can be modeled by two CC-functions (solid lines: fitting results; broken lines: individual fitting results for $c_{\rm m}/c^*_{\rm m} = 0.003$). (b) Imaginary part of the dielectric susceptibility $\Delta\chi\prime\prime(\tilde{\omega})$ as a function of the radial frequency $\tilde{\omega}$ as obtained from simulations. (c): Fit parameters. Amplitudes of LF (filled circles) and HF (open circles) relaxation mode $\Delta\chi^{(0)}_{\rm LF}$, $\Delta\chi^{(0)}_{\rm HF}$ as a function of the scaled monomer concentration $c_{\rm m}/c^*_{\rm m}$. (d): Fit parameters. Relaxation times of LF (filled circles) and HF (open circles) relaxation mode $\tilde{\tau}_{\rm LF}$, $\tilde{\tau}_{\rm HF}$ as a function of the scaled monomer concentration $c_{\rm m}/c^*_{\rm m}$.

part $\Delta\chi''(\tilde{\omega})$ is systematically underestimated. All in all, agreement gets better with increasing scaled monomer density.

The fit exponents $\alpha_{\mathrm{LF}}, \alpha_{\mathrm{HF}}$ are close to unity indicating that both LF and HF relaxation process are more or less of Debye type. In Fig. 3.2 c) and d) we plot relaxation times $\tilde{\tau}_{\mathrm{LF}}$, $\tilde{\tau}_{\mathrm{HF}}$ and strengths $\Delta\chi^{(0)}_{\mathrm{LF}}$, $\Delta\chi^{(0)}_{\mathrm{HF}}$ of the LF and HF relaxation process against the scaled monomer concentration $c_{\mathrm{m}}/c^{*}_{\mathrm{m}}$. For the concentration regime under consideration the LF process clearly dominates the HF process by about an order of magnitude in strength. The strength of the LF process $\Delta\chi^{(0)}_{\mathrm{LF}}$ grows more slowly with scaled monomer concentration than the strength of the HF process $\Delta\chi^{(0)}_{\mathrm{HF}}$. LF and Hf process are separated by more than an order of magnitude in time, with the separation decreasing with scaled monomer concentration.

At first glance our simulation results are at variance with experiment, where the relaxation strength of the LF process increases at higher rate than the relaxation strength of the HF process, and where the relaxation time of the LF process is independent of the scaled monomer concentration while the relaxation time of the HF process is not [35–37, 39–41]. Moreover, within experiment the LF relaxation strength is smaller than the HF relaxation strength. All in all, in our simulations the characteristics of LF and HF relaxation process appear to be interchanged as compared to experiment. As we will show in the multi-PE simulations below, this is due to the absence of interactions between different PE-counterion atmosphere complexes in single-PE simulations.

From the foregoing qualitative considerations we expect the LF process to correlate with scaling predictions for the relaxation of uncondensed counterions Eqns. (3.24) and (3.25), whereas we expect the HF process to correlate with scaling predictions for condensed counterions Eqns. (3.26) and (3.27) or Eqns. (3.28) and (3.29), respectively. (Recall that in case of the relaxation of condensed counterions no distinction between parallel or perpendicular relaxation can be made based on the dependence on scaled monomer concentration alone.) We indeed find reasonable agreement, cf. Fig. 3.2 c) and d). We do not want to conceal small deviations from scaling, though, which we partially ascribe to variations of the fraction of condensed counterions and the PE conformation with scaled monomer concentration.

Compliance of the relaxation parameters with the scaling predictions provides strong but not definite evidence, that the theoretical premises reflect the particular physical mechanisms. Within simulations, unambiguous verification as to the origin of LF and HF relaxation process can be accomplished through separately analyzing the dielectric susceptibilities $\Delta\chi_{\mathrm{cc}}(\tilde{\omega})$, $\Delta\chi_{\mathrm{uc}}(\tilde{\omega})$ due to condensed and

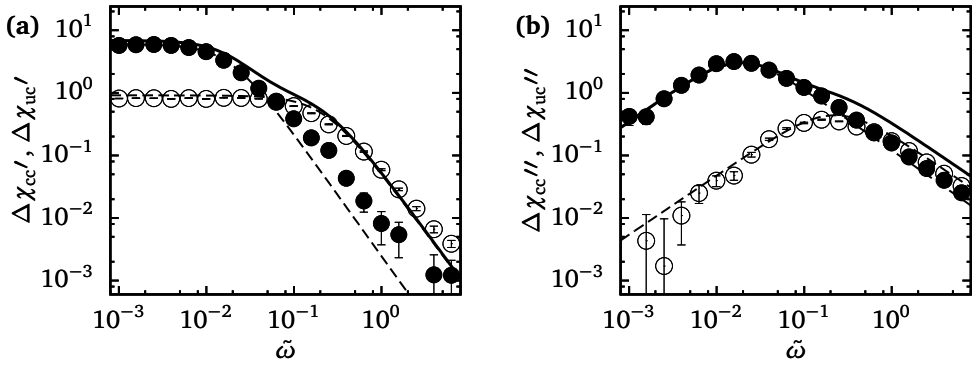

Figure 3.3.: Simulations at fixed monomer number $N_m = 16$ and scaled monomer concentration $c_m/c_m^* = 0.1$. Dielectric response of condensed counterions $\Delta\chi_{cc}(\tilde{\omega})$ (open circles) and uncondensed counterions $\Delta\chi_{uc}(\tilde{\omega})$ (filled circles). Lines are fitting results to the dielectric response of all counterions, cf. Fig. 3.2. (a): Real part $\Delta\chi_{cc}'(\tilde{\omega})$, $\Delta\chi_{uc}'(\tilde{\omega})$ of the dielectric susceptibility. (b): Imaginary part $\Delta\chi_{cc}''(\tilde{\omega})$, $\Delta\chi_{uc}''(\tilde{\omega})$ of the dielectric susceptibility.

uncondensed counterions. The dielectric susceptibilities $\Delta\chi_{cc}(\tilde{\omega})$, $\Delta\chi_{uc}(\tilde{\omega})$ due to condensed and uncondensed counterions can be obtained from the respective average dipole density Eqns. (3.33) and (3.34). As an example we show real part and imaginary part of the dielectric susceptibility due to condensed and uncondensed counterions at scaled monomer density $c_m/c_m^* = 0.1$ in Fig. 3.3. Comparison with the CC-functions as fitted to the dielectric susceptibility due to all counterions clearly correlates the relaxation of condensed counterion with the HF process, and the relaxation of uncondensed counterions with the LF process. A correlation analysis of the relaxation parameters of condensed and uncondensed counterions as obtained from fits of a single CC-function to the respective dielectric susceptibility and the relaxation parameters of LF and HF relaxation process yields excellent agreement which proves the assignments condensed counterions – HF process and uncondensed counterions – LF process, consistent with the scaling predictions. In view of our arbitrarily chosen criterion defining condensed and uncondensed counterions, the near to quantitative agreement between both sets of relaxation parameters should be taken with a pinch of salt, though.

3.3.2. Variable length, fixed scaled PE concentration

Within the common experimental protocol the PE contour length $L_0 = 2a_m N_m$ is varied at fixed monomer concentration c_m. In order to disentangle the influence of PE contour length and monomer concentration on the dielectric susceptibility, we propose to vary the PE contour length at fixed scaled monomer concentration $c_m/c_m^* = L_0^3/V$. This amounts to a change of the PE length without changing

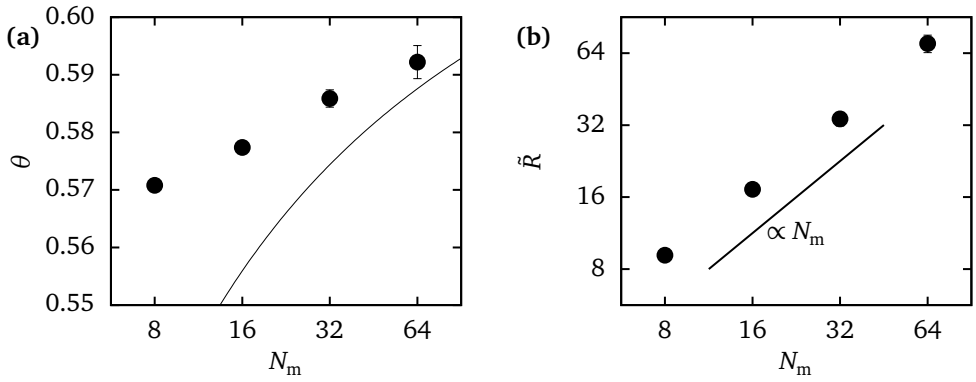

Figure 3.4.: Simulations for variable monomer number N_m and fixed scaled monomer concentration $c_m/c_m^* = 0.10$. (a) Fraction of condensed counterions θ (symbols) as a function of the monomer number N_m, together with the theoretical prediction Eq. (3.40) (line). (b) Average end-to-end distance $\tilde{R}$ as a function of the monomer number N_m.

the structure of the PE solution. More precisely we perform simulations of a single PE chain with variable monomer number $N_m = 8, 16, 32, 64$ and $N_{ct} = N_m$ neutralizing counterions at scaled monomer concentration $c_m/c_m^* = 0.1$. As before, the Manning parameter is fixed at $\xi_M = 3$.

Counterion condensation and PE conformation

From theoretical considerations, cf. Eq. (3.40), the fraction of condensed counterions θ is predicted to increase with PE length, which we find confirmed in Fig. 3.4 where we plot the fraction of condensed counterions θ as obtained from simulations. We do see qualitative deviations from the predicted inverse-logarithmic length dependence, which we ascribe to strong deviations from the extended conformation entering theory, plus our *ad hoc* definition of the fraction of condensed counterions. What is important here is that changes in the fraction of condensed counterions are marginal such that we expect no or only little changes in PE conformation due to counterion condensation.

As stated before, in dilute, salt-free solution a PE chain adopts an extended conformation where the end-to-end distance scales linearly with the monomer number $R \sim a_m N_m$ [91]. Indeed, we observe close to linear scaling of the end-to-end distance with the monomer number within simulations, cf. Fig. 3.4, although the simulated monomer numbers are rather small. However, the end-to-end distance is much smaller than the contour length $L_0 = 2a_m N_m$ hinting at a crumpling of the PE chain on small scales [89, 90, 92–94].

Dielectric response

In Fig. 3.5 a) and b) we show real part $\Delta\chi'(\tilde{\omega})$ and imaginary part $\Delta\chi''(\tilde{\omega})$ of the dielectric susceptibility as a function of the radial frequency $\tilde{\omega}$ of the external electric field. As before, on a double-logarithmic scale two relaxation processes can be clearly distinguished.

Similar to our simulations with varying scaled monomer concentration we find fit exponents $\alpha_{\mathrm{LF}}, \alpha_{\mathrm{HF}}$ close to unity. In Fig. 3.5 c) and d) we plot relaxation time and strength of the LF and HF relaxation process against the monomer number N_{m}. Complying with our findings for fixed length and varying scaled monomer concentration, cf. Fig. 3.2, the LF process clearly dominates the HF process, where the strength of the LF process $\Delta\chi_{\mathrm{LF}}^{(0)}$ decreases more slowly with the monomer number than the strength of the HF process $\Delta\chi_{\mathrm{HF}}^{(0)}$. LF and Hf process are separated by about an order of magnitude in time, with the separation increasing with monomer number.

We compare the monomer number dependence of strength and relaxation time of the LF and HF relaxation process at fixed scaled monomer concentration with scaling predictions. In contrast to our findings for fixed length and varying scaled monomer concentration we find poor agreement of the LF process with the scaling predictions, cf. Fig. 3.5 c) and d). The strength of the LF process $\Delta\chi_{\mathrm{LF}}^{(0)}$ deviates considerably from the scaling prediction Eq. (3.24), decreasing with monomer number. The LF relaxation time $\tilde{\tau}_{\mathrm{LF}}$ increases with monomer number as predicted by Eq. (3.25) albeit with a smaller power. The direction of the deviations towards smaller scaling exponents appears to be similar to what has been observed in experiments on ss-DNA in salt-free solution [34]. In these experiments the deviations are not as large, though. Comparison of the HF relaxation strength $\Delta\chi_{\mathrm{HF}}^{(0)}$ and relaxation time $\tilde{\tau}_{\mathrm{LF}}$ with the scaling predictions for condensed counterions yields fair agreement with Eqns. (3.28) and (3.29) for perpendicular relaxation, while Eqns. (3.26) and (3.27) for parallel relaxation of the condensed counterions fail to describe the data. Similar scaling for the perpendicular relaxation of condensed counterions has been found within simulations of short rodlike PEs in salt solution [19].

Fair agreement between the scaling predictions for perpendicular relaxation of condensed counterions with our fit results fuels our discussion as to the origin of the HF process. Indeed, provided the HF process we observe within simulations is due to the relaxation of condensed counterions perpendicular to the PE, then we probably miss the contribution due to the parallel relaxation of condensed counterions, which should be larger than the former. In order to get more structural insight, we push our

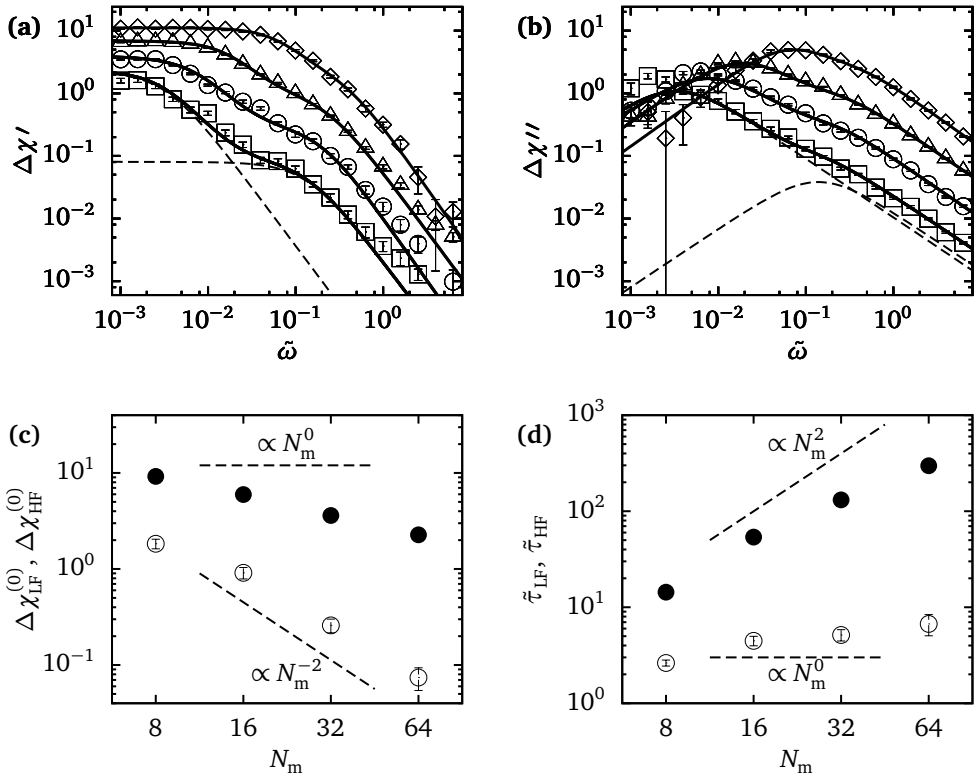

Figure 3.5.: Simulations for variable monomer number $N_m = 16, 32, 64, 128$ and fixed scaled monomer concentration $c_m/c_m^* = 0.10$. (a) Real part of the dielectric susceptibility $\Delta\chi\prime(\tilde{\omega})$ as a function of the radial frequency $\tilde{\omega}$ as obtained from simulations ($N_m = 8$ – diamonds, $N_m = 16$ – triangles, $N_m = 32$ – circles, $N_m = 64$ – squares). The dielectric susceptibility can be modeled by two CC-functions (solid lines: fitting results; broken lines: individual fitting results for $N_m = 64$). (b) Imaginary part of the dielectric susceptibility $\Delta\chi\prime\prime(\tilde{\omega})$ as a function of the radial frequency $\tilde{\omega}$ as obtained from simulations. (c): Fit parameters. Amplitudes of LF (filled circles) and HF (open circles) relaxation mode $\Delta\chi_{LF}^{(0)}$, $\Delta\chi_{HF}^{(0)}$ as a function of monomer number N_m. (d): Fit parameters. Relaxation times of LF (filled circles) and HF (open circles) relaxation mode $\tilde{\tau}_{LF}$, $\tilde{\tau}_{HF}$ as a function of monomer number N_m.

analysis further and try to figure out whether the correlation HF process – perpendicular relaxation of condensed counterions exists.

Further decomposition of the fluctuating dipole density in contributions parallel or perpendicular with respect to the direction of the PE principal axis can be done according to

$$\Delta\tilde{P}_{\parallel}(\tilde{t}) = \Delta\tilde{P}_{z}(\tilde{t})\,\mathrm{e}_{\parallel,z} \tag{3.43}$$

and

$$\Delta\tilde{P}_{\perp}(\tilde{t}) = \Delta\tilde{P}_{z}(\tilde{t}) - \Delta\tilde{P}_{\parallel}(\tilde{t}), \tag{3.44}$$

where $\mathrm{e}_{\parallel,z}$ is the z-component of the (normalized) eigenvector corresponding to the largest eigenvalue of the PE gyration tensor. From the corresponding dielectric susceptibilities $\Delta\chi_{\parallel}(\tilde{\omega})$ and $\Delta\chi_{\perp}(\tilde{\omega})$, cf. Fig. 3.6 (a) and (b) we readily see, that parallel and perpendicular relaxation contribute equally to both HF and LF process, where the parallel relaxation always exceeds the perpendicular relaxation in accord with previous observations within simulations of rodlike PEs [19, 74–77]. Likewise, the parallel dielectric susceptibility of condensed counterions is substantially higher than the perpendicular dielectric susceptibility of condensed counterions, cf. Fig. 3.6 (c) and (d) which contradicts our expectations based on comparison with the scaling predictions. As opposed to the rodlike case, where the parallel dielectric susceptibility of the condensed counterions $\Delta\chi_{\parallel,\mathrm{cc}}(\tilde{\omega})$ stays constant and the perpendicular dielectric susceptibility of the condensed counterions $\Delta\chi_{\perp,\mathrm{cc}}(\tilde{\omega})$ decreases with the inverse second power of the monomer number N_{m} [19] which complies with the scaling predictions Eqns. (3.26) and (3.28), we find that both parallel and perpendicular dielectric susceptibilities of the condensed counterions decrease with the inverse second power of the monomer number (data not shown). The origin of this strong qualitative deviation of the parallel relaxation of condensed counterions from the scaling prediction might be found in the flexibility of the PE chain. For flexible PE chains, the gain of conformational entropy might exceed electrostatic repulsion such that the PE chain appears to be crumpled on short length scales. In this case condensed counterions move in a locally inhomogeneous potential, as opposed to the case of rodlike PEs where the potential is more or less homogeneous. The characteristic length of the PE chain crumpling is provided by the size of a PE monomer $\Delta \propto a_{\mathrm{m}}$, similar to the characteristic length entering the scaling predictions for perpendicular relaxation Eqns. (3.28)

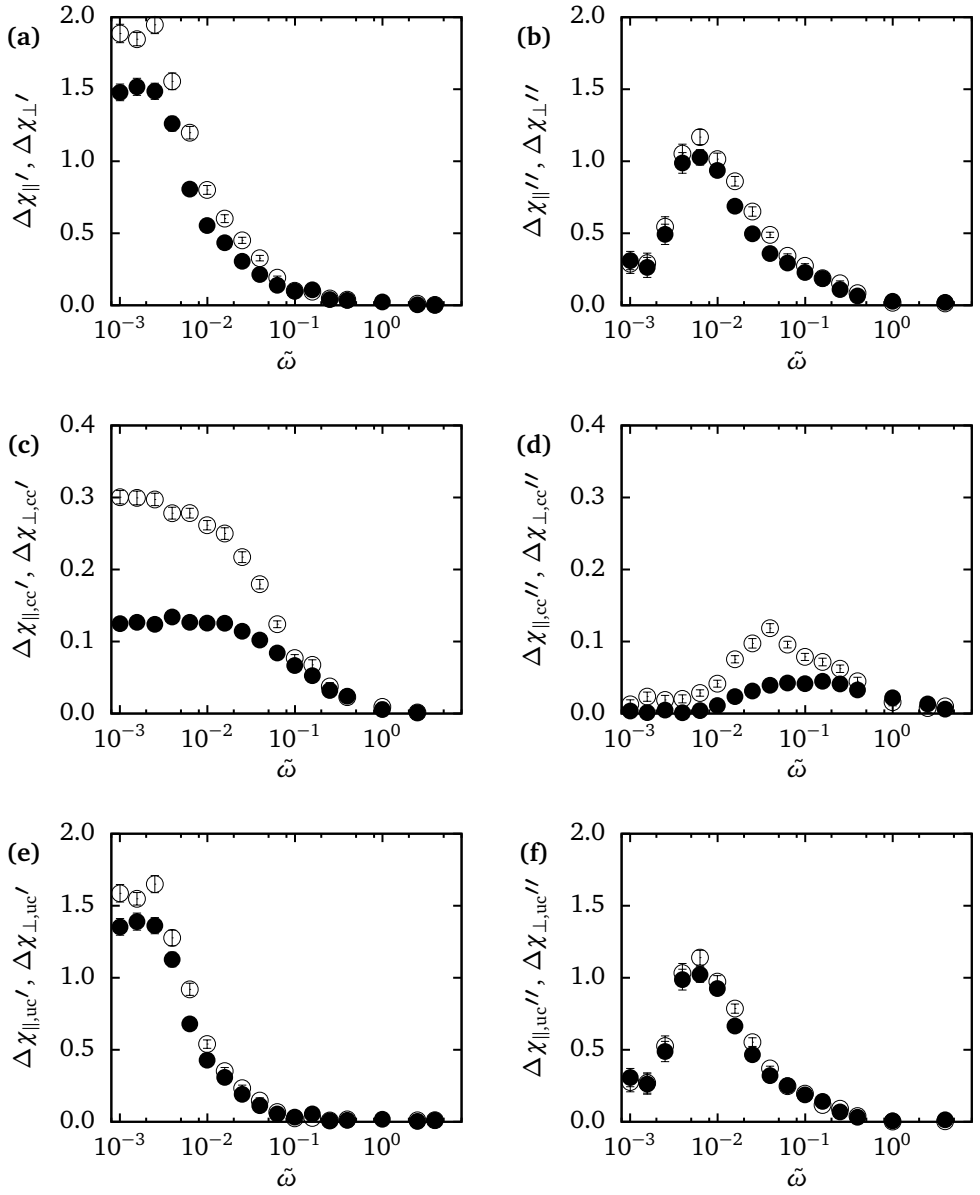

Figure 3.6.: Simulations for monomer number $N_\mathrm{m} = 32$ and scaled monomer concentration $c_\mathrm{m}/c_\mathrm{m}^* = 0.10$. Parallel dielectric susceptibility $\Delta\chi_\parallel(\tilde{\omega})$ (open circles) and perpendicular dielectric susceptibility $\Delta\chi_\perp(\tilde{\omega})$ (filled circles) as a function of the radial frequency $\tilde{\omega}$ as obtained from simulations. (a) and (b) Real part and imaginary part of the parallel and perpendicular dielectric susceptibility due to all counterions. (c) and (d) Real part and imaginary part of the parallel and perpendicular dielectric susceptibility due to condensed counterions. (e) and (f) Real part and imaginary part of the parallel and perpendicular dielectric susceptibility due to uncondensed counterions.

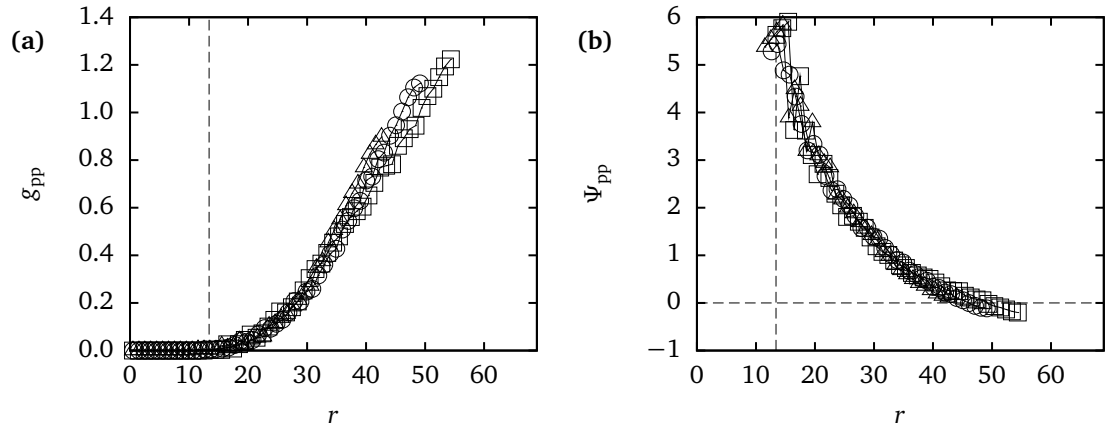

Figure 3.7.: Simulations for fixed monomer number $N_m = 16$, fixed scaled PE concentration $c_m/c_m^* = 0.10$ and variable PE number $N_p = 2$ (triangles), $N_p = 3$ (circles), $N_p = 4$ (squares). (a) PE-PE radial distribution function $g_{pp}(r)$ as a function of the PE=PE distance r. (b) Dimensionless PE-PE potential of mean force $\Psi_{pp}(r)$ as a function of the PE-PE distance r.

and (3.29). We note in passing, that the dielectric response of the uncondensed counterions is nearly isotropic, cf. Fig. 3.6 (e) and (f).

3.3.3. Multi-PE simulations – correlation effects

In this section we study the influence of interactions among different PE-counterion atmosphere complexes in extension to our preceding discussion of the dielectric relaxation of one single PE-counterion atmosphere complex. From simulations of a minimal model for the dielectric relaxation of PE solutions we thus take steps towards simulations of more realistic models. This comes at the cost of gradually increasing the model complexity, not to mention the mounting computational expense. Technically we include interactions among different PE-counterion atmosphere complexes by varying the number of PEs in the simulations cell $N_p = 1, 2, 3, 4$ at fixed monomer number per PE $N_m = 16$ and fixed scaled monomer concentration $c_m/c_m^* = N_p N_m^3/V = 0.10$.

Structure of the PE solution

Simulations of a single PE with its counterion atmosphere do not allow to make a point concerning the spatial arrangement of a number of PEs. Here we access the structure of the PE solution by considering the PE-PE and PE-counterion radial distribution functions $g_{\mathrm{pp}}(r)$ and $g_{\mathrm{pc}}(r)$, defined as

$$g_{\mathrm{pp}}(r) = \frac{V}{N_{\mathrm{p}}^2} \sum_{i=1}^{N_{\mathrm{p}}} {\sum_{j=1}^{N_{\mathrm{p}}}}' \frac{\delta\left(r - |\boldsymbol{r}_{\mathrm{p},i} - \boldsymbol{r}_{\mathrm{p},j}|\right)}{4\pi r^2} \tag{3.45}$$

and

$$g_{\mathrm{pc}}(r) = \frac{V}{N_{\mathrm{c}} N_{\mathrm{p}}} \sum_{i=1}^{N_{\mathrm{p}}} \sum_{j=1}^{N_{\mathrm{c}}} \frac{\delta\left(r - |\boldsymbol{r}_{\mathrm{p},i} - \boldsymbol{r}_{\mathrm{c},j}|\right)}{4\pi r^2} \,. \tag{3.46}$$

In this context $\boldsymbol{r}_{\mathrm{p},i}$ and $\boldsymbol{r}_{\mathrm{c},j}$ denote the center-of-mass positions of the i-th PE and the j-th counterion, respectively, and the primed sum in Eq. (3.45) excludes terms with index $j = i$. The radial distribution functions $g_{\mathrm{pp}}(r)$ and $g_{\mathrm{pc}}(r)$ capture the local structure of the PE solution surrounding a reference PE in terms of distance-dependent variations of the PE or counterion density. Simple Boltzmann inversion relates the PE-PE and PE-counterion radial distribution functions to the dimensionless PE-PE and PE-counterion potentials of mean force (PMF) $\Psi_{\mathrm{pp}}(r)$ and $\Psi_{\mathrm{pc}}(r)$,

$$\Psi_{\mathrm{pp}}(r) = -\ln\left[g_{\mathrm{pp}}(r)\right] \tag{3.47}$$

and

$$\Psi_{\mathrm{pc}}(r) = -\ln\left[g_{\mathrm{pc}}(r)\right] \,. \tag{3.48}$$

The PMFs contain both electrostatic and entropic contributions. Note that in order to avoid cell geometry-induced artifacts we only consider radial distribution functions and PMFs at distances smaller than half the cell width.

In Fig. 3.7 we plot the PE-PE radial distribution function $g_{\mathrm{pp}}(r)$ Eq. (3.45) and the PE-PE PMF Eq. (3.47) obtained from simulations as a function of the radial distance r. We notice a correlation hole at short distances where the PE density is zero followed by an increase of the radial distribution function. The concept of a correlation hole has been first introduced in connection with solutions of neutral polymers [91] where it accounts for the exclusion of polymers from the domain of a reference polymer due to steric repulsion. In this context the size of the correlation hole conforms to the polymer

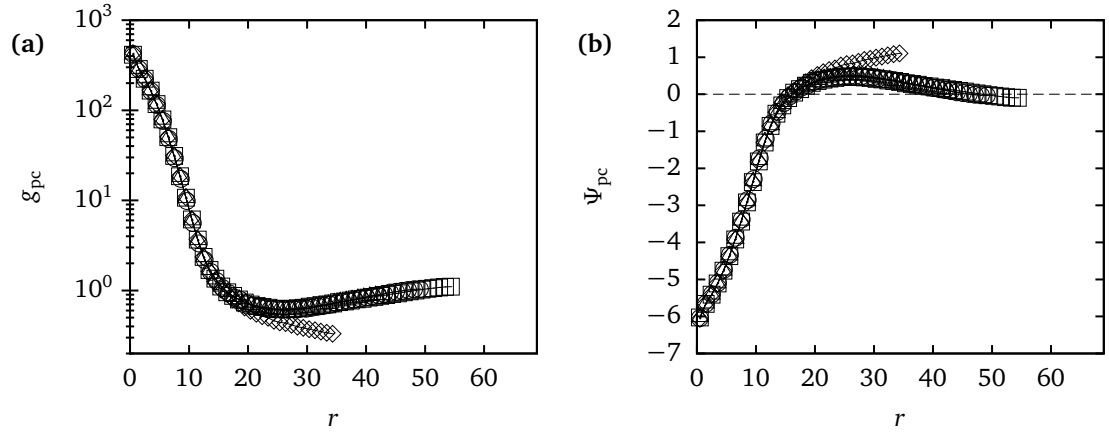

Figure 3.8.: Simulations for fixed monomer number $N_m = 16$, fixed scaled PE concentration $c_m/c_m^* = 0.10$ and variable PE number $N_p = 1$ (diamonds), $N_p = 2$ (triangles), $N_p = 3$ (circles), $N_p = 4$ (squares). (a) PE-counterion radial distribution function $g_{pc}(r)$ as a function of the PE-counterion distance r. (b) Dimensionless PE-counterion potential of mean force $\Psi_{pp}(r)$ as a function of the PE-counterion distance r.

size. Within PE solutions repulsive electrostatic interactions add to the steric repulsion. Here the size of the correlation hole is identified with the Debye screening length κ^{-1} rather than the PE size [95]. Owing to our choice of parameters we find the radius of the correlation hole similarly to be in the range of the average PE end-to-end distance $R/a = 17.24$ and the Debye screening length $1/\kappa a = 16.48$. This implies that PE chains do not interpenetrate on average. Hence the PE-PE PMF $\Psi_{pp}(r)$ is infinitely repulsive at short distances before decaying at longer distances. The appearance of a correlation hole at short distances and the subsequent increase of the PE-PE radial distribution function agree with the outcome of an earlier simulation study of dilute PE solutions [15]. But for the simple reason that the PE number and correspondingly the system size is still too small we do not observe the broad maximum at distances close to the PE correlation length $r = (V/N_p)^{1/3}$ reported in Refs. [14, 15, 90].

The PE-counterion radial distribution function $g_{pc}(r)$ is characterized by a high counterion density at short distances which strongly decreases over the PE-PE correlation hole, cf. Fig. 3.8. For a single PE, at larger distances the PE-counterion radial distribution function keeps decreasing, albeit at a smaller rate, reflecting the intrinsic inhomogeneity of the counterion density. For more than one PE the counterion density becomes homogeneous at larger distances from the reference PE, and the PE-counterion radial distribution function levels off after passing through a minimum.

Whereas interactions of the reference PE with its counterion atmosphere determine the PE-counterion radial distribution function inside of the PE-PE correlation hole, overlap of the counterion atmospheres

of different PEs determine the PE-counterion radial distribution function beyond the PE-PE correlation hole. This becomes more transparent in the PE-counterion PMF which reveals a potential barrier between different PEs originating from the overlap of the counterion atmospheres, as already anticipated in Section 3.1. The distance of the local maximum in the PE-counterion PMF from the reference PE, where no force acts on the counterions, could provide a measure for the non-overlapping part of the counterion atmosphere. This distance is significantly smaller than the extension of the counterion atmosphere which we define to be given by the distance where the number of counterions surrounding the reference PE $n_c = \int_0^r \mathrm{d}^3 r' g_{pc}(r') N_c/V$ equals the monomer number N_m. In our case the distance where the number of counterions surrounding the reference PE equals the monomer number exactly coincides with half the PE correlation length $r = (V/N_p)^{1/3}/2$.

Dielectric response

In Fig. 3.9 a) and b) we show real part $\Delta\chi'(\tilde{\omega})$ and imaginary part $\Delta\chi''(\tilde{\omega})$ of the dielectric susceptibility as a function of the radial frequency $\tilde{\omega}$ of the external electric field. (Notice the log-linear scale in contrast to the log-log scale used in Figs. 3.2 and 3.3.) The dielectric response exhibits a strong dependence on the PE number N_p, with height and shape of the dielectric spectrum equally affected.

In Fig. 3.9 c) and d) we plot relaxation time and strength of the LF and HF relaxation process as obtained by simultaneously fitting two Cole-Cole functions to real and imaginary part of the dielectric susceptibility against the scaled monomer concentration c_m/c_m^*. The strength of both LF and HF process decreases with increasing N_p, with decreasing slope. The relaxation time of the LF process increases with increasing N_p before saturation, while the relaxation time of the HF process rests unaffected.

The decrease of the dielectric susceptibility with increasing PE number can be ascribed to the overlap of the counterion atmospheres discussed above. In the literature we find two scenarios: 1) repulsive interactions as apparent in the PE-counterion PMF Fig. 3.8 tend to reduce the fluctuations of the dipole density. This argument is similar to the effect of repulsive interactions among condensed counterions on a single PE in Oosawa's theory [54, 55] which reduce the dielectric susceptibility as compared to Mandel's theory [48] where counterion-counterion interactions are absent. A recently proposed extension of Manning's model to interacting PEs comes to a similar conclusion [62], mutual repulsion of counterions on different PEs lower the susceptibility. 2) the presence of other PEs lowers the potential

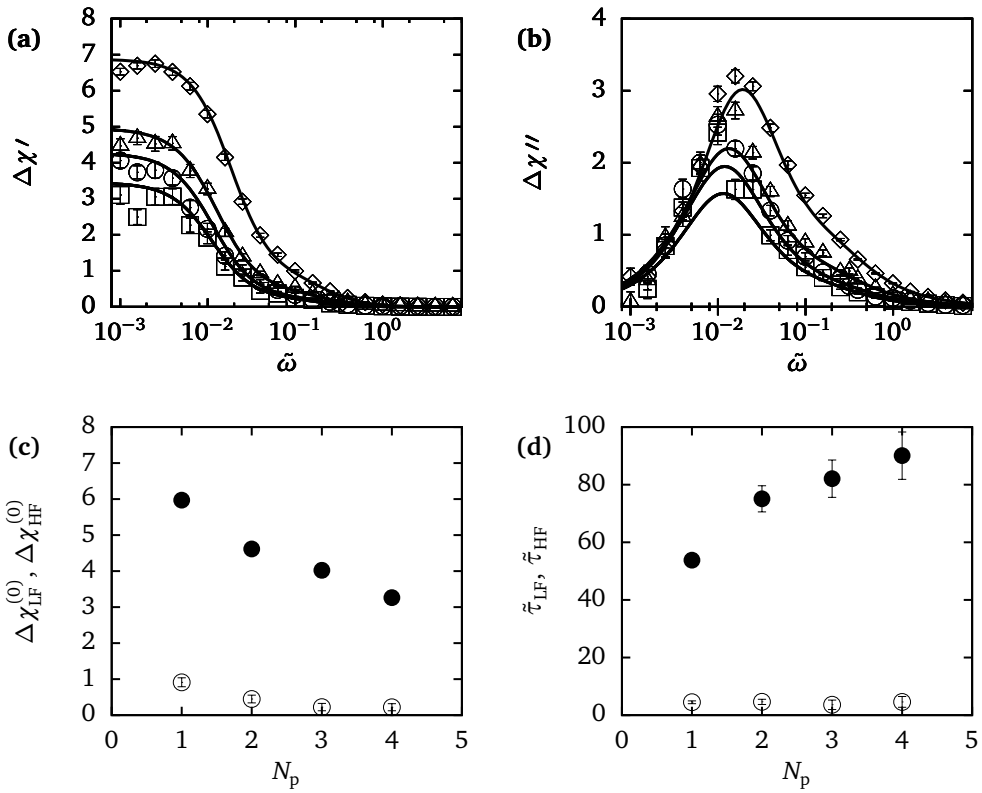

Figure 3.9.: Simulations at fixed monomer number $N_{\mathrm{m}} = 16$, fixed scaled monomer concentration $c_{\mathrm{m}}/c^{*}_{\mathrm{m}} = 0.10$, and various PE numbers $N_{\mathrm{p}} = 1$ (diamonds), $N_{\mathrm{p}} = 2$ (triangles), $N_{\mathrm{p}} = 3$ (circles) and $N_{\mathrm{p}} = 4$ (squares). (a) Real part of the dielectric susceptibility $\Delta\chi'$ as a function of the radial frequency $\tilde{\omega}$. The solid lines are fitting results of two CC-functions. (b) Imaginary part of the dielectric susceptibility $\Delta\chi''$ of the condensed counterions as a function of the radial frequency $\tilde{\omega}$. (c) Fit parameters. Relaxation strengths of the HF process $\Delta\chi^{(0)}_{\mathrm{HF}}$ (open circles) and LF process $\Delta\chi^{(0)}_{\mathrm{LF}}$ (filled circles). (d) Fit parameters. Relaxation times of the HF process $\tilde{\tau}_{\mathrm{HF}}$ (open circles) and of the LF process $\tilde{\tau}_{\mathrm{LF}}$ (filled circles).

barrier for counterions to overcome in order to move from one PE to the other. Consequently the conductivity increases and the dielectric susceptibility decreases [19].

At this point, a closer look at the contribution to the dielectric susceptibility due to condensed or uncondensed counterions might be helpful in understanding the origin of the variations of the dielectric susceptibility with the PE number. For this purpose in Fig. 3.10 a) and b) we plot the real part $\Delta\chi_{cc}'(\tilde{\omega})$ and imaginary part $\Delta\chi_{cc}''(\tilde{\omega})$ of the dielectric susceptibility due to condensed counterions as a function of the radial frequency of the external electric field. Depending on the PE number N_p in the dielectric spectrum of the condensed counterions a second dispersion develops centered at frequencies lower than the LF relaxation frequency. The strength of this low-low frequency (LLF) process increases with PE number N_p, in contrast to the strength of the HF process which decreases.

Although the data quality is not as good as in the case of simulations of a single PE with its counterion atmosphere we attempt a fit of three Cole-Cole functions to the dielectric spectrum

$$\Delta\chi(\tilde{\omega}) = \frac{\Delta\chi_{LLF}^{(0)}}{1+(i\tilde{\omega}\tilde{\tau}_{LLF})^{\alpha_{LLF}}} + \frac{\Delta\chi_{LF}^{(0)}}{1+(i\tilde{\omega}\tilde{\tau}_{LF})^{\alpha_{LF}}} + \frac{\Delta\chi_{HF}^{(0)}}{1+(i\tilde{\omega}\tilde{\tau}_{HF})^{\alpha_{HF}}}\,. \tag{3.49}$$

(Technically we fit one CC-function to the contribution due to uncondensed counterions, and two CC-functions to the contribution due to condensed counterions.) The fitting results for the LLF, LF, and HF strength and relaxation times are shown in Fig. 3.10. The major part of the decrease of the dielectric susceptibility is in the contribution of the uncondensed counterions, which we expect due to increased electrostatic screening. Surprising is the emergence of a third relaxation process, the LLF process, in the dielectric susceptibility of the condensed counterions. The strength of the LLF process grows in favor of the strength of the HF process. Similar to the fitting results obtained with two Cole-Cole functions, cf. Fig. 3.9, the LF relaxation time increases with PE number, but at somewhat smaller rate. The LLF relaxation time seems to be marginally increasing, whereas the HF relaxation time stays unaffected by the change of PE number.

The observation of a second relaxation process in the low-frequency part of the contribution due to condensed counterions resolves the apparent disagreement of simulations and experiment. The LLF process corresponds to the experimentally observed relaxation of condensed counterions. But in contrast to the interpretation leading to the scaling predictions in Section 3.3, where condensed counterions relax parallel to the PE chain, the LLF process is connected to a collective effect.

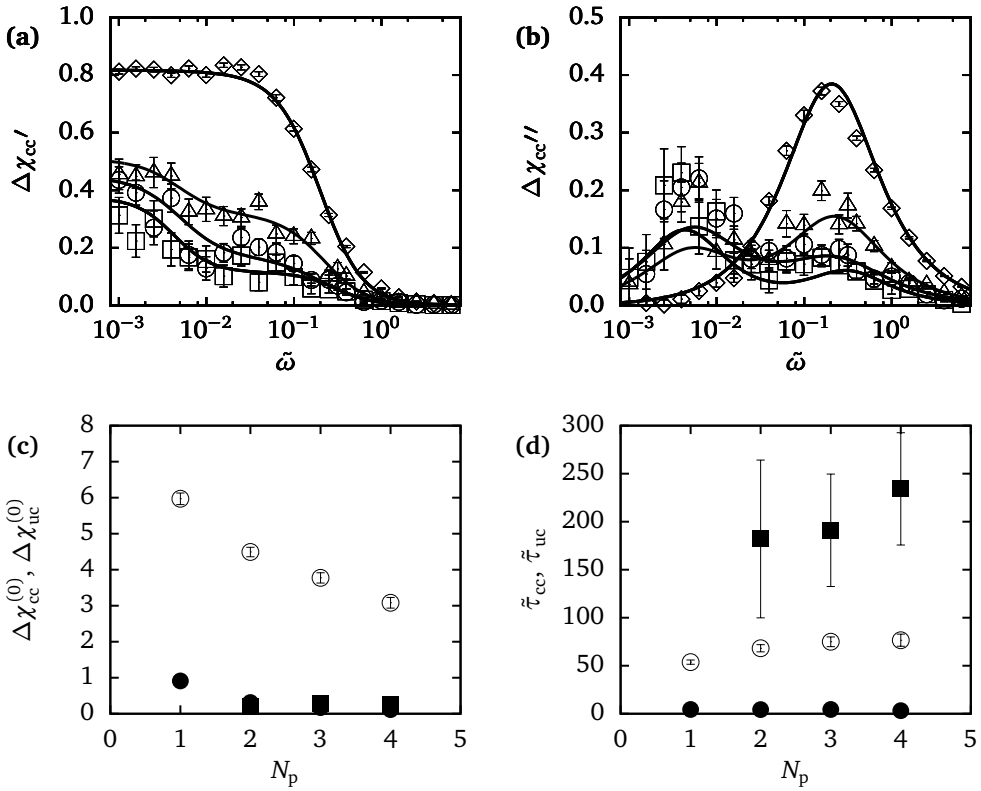

Figure 3.10.: Simulations at fixed monomer number $N_m = 16$, fixed scaled monomer concentration $c_m/c_m^* = 0.10$, and various PE numbers $N_p = 1$ (diamonds), $N_p = 2$ (triangles), $N_p = 3$ (circles) and $N_p = 4$ (squares). Contribution of the condensed counterions. (a) Real part of the dielectric susceptibility $\Delta\chi_{cc}'$ of the condensed counterions as a function of the radial frequency $\tilde{\omega}$. The solid lines are fitting results of two CC-functions. (b) Imaginary part of the dielectric susceptibility $\Delta\chi_{cc}''$ of the condensed counterions as a function of the radial frequency $\tilde{\omega}$. (c) Fit parameters. Relaxation strengths of the uncondensed counterions $\Delta\chi_{uc}^{(0)}$ (open circles) and of the condensed counterions $\Delta\chi_{cc}^{(0)}$ (LLF process - filled squares, HF process - filled circles). (d) Fit parameters. Relaxation times of the uncondensed counterions $\tilde{\tau}_{uc}$ (open circles) and of the condensed counterions $\tilde{\tau}_{cc}$ (LLF process - filled squares, HF process - filled circles).

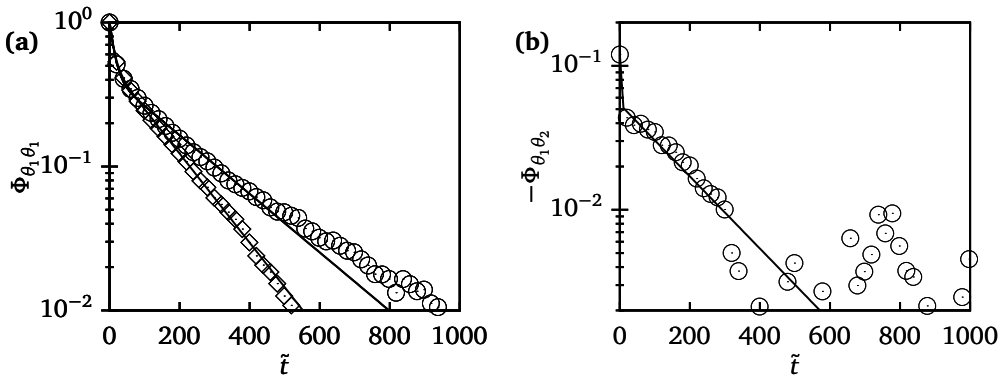

Figure 3.11.: Simulations at monomer number $N_m = 16$ and scaled monomer concentration $c_m/c_m^* = 0.10$. (a) Autocorrelation function $\Phi_{\theta_1\theta_1}(\tilde{t})$ Eq. (3.50) of the fluctuations of the fraction of condensed counterions on a single PE for PE number $N_p = 1$ (diamonds) and $N_p = 2$ (circles). The solid lines are fits of a sum of two exponentials. (b) Crosscorrelation function $\Phi_{\theta_1\theta_2}(\tilde{t})$ Eq. (3.51) of the fluctuations of the fraction of condensed counterions on different PEs for $N_p = 2$ (symbols). The solid lines are fits of a sum of two exponentials.

Evidence for a collective effect

The presence of a second slow relaxation mode in the dielectric response due to condensed counterions also becomes apparent in the autocorrelation function $\Phi_{\theta_1\theta_1}(\tilde{t})$ of the fluctuations of the fraction of condensed counterions θ_1 on a single PE chain

$$\Phi_{\theta_1\theta_1}(\tilde{t}) = \frac{\left\langle \left[\theta_1(\tilde{t}) - \langle\theta_1\rangle\right]\left[\theta_1(0) - \langle\theta_1\rangle\right]\right\rangle}{\left\langle \theta_1 - \langle\theta_1\rangle\right\rangle^2}. \tag{3.50}$$

In Figure 3.11 a) we compare the autocorrelation function $\Phi_{\theta_1\theta_1}(\tilde{t})$ as obtained from simulations with PE number $N_p = 1$ and $N_p = 2$. Both autocorrelation functions feature two distinct relaxation regimes, a fast relaxation regime at short times followed by a slow relaxation regime at long times. In order to get an estimate for the relaxation times we fit a sum of two exponentials to the autocorrelation function $\Phi_{\theta_1\theta_1}(\tilde{t})$. For the relaxation time of the fast process we find $\tilde{\tau}^{\text{fast}}_{\theta_1\theta_1} \approx 12.5$ for PE number $N_p = 1$ and $\tilde{\tau}^{\text{fast}}_{\theta_1\theta_1} \approx 14.3$ for PE number $N_p = 2$, for the relaxation time of the slow process we find $\tilde{\tau}^{\text{slow}}_{\theta_1\theta_1} \approx 140.4$ for PE number $N_p = 1$ and $\tilde{\tau}^{\text{slow}}_{\theta_1\theta_1} \approx 213.5$ for PE number $N_p = 2$. The magnitude of both relaxation processes is approximately the same. In the literature a similar autocorrelation function has been considered for a single PE chain in salt solution, but no explicit discussion of different relaxation processes has been given [96].

That the slow relaxation process might be linked to interactions across multiple PE-counterion complexes can be inferred from the crosscorrelation $\Phi_{\theta_1\theta_2}(\tilde{t})$ between the fluctuations of the fraction of condensed counterions θ_1, θ_2 on different PEs

$$\Phi_{\theta_1\theta_2}(\tilde{t}) = \frac{\left\langle \left[\theta_1(\tilde{t}) - \langle\theta_1\rangle\right] \left[\theta_2(0) - \langle\theta_2\rangle\right] \right\rangle}{\left\langle \theta_1 - \langle\theta_1\rangle \right\rangle \left\langle \theta_2 - \langle\theta_2\rangle \right\rangle}. \tag{3.51}$$

Here $\theta_1(\tilde{t})$ and $\theta_2(\tilde{t})$ denote the fluctuating fraction of condensed counterions on PE 1 and 2, respectively. We find weak anticorrelation, suggesting long-range interactions between different PE-counterion complexes, cf. Fig. 3.11 b). Hence the relaxation of a single PE is intimately linked to the relaxation of other PEs, corresponding to a collective relaxation mode. The relaxation time of the slow relaxation process as obtained from a fit of a sum of two exponentials $\tilde{\tau}^{\text{slow}}_{\theta_1\theta_2} \approx 173$ is close to the relaxation time of the LLF process $\tilde{\tau}_{\text{LLF}} \approx 182$.

In the language of counterion condensation theory, anticorrelation of the fluctuations of the fraction of condensed counterions on different PEs implies different PE effective charges (the effective charge is the PE bare charge neutralized by the condensed counterions), or to put it casually the PE-condensed counterion complexes are “ionized”. In some sense this anticorrelation resembles observations concerning asymmetric counterion condensation on two like-charged colloids [97]. In this context, energy barriers due to correlational energy are thought to stabilize long-lived “ionized states”.

We show, that the slow relaxation process visible in the autocorrelation function $\Phi_{\theta_1\theta_1}(\tilde{t})$ and the crosscorrelation function $\Phi_{\theta_1\theta_2}(\tilde{t})$ underlies the LLF dielectric relaxation process. Evidence is provided by the relaxation time of the slow relaxation process, which has the right order of magnitude as compared to the relaxation time of the LLF relaxation process. However, we cannot explain the presence of a similar slow relaxation process – albeit with somewhat shorter relaxation time – for PE number $N_{\text{p}} = 1$ which has no analogue in the dielectric spectrum.

3.4. Conclusion

While dielectric spectroscopy is a well developed experimental methodology, questions remain open concerning the interpretation of the dielectric response spectra. Using BD simulations of a coarse-grained model of PE solutions, we were able to show that the lowest-frequency relaxation process observed within experiment is due to the relaxation of condensed counterion. Moreover, our results

indicate that this relaxation process is related to a collective effect involving condensed counterions on distant PE chains. This novel relaxation mechanism differs from the classical viewpoint, where no interactions beyond those between a single PE chain and its counterion atmosphere are taken into account, and condensed counterions relax parallel to a PE chain.

4. Electrophoresis beyond the line charge model

The electrophoretic response of PE solutions is determined by the coupling of hydrodynamic and electrostatic interactions giving rise to a rich phenomenology. Size and charge of the PE chains as well as their interactions with the solvent and the ionic environment influence the electrophoretic response of PE solutions enabling numerous applications aiming at electrophoretic separation or electrophoretic enrichment of PE chains.

The exploration of electrophoresis at the beginning of the 20th century arose from the need to separate macromolecules without changing their properties, which is easier said than done. For this, the design of the moving boundary electrophoresis apparatus due to Nobel laureate Arne Tiselius [98] marks the advent of electrophoresis as a separation techniques. The separation of serum proteins according to their charge accomplished by moving boundary electrophoresis impressively demonstrated the power of this method and presented an important step towards the fractionation of blood plasma [98, 99]. Since then electrophoresis became a working horse for the characterization of macromolecules in biology, chemistry, medicine, pharmaceutics, physics and related subjects. Modern electrophoretic methods comprise free-solution capillary zone electrophoresis [100], end-label free-solution electrophoresis where a suitable molecule attached to the macromolecule acts as a drag-tag [101], gel-electrophoresis where cross-linked polymers play the role of a sieving matrix [102], and many more [103]. Needless to say that the industrial impact of electrophoresis is outstanding. Commercial instruments for capillary-array electrophoresis which only recently became available made a decisive contribution to the deciphering of the human genome [11]. In this connection, the ambitious target of a $1000 Genome put forth by the National Human Genome Research Institute is expected to inspire the development of so-called next-generation electrophoresis methods [104].

Free-solution electrophoresis is the simplest experimental set-up to study the fundamental physics of PE electrophoresis. In a nutshell, two things happen when a PE solution is exposed to a static electric

field. First, as the PE chain moves through the solvent, the counterion distribution around the PE chain constantly rebuilds. Since the process of rebuilding the counterion distribution takes a finite amount of time, equilibrium will never be established, the counterion density decreases in front and increases in the wake of the moving PE chain. These small field-induced deviations from the equilibrium counterion distribution effect an internal electric field, the *relaxation field*, which counteracts the external one. As a result, the motion of the PE chain is slowed down. This electrostatic effect goes under the name of *relaxation effect*. The action of the relaxation effect is particularly relevant for strongly charged PEs. Second, the motion of the PE chain and counterions is coupled through long-range hydrodynamic interactions. Under the action of an external electric field the PE chain migrates against the flow field created by oppositely moving counterions. The increased hydrodynamic friction experienced by the PE chain retards its mobility. This hydrodynamic effect is called *retardation effect*.

A large body of literature deals with DNA solutions as a well-characterized model system [105–110]. Frequently used synthetic model systems are solutions of polystyrene sulfonate (PSS) or polyacrylic acid (PAA) [21, 106, 111–113]. A characteristic feature of free-solution electrophoresis is the length-independence of the electrophoretic mobility observed for long PE chains [105–107, 113–115]. This so-called free-draining behavior renders simple free-solution electrophoresis unsuitable for the separation of long PE chains. The free-draining electrophoretic mobility decreases approximately logarithmically with increasing salt concentration [108, 109, 116–118], where the slope of the decrease depends on the nature of counterions and added salt [108–110].

In PE solutions, PE-counterion electrostatic interactions critically depend on the linear charge density $\mathrm{e}\,q_\mathrm{m}/b$ of the PE chains, where q_m denotes the valency of a charged monomer, and b is the charge separation along the PE chain. Above a certain threshold charge density counterions condense on the PE chains and thus to reduce the effective charge density (calculated from the PE charge minus the charge of condensed counterions) to the threshold. This phenomenon is referred to as *counterion condensation* in analogy to the liquid-gas transition. Counterion condensation arises from the subtle balance of electrostatic energy and entropy, expressed through the dimensionless linear charge density or Manning parameter [27]

$$\xi_\mathrm{M} = \frac{|q_\mathrm{ct} q_\mathrm{m}|}{4\pi\epsilon\epsilon_0 \mathrm{k_B} T b}\,. \tag{4.1}$$

Here we denote the counterion valency by q_ct, the relative solvent permittivity by ϵ, the vacuum permittivity by ϵ_0, and the Boltzmann constant by $\mathrm{k_B}$. The Manning parameter Eq. (4.1) governs

the PE-counterion electrostatic interactions, its threshold value is $\xi_M = 1$. For PE chains with linear charge densities above the condensation threshold $\xi_M > 1$ counterion condensation implies that the electrophoretic mobility is expected to be independent of PE charge. Thus counterion condensation can be probed by electrophoresis.

This observation provided the basic motivation for electrophoresis experiments targeting PEs of variable linear charge density. In general, there are two possibilities to change the PE charge. One way to vary the charge of weakly acidic PEs, for instance polyacrylic acid (PAA), consists in changing the solvent pH [116–119]. An advantage of this method is its obvious simplicity and reversibility. The actual distribution of charges on the PE chain eludes control, though. Another method varies the PE charge by copolymerization of charged and uncharged monomers, e.g. acrylic acid and acrylamide [112]. In principle, this methods allows for full control of the charge distribution on the PE chain [20, 120]. In practice charged and uncharged monomers are often polymerized in a random fashion [21, 112, 120–122]. Within a related approach, the PE charge can be modified through chemical reaction such as the sulfonation of polystyrene [113] or *N*-acetylation of chitosan [118]. An elegant method to vary the Manning parameter changes the solvent permittivity. This can be achieved by varying the composition of water/organic cosolvent mixtures [20, 123]. By this method the charge distribution on the PE chain is left untouched at the cost of a modified solvent viscosity. Besides, potential changes of the solvation behavior of PE monomers and counterions have to be accounted for.

In experiment the PE electrophoretic mobility is found to increase with Manning parameter and to level off above the counterion condensation threshold $\xi_M = 1$ [21, 112, 120–122]. But in contrast to expectation a slight increase of the electrophoretic mobility with Manning parameter is observed beyond the threshold. The interpretation of this result relates the increase of the electrophoretic mobility to the discrete nature and compositional heterogeneity of the charge distribution on the PE chains [21, 120]. More recent experiments led to the insight that the PE electrophoretic response is not satisfactorily described by coarse-grained parameters such as the linear charge density [20, 21]. Instead microscopic parameters such as the actual charge distribution on the PE chain might be of importance, which is corroborated by the different electrophoretic mobility of PE chains of different charge density but the same Manning parameter [20] and, more pertinent, by the different electrophoretic mobility of PE chains bearing different charge distributions but the same linear charge density [21].

Yet a systematic connection between parameters of the discrete charge distribution on the PE chains and the electrophoretic mobility has to be established.

Outline

At the current state, mesoscale computer simulations of appropriate PE model systems present a viable tool to push forward our understanding of charge distribution effects in PE electrophoresis. In this respect we intend to go beyond recent publications which focus on the length and field-strength dependence of the electrophoretic mobility of short-chain PEs with homogeneous charge distribution [124, 125].

Using the BD simulation technique, we investigate the electrophoretic response of an infinitely long PE chain and its neutralizing counterions within the framework of the cell model for PE solutions [22]. In order to bring out the consequences of the local charge distribution we consider five PE models which differ in monomer-to-counterion size-ratio and charge separation along the PE chain. We separately determine the electrophoretic response with respect to the external electric field applied either parallel or perpendicular to the PE axis, and calculate the orientationally average as proposed in Refs. [126–128]. Thereby, special emphasis is put on the counterion dynamics. In order to distinguish hydrodynamic from electrostatic effects we study both free-draining dynamics where the hydrodynamic coupling between the particle motion is neglected and non-draining dynamics.

In the linear response limit, that is for weak external electric field, we measure the electrophoretic response as a function of the strength of the PE-counterion electrostatic interactions characterized by the Manning parameter ξ_{M}. Our simulation results satisfactorily show the strong impact of the chain architecture on the ectrophoretic mobility as both monomer-to-counterion size ratio and charge separation reduce the electrophoretic mobility at fixed Manning parameter. As might be expected, the electrophoretic response in parallel field is quite different from the electrophoretic response in perpendicular field. Under free-draining dynamics the parallel electrophoretic mobility is governed by PE model dependent electrofriction between condensed counterions and the corrugated electrostatic potential set up by the charged monomers. In contrast to this the perpendicular mobility is largely determined by counterion condensation, only marginally dependent on the chain architecture, and, to a certain extent, can be modeled by simple renormalization of the monomer charge.

The inclusion of the hydrodynamic coupling between the particle motion within non-draining dynamics dramatically changes the electrophoretic response of both PE chain and counterions. As a result of the hydrodynamic entraining effect the PE electrophoretic mobility is increased as compared to the free-draining case, and already at low Manning parameter differentiated according to monomer-to-counterion size ratio. Qualitatively this can be understood in terms of the hydrodynamic mobility of a cylinder whose length is of the order of the Debye-Hückel screening length. In parallel field condensed counterions may be dragged along by the PE chain moving against the default direction prescribed by the external electric field. Yet we stress that in parallel field the condensed counterions do not move as an entity with the PE chain, as opposed to a common model assumption [129]

In order to study the non-linear response, we fix the Manning parameter to $\xi_{\mathrm{M}} = 4$ and vary the strength of the external electric field. Since for high field strength preferential orientation of the PE chain is to be expected [124] we abstain from performing the orientational average and settle for a discussion of parallel and perpendicular field. The observed increase of the PE electrophoretic mobility corresponds to the Wien effect in simple strong electrolytes [23]. Under free-draining dynamics the electrophoretic mobility saturates for high field strength, the non-linear effect of the chain architecture is wiped out. This is accompanied by stripping off condensed counterions from the PE chain due to the action of the perpendicular external electric field. In contrast, under non-draining dynamics the PE electrophoretic mobility increases without bounds preserving the PE model dependence. In parallel field, due to the high drag experienced by counterions close to the PE chain with increasing field strength condensed counterions tend to move into the bulk. They *evaporate* in order to minimize dissipation.

4.1. A cell model for polyelectrolyte electrophoresis

Below we introduce an adaption of the cell model for PE solutions for the simulation of the electrophoretic response of long extended PE chains. Throughout we use dimensionless parameters following the definitions in chapter 2 and indicated by a tilde.

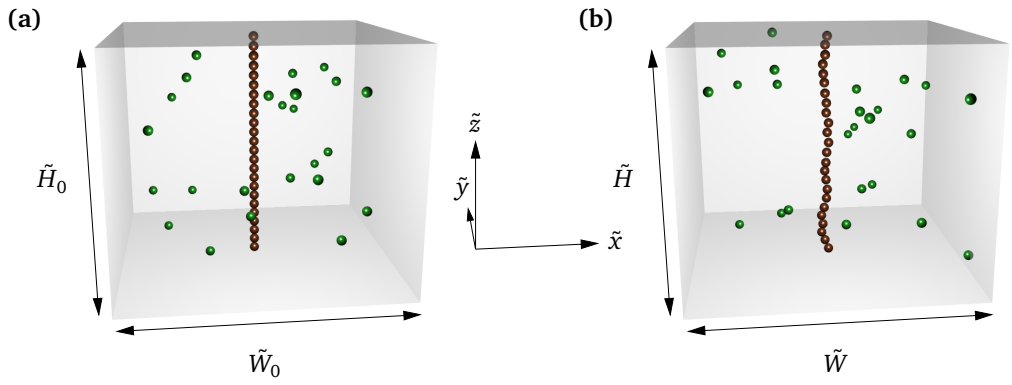

Figure 4.1.: Cell model for a flexible PE chain (red spheres) with neutralizing counterions (green spheres). Periodic boundary conditions apply along the projected end-to-end distance of the PE chain. (a) Initially the chain is fully extended. Cell height and width are given by the contour length $\tilde{H}_0 = 2\tilde{a}_\mathrm{m} N_\mathrm{m}$ and $\tilde{W}_0 = \sqrt{\tilde{V}/\tilde{H}_0}$, respectively. (b) The cell height $\tilde{H}$ which is coupled to the vertical PE extension fluctuates over the course of the simulation. At fixed volume the corresponding cell width is adjusted according to $\tilde{W} = \sqrt{\tilde{V}/\tilde{H}_0}$.

Cell model

We consider a PE chain of N_m monomers of radius $\tilde{a}_\mathrm{m}$ a fraction f of which is charged with charge valency $\tilde{q}_\mathrm{m} = 1$, and N_ct counterions of radius $\tilde{a}_\mathrm{ct}$ with charge valency $\tilde{q}_\mathrm{ct} = -1$, confined in a cubic cell of height $\tilde{H}$ and width $\tilde{W}$. The overall cell is electroneutral,

$$f\,\tilde{q}_\mathrm{m} N_\mathrm{m} + \tilde{q}_\mathrm{ct} N_\mathrm{ct} = 0\,. \tag{4.2}$$

In the spirit of the cell model for PE solutions [22, 130], periodic boundary conditions along the vertical axis are implemented by coupling the cell height $\tilde{H}$ to the vertical PE extension, and replicating the simulation cell infinite times, cf. Fig. 4.1. As a result, height and width are freely fluctuating while the volume $\tilde{V} = \tilde{H} \times \tilde{W}^2$ is fixed. The observed height and width fluctuations are small as compared to the average cell dimensions.

Long-range Coulomb interactions among cell replicas are accounted for through a resummation scheme proposed by Lekner and Sperb [131, 132]. Our implementation closely follows Naji and Netz [28]. Hydrodynamic interactions, if included, are treated on the level of the minimum-image convention [86]. Since under electrophoresis the opposite motion of positively and negatively charged entities entails partial screening of hydrodynamic interactions [133], this truncation presents a mi-

nor shortcoming given sufficiently large cell dimensions. A discussion of related finite-size effects is provided in Appendix A. (Note that in principle, inter-replica hydrodynamic interactions could be included based on Hasimoto's Green's function for the Stokes equation under periodic boundary conditions [134, 135].) Perpendicular to the chain the minimum-image convention applies for all interactions.

Polyelectrolyte models

In order to elucidate the influence of the PE local structure on the electrophoretic response of the cell model we consider five PE models characterized by monomer radius $\tilde{a}_{\mathrm{m}}$ and charge fraction f. Given the distance between adjacent monomers along the PE contour, $2\tilde{a}_{\mathrm{m}}$, the distance between adjacent charged monomers along the PE contour, the charge separation, follows as

$$\tilde{b} = 2\tilde{a}_{\mathrm{m}}/f \,. \tag{4.3}$$

In Figure 4.2 we show simulation snapshots of five PE models: model *A*, a PE chain where every single monomer of radius $\tilde{a}_{\mathrm{m}} = 1$ is charged (charge fraction $f = 1$ and charge separation $b = 2$); model B_1, a PE chain where every second monomer of radius $\tilde{a}_{\mathrm{m}} = 1$ is charged (charge fraction $f = 1/2$ and charge separation $b = 4$); model B_2, a PE chain where every single monomer of radius $\tilde{a}_{\mathrm{m}} = 2$ is charged (charge fraction $f = 1$ and charge separation $b = 4$); model C_1, a PE chain where every third monomer of radius $\tilde{a}_{\mathrm{m}} = 1$ is charged (charge fraction $f = 1/3$ and charge separation $b = 6$); model C_2, a PE chain where every single monomer of radius $\tilde{a}_{\mathrm{m}} = 3$ is charged (charge fraction $f = 1$ and charge separation $b = 6$). These PE models group into two sets. The PE models *A*, B_1, and C_1 share the same monomer radius $\tilde{a}_{\mathrm{m}} = 1$ but have different numbers of interspersed neutral monomers; model *A* has no interspersed neutral monomer per charged monomer, model B_1 has one interspersed neutral monomer, and model C_1 has two interspersed neutral monomers. The PE models *A*, B_2, and C_2 share the same charge fraction $f = 1$ but have different monomer radii; model *A* has monomers of the same size as the counterions, model B_2 has monomers that are twice as large, and model C_2 has monomers that are tree times as large. The counterion radius is fixed at $\tilde{a}_{\mathrm{ct}} = 1$ for all PE models.

The number of charged monomers is fixed at $fN_{\mathrm{m}} = 24$ for all PE models. Accordingly, the initial height of the simulation cell is $\tilde{H}_0 = 48$ for model *A*, $\tilde{H}_0 = 96$ for model B_1 and B_2, and $\tilde{H}_0 = 144$ for

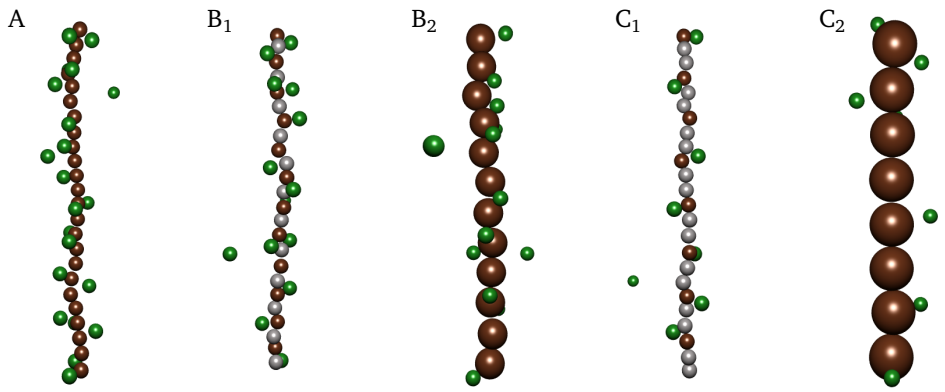

Figure 4.2.: Simulation snapshots of five PE models differing in monomer radius $\tilde{a}_{\mathrm{m}}$ and charge separation $\tilde{b}$ as explained in the main text. Charged monomers are shown in red, neutral monomers in light grey, and counterions in green. Since charged monomers share the same charge $\tilde{q}_{\mathrm{m}}$ irrespective of PE model the Manning parameter ξ_{M} Eq. (4.4) is adjusted via the solvent permittivity. Here the Manning parameter is $\xi_{\mathrm{M}} = 4$.

model C_1 and C_2. The initial width is $\tilde{W}_0 = 56.72$ ensuring equal monomer concentrations over all PE models.

Polyelectrolyte-counterion interactions

In solution, PE-counterion interactions are characterized by the Manning parameter [27]

$$\xi_{\mathrm{M}} = \frac{|q_{\mathrm{ct}} q_{\mathrm{m}}|}{4\pi\epsilon\epsilon_0 \mathrm{k_B} T b}, \tag{4.4}$$

which compares the distance $|q_{\mathrm{ct}} q_{\mathrm{m}}|/4\pi\epsilon\epsilon_0 \mathrm{k_B} T$ beyond which thermal energy exceeds counterion-monomer electrostatic interactions with the charge separation b. For small Manning parameter $\xi_{\mathrm{M}} < 1$ the counterion distribution around the PE chain is diffuse. For large Manning parameter $\xi_{\mathrm{M}} > 1$ the counterion distribution breaks up into two parts: a fraction θ of counterions confined to a small volume in the immediate vicinity of the PE chain and a fraction $1 - \theta$ of counterions diffusely distributed at larger distance from the PE chain. We refer to θ as the fraction of condensed counterions.

Comparability of the electrophoretic response of different PE models requires equal Manning parameter ξ_{M} irrespective of charge separation b. This can be achieved by adjusting the solvent permittivity ϵ, in close analogy to experiments in water/organic cosolvent mixtures of varying composition [20, 123, 136, 137].

Dynamics

Monomers and counterions evolve according to the position Langevin equation Eq. (2.1) introduced in Chapter 2. The dynamics are either free-draining or non-draining neglecting or including the hydrodynamic coupling of the particle dynamics, respectively. In the former case the mobility tensor $\boldsymbol{M}_{ij}(r_{ij})$ is given by Eq. (2.2), in the latter case the Rotne-Prager Yamakawa tensor Eqns. (2.3) and (2.4) is applied. The static external electric field Eq. (2.8) is directed either parallel, $\boldsymbol{E}_{\parallel} = \tilde{E}\hat{\mathbf{e}}_z$, or perpendicular to the PE axis, $\tilde{\boldsymbol{E}}_{\perp} = \tilde{E}\hat{\mathbf{e}}_x$.

4.2. Linear Response

Electrophoresis experiments commonly are performed at low field strength in order to avoid Joule heating of the sample. The electrophoretic response is linear in this regime, *i.e.* the electrophoretic mobility defined below is strictly independent of the field strength. Within BD simulations of the cell model we find a dimensionless field strength of the order of $\tilde{E} = 0.05 - 0.2$ to be sufficiently low to probe the linear response regime. The Manning parameter is varied over two decades, $\xi_{\mathrm{M}} = 0.1 \ldots 10$, including the the counterion condensation threshold $\xi_{\mathrm{M}} = 1$.

4.2.1. Counterion distribution

The counterion distribution around the PE chain is determined by the balance of electrostatic attraction towards and entropic repulsion away from the PE chain, as characterized by the Manning parameter ξ_{M}. The structure of the counterion distribution is crucial for static and dynamic properties of PE solutions. In Figure 4.3 (a) we show the fraction of condensed counterions θ which we define as the fraction of counterions within a distance $\tilde{r}^* = \tilde{a}_{\mathrm{m}} + 4\tilde{a}_{\mathrm{ct}}$ from the center of a monomer. For small Manning parameter $\xi_{\mathrm{M}} < 1$ the counterion distribution is diffuse, there are almost no counterions in the immediate vicinity of the PE chain. At about $\xi_{\mathrm{M}} = 1$ counterion condensation sets in and the fraction of condensed counterions increases with Manning parameter ξ_{M}. Deviations from Manning's limiting law for the fraction of condensed counterions [27]

$$\theta = 1 - \frac{1}{\xi_{\mathrm{M}}} \tag{4.5}$$

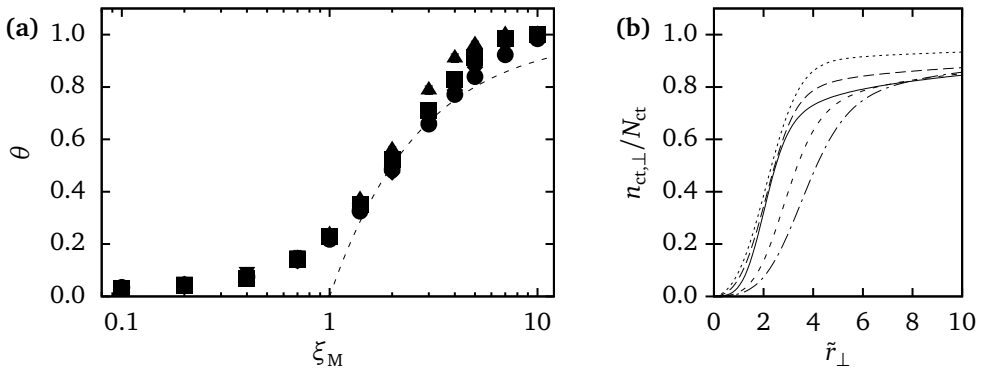

Figure 4.3.: Free-draining simulations under parallel field. (a) Fraction of condensed counterions θ as a function of the Manning parameter ξ_M (model A – circles, model B_1 – squares, model B_2 – diamonds, model C_1 – triangles up, model C_2 – triangles down). The dashed line corresponds to Manning's limiting law Eq. (4.5). (b) Cumulative counterion density $n_{ct,\perp}(\tilde{r}_\perp)$ Eq. (4.6) as a function of lateral distance $\tilde{r}_\perp$ from the PE axis for Manning parameter $\xi_M = 4$ (model A – solid line, model B_1 – long-dashed line, model B_2 – short-dashed line, model C_1 – dotted line, model C_2 – dash-dotted line).

visible in Fig. 4.3 (a) are due to finite cell volume and finite counterion number effects. A thorough discussion of finite size effects can be found in Ref. [18].

The influence of the architecture of a PE model on the fraction of condensed counterions θ becomes apparent at large Manning parameter $\xi_M > 1$ where the fraction of condensed counterions increases with charge separation $\tilde{b}$. This finding is illustrated by the cumulative radial counterion density,

$$n_{ct,\perp}(\tilde{r}_\perp) = 2\pi \int_{-\tilde{H}/2}^{+\tilde{H}/2} \int_0^{\tilde{r}_\perp} d\tilde{r}'_\perp d\tilde{z}' \, \tilde{r}'_\perp \tilde{\rho}_{ct}(\tilde{r}'_\perp, \tilde{z}') . \tag{4.6}$$

Here $\tilde{\rho}_{ct}(\tilde{r}_\perp, \tilde{z}) = \sum_{i=1}^{N_{ct}} \delta(\tilde{r}_\perp - \tilde{r}_{\perp,i})\delta(\tilde{z} - \tilde{z}_i)/2\pi\tilde{r}_\perp$ denotes the counterion density integrated over the polar angle, and $\tilde{r}_\perp$ the radial distance from the PE axis. In Figure 4.3 (b) we show the cumulative radial counterion density $n_{ct,\perp}(\tilde{r}_\perp)$ for Manning parameter $\xi_M = 4$. While the steep increase at short radial distances $\tilde{r}_\perp$ up to a shoulder in the graph attributes to the compact layer of condensed counterions, the shallow gradient at large radial distances is due to the rapidly decaying counterion density in the diffuse counterion atmosphere. For models with the same monomer radius $\tilde{a}_m$ (A, B_1, and C_1) the height of the shoulder increases with increasing charge separation $\tilde{b}$. (Note that the fraction of condensed counterions θ is defined with respect to the distance of a counterion from a monomer and

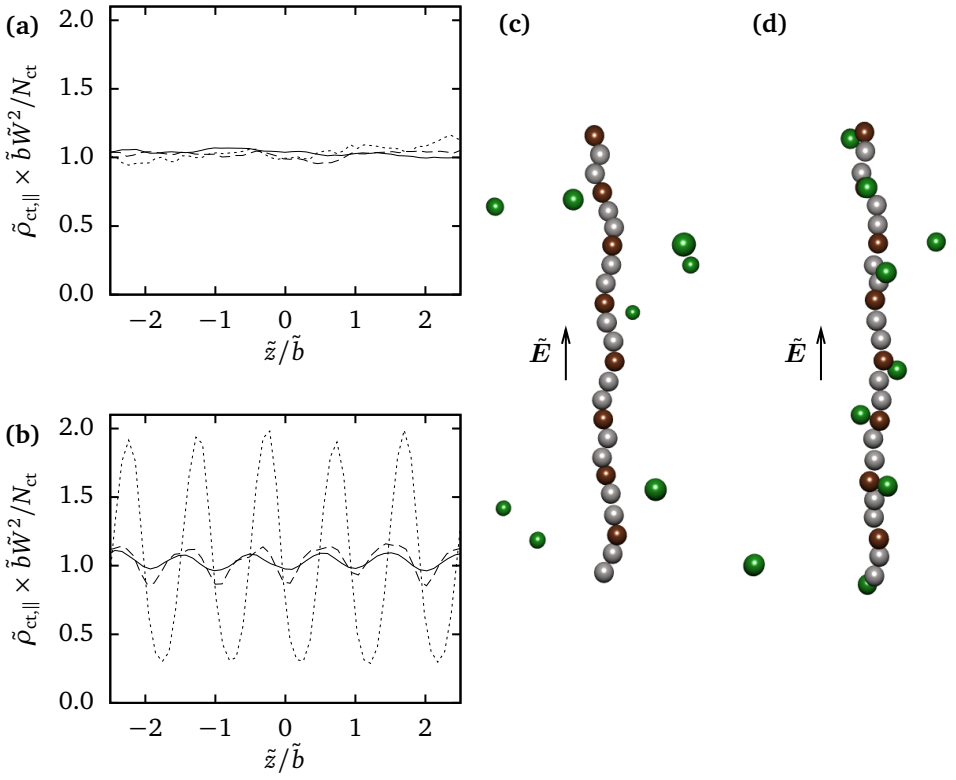

Figure 4.4.: Free-draining simulations under parallel field. Axial counterion density $\tilde{\rho}_{\mathrm{ct},\parallel}$ as a function of the scaled vertical coordinate $\tilde{z}/\tilde{b}$ for Manning parameter (a) $\xi_{\mathrm{M}} = 0.4$ and (b) $\xi_{\mathrm{M}} = 4$ (model A – solid line, model B_1 – long-dashed line, model C_1 – dotted line). (c) Simulation snapshot of model C_1 at Manning parameter $\xi_{\mathrm{M}} = 0.4$. (d) Simulation snapshot of model C_1 at Manning parameter $\xi_{\mathrm{M}} = 4$.

not with respect to the distance from the PE axis. Therefore no one-to-one mapping between the fraction of condensed counterions and the cumulative radial counterion density exists.) An increased counterion density at short distances from discretely charged planes and rods has been found within Monte-Carlo simulations [138, 139] and Poisson-Boltzmann theory [138, 140].

Of similar interest as the cumulative radial counterion density $n_{\mathrm{ct},\perp}(\tilde{r}_\perp)$ Eq. (4.6) is the axial counterion density

$$\tilde{\rho}_{\mathrm{ct},\parallel}(\tilde{z}) = 2\pi \int_0^{+\tilde{W}/\sqrt{2}} \mathrm{d}\tilde{r}'_\perp \, \tilde{r}'_\perp \tilde{\rho}_{\mathrm{ct}}(\tilde{r}'_\perp, \tilde{z}), \tag{4.7}$$

which we plot as a function of the scaled vertical coordinate $\tilde{z}/\tilde{b}$ in Figure 4.4. For small Manning parameter $\xi_{\mathrm{M}} < 1$ the axial counterion density is homogeneous across the scaled vertical coordinate,

cf. Fig. 4.4 (a). Counterions do not localize close to charged monomers (positioned at scaled vertical coordinate $z/b = -2, -1, 0, 1, 2$ in Fig 4.4 (a) and (b)), as supported by simulation snapshot Fig. 4.4 (c). Conversely, for large Manning parameter $\xi_{\mathrm{M}} > 1$ the axial counterion density varies periodically, cf. Fig. 4.4 (b), where the amplitude increases with charge separation $\tilde{b}$. In this cases counterions do localize close to charged monomers, as supported by simulation snapshot Fig. 4.4 (d). Counterion localization has a strong impact on the electrophoretic response under parallel field as will become apparent below.

4.2.2. Free-draining dynamics – electrofriction and relaxation

Two important effects originating from electrostatic interactions in PE solutions can be studied within free-draining simulations, *i.e.* neglecting the hydrodynamic coupling between particle dynamics. The *relaxation effect* in PE electrophoresis describes the development of a counteracting internal electric field, the relaxation field, due to the induced asymmetry of the counterion distribution around the PE chain under the action of the external electric field [141, 142].[1] *Electrofriction* arises when a counterion is driven across an inhomogeneous electrostatic potential [18, 143–145]. In the present case the inhomogeneity of the electrostatic potential is due to the charged PE monomers [18]. The concepts of the relaxation effect and electrofriction are helpful in connection with the interpretation of electrophoresis experiments. They cannot be regarded as independent, though.

Parallel field – electrofriction

Within BD simulations we measure the monomer electrophoretic mobility according to

$$\tilde{\mu}_{\mathrm{m},\parallel} = \frac{\langle \tilde{v}_{\mathrm{m}}(\tilde{t}) \rangle}{\tilde{E}}, \tag{4.8}$$

where $\langle \tilde{v}_{\mathrm{m}}(\tilde{t}) \rangle = \left\langle \sum_{i=1}^{N_{\mathrm{m}}} \tilde{v}_{\mathrm{m},i}(\tilde{t})/N_{\mathrm{m}} \right\rangle$ is the average monomer velocity, and $\langle \cdot \rangle$ denotes an ensemble average. In the limit of vanishing PE-counterion electrostatic interactions, $\xi_{\mathrm{M}} \to 0$, the average monomer velocity is given by the average electric force $f q_{\mathrm{m}} E$ acting on a monomer divided by its Stokes friction

[1] The interested reader may refer to the vivid description of the relaxation effect in Falkenhagen's book [141].

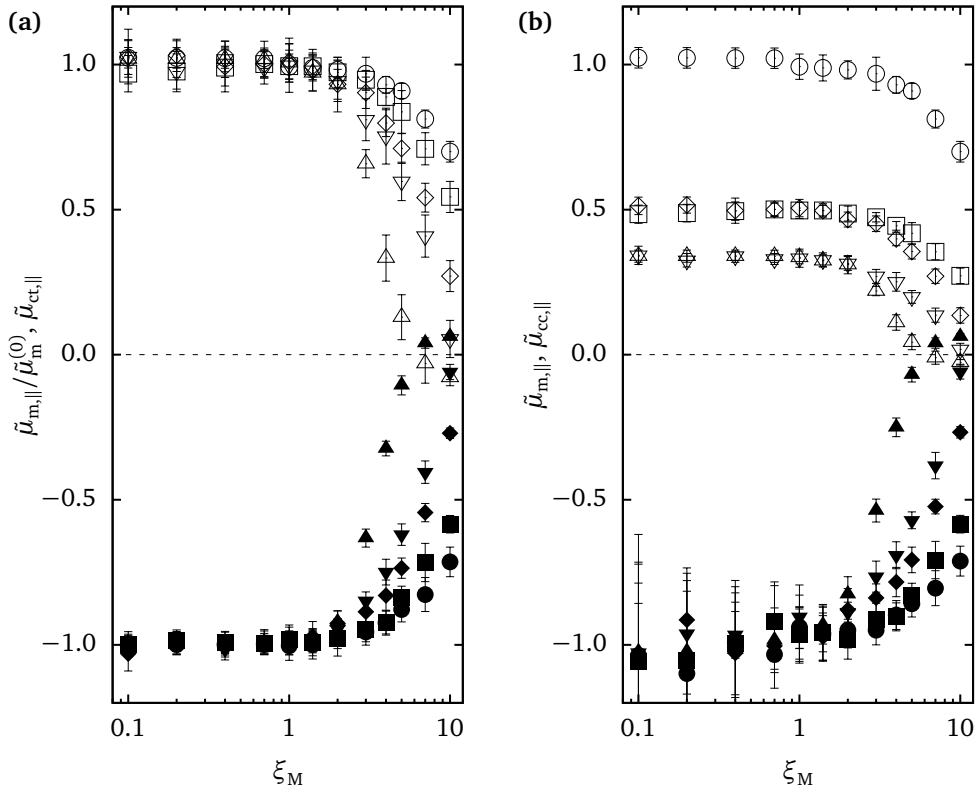

Figure 4.5.: Free-draining simulations under parallel field (model A – circles, model B_1 – squares, model B_2 – diamonds, model C_1 – triangles up, model C_2 – triangles down). (a) Scaled monomer mobility $\tilde{\mu}_{\mathrm{m},\parallel}/\tilde{\mu}_{\mathrm{m}}^{(0)}$ (open symbols) and counterion mobility $\tilde{\mu}_{\mathrm{ct},\parallel}$ (filled symbols) as a function of Manning parameter ξ_{M}. (b) Monomer mobility $\tilde{\mu}_{\mathrm{m},\parallel}$ (open symbols) and condensed counterion mobility $\tilde{\mu}_{\mathrm{cc},\parallel}$ (filled symbols) as a function of Manning parameter ξ_{M}.

coefficient $6\pi\eta a_{\mathrm{m}}$, in dimensionless units $\left\langle \tilde{v}_{\mathrm{m}}^{(0)} \right\rangle = f\tilde{q}_{\mathrm{m}}\tilde{E}/\tilde{a}_{\mathrm{m}}$. Consequently the monomer mobility in the limit of vanishing PE-counterion electrostatic interactions is

$$\tilde{\mu}_{\mathrm{m}}^{(0)} = \frac{f\tilde{q}_{\mathrm{m}}}{\tilde{a}_{\mathrm{m}}}. \tag{4.9}$$

In Figure 4.5 (a) we show the scaled monomer mobility $\tilde{\mu}_{\mathrm{m},\parallel}/\tilde{\mu}_{\mathrm{m}}^{(0)}$ as a function of the Manning parameter ξ_{M}. For small Manning parameter $\xi_{\mathrm{m}} < 1$ PE-counterion electrofriction is negligible and the scaled monomer mobility is given by its limiting value $\tilde{\mu}_{\mathrm{m},\parallel}/\tilde{\mu}_{\mathrm{m}}^{(0)} = 1$ regardless of the PE model. For large Manning parameter $\xi_{\mathrm{M}} > 1$ the scaled monomer mobility decreases from its limiting value, where the magnitude of the decrease is model dependent. In case of PE models A, B_1, and C_1 with the same

monomer radius $\tilde{a}_\mathrm{m}$ the scaled monomer mobility $\tilde{\mu}_{\mathrm{m},\parallel}/\tilde{\mu}_\mathrm{m}^{(0)}$ decreases with charge separation $\tilde{b}$. This is due to potential barriers of increasing height a counterion close to the PE chain has to overcome when traveling along the PE chain, cf. the axial counterion density shown in Fig. 4.4 (b). At fixed charge separation $\tilde{b}$ the barrier height decreases with monomer radius $\tilde{a}_\mathrm{m}$ or monomer-counterion distance of closest approach, respectively. Accordingly, the scaled monomer mobility is higher for models B_2 and C_2 as compared to models B_1 and C_1.

Along with the scaled monomer mobility in Fig. 4.5(a) we show the counterion mobility

$$\tilde{\mu}_{\mathrm{ct},\parallel} = \frac{\langle \tilde{v}_\mathrm{ct}(\tilde{t})\rangle}{\tilde{E}}\,, \tag{4.10}$$

where $\langle \tilde{v}_\mathrm{ct}(\tilde{t})\rangle = \left\langle \sum_{i=1}^{N_\mathrm{ct}} \tilde{v}_{\mathrm{ct},i}(\tilde{t})/N_\mathrm{ct}\right\rangle$ is the average counterion velocity. As a rule, counterions move against the external electric field, the counterion mobility is negative, $\tilde{\mu}_{\mathrm{ct},\parallel} < 0$. Neglecting the hydrodynamic coupling between different particles, the counterion mobility approximately equals the negative scaled monomer mobility, $\tilde{\mu}_{\mathrm{ct},\parallel} \approx -\tilde{\mu}_{\mathrm{m},\parallel}/\tilde{\mu}_\mathrm{m}^{(0)}$. In other words, under free-draining dynamics the internal forces balance on average. (Recall that the external forces acting on charged monomers and counterions balance due to the electroneutrality of the cell model.)

In Figure 4.5(b) we show the monomer mobility $\tilde{\mu}_{\mathrm{m},\parallel}$ together with the condensed counterion mobility

$$\tilde{\mu}_{\mathrm{cc},\parallel} = \frac{\langle \tilde{v}_\mathrm{cc}(\tilde{t})\rangle}{\tilde{E}} \tag{4.11}$$

where $\langle \tilde{v}_\mathrm{cc}(\tilde{t})\rangle = \left\langle \sum_{i=1}^{\theta N_\mathrm{ct}} \tilde{v}_{\mathrm{cc},i}(\tilde{t})/\theta N_\mathrm{ct}\right\rangle$ is the average condensed counterion velocity, and θN_ct is the number of condensed counterions. Over the Manning parameter range considered, condensed counterions do not move with the PE chain, $\tilde{\mu}_{\mathrm{cc},\parallel} \neq \tilde{\mu}_{\mathrm{m},\parallel}$, in contrast to the assumption entering Manning's PE electrophoresis theory [129]. PE-counterion electrofriction nearly exclusively takes place in the small volume occupied by condensed counterions, which can be inferred from the almost quantitative coincidence of the condensed counterion mobility and the counterion mobility, $\tilde{\mu}_{\mathrm{cc},\parallel} \approx \tilde{\mu}_{\mathrm{ct},\parallel}$. Further support comes from the uncondensed counterion mobility which is almost unaffected by the presence of the PE chain (data not shown).

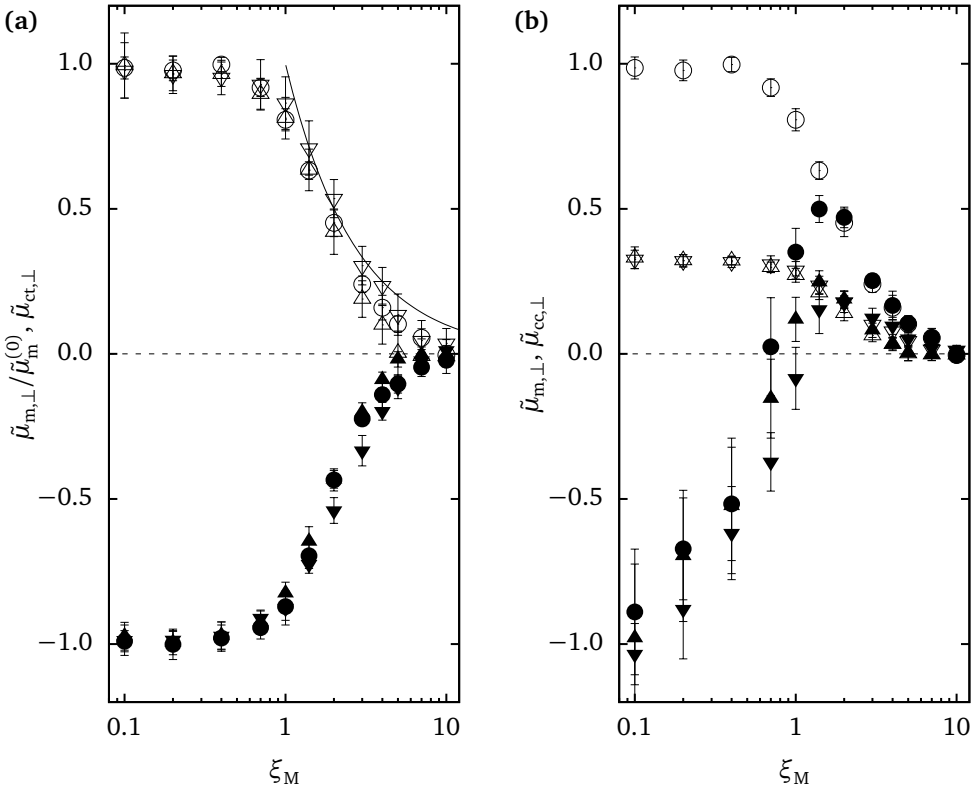

Figure 4.6.: Free-draining simulations under perpendicular field (model A – circles, model C_1 – triangles up, model C_2 – triangles down). (a) Scaled monomer mobility $\tilde{\mu}_{\mathrm{m},\perp}/\tilde{\mu}_{\mathrm{m}}^{(0)}$ (open symbols) and counterion mobility $\tilde{\mu}_{\mathrm{ct},\perp}$ (filled symbols) as a function of Manning parameter ξ_{M}. The solid line is the scaled effective monomer mobility in the limit of vanishing PE-counterion electrostatic interactions $\tilde{\mu}_{\mathrm{m},*}^{(0)}/\tilde{\mu}_{\mathrm{m}}^{(0)}$ Eq. (4.12). (b) Monomer mobility $\tilde{\mu}_{\mathrm{m},\perp}$ (open symbols) and condensed counterion mobility $\tilde{\mu}_{\mathrm{cc},\perp}$ (filled symbols) as a function of Manning parameter ξ_{M}.

Perpendicular field – relaxation and charge renormalization

In Figure 4.6 (a) we show the scaled monomer mobility under perpendicular field $\tilde{\mu}_{\mathrm{m},\perp}/\tilde{\mu}_{\mathrm{m}}^{(0)}$ together with the counterion mobility $\tilde{\mu}_{\mathrm{ct},\perp}$. Starting out from its limiting value $\tilde{\mu}_{\mathrm{m},\perp}/\tilde{\mu}_{\mathrm{m}}^{(0)} = 1$ for small Manning parameter $\xi_{\mathrm{M}} \to 0$ the scaled monomer mobility under perpendicular field decreases gradually for intermediate Manning parameter $0.7 \leq \xi_{\mathrm{M}} \leq 1$ and strongly for large Manning parameter $\xi_{\mathrm{M}} > 1$. The scaled monomer mobility shows very little PE model dependence. This is due to variations of the vertically averaged electrostatic potential with charge distance $\tilde{b}$ or monomer radius $\tilde{a}_{\mathrm{m}}$ at short distances from the PE chain, cf. the cumulative counterion density Fig. 4.3 (b), being relatively small as compared to variations of the radially averaged electrostatic potential, cf. the axial counterion density Fig. 4.4 (b). The decrease of the perpendicular scaled monomer mobility $\tilde{\mu}_{\mathrm{m},\perp}/\tilde{\mu}_{\mathrm{m}}^{(0)}$ with Manning parameter is stronger than the decrease of the parallel scaled monomer mobility $\tilde{\mu}_{\mathrm{m},\parallel}/\tilde{\mu}_{\mathrm{m}}^{(0)}$. As under parallel field, a symmetry-relation between counterion mobility and scaled monomer mobility holds under perpendicular field, $\tilde{\mu}_{\mathrm{ct}\perp} \approx -\tilde{\mu}_{\mathrm{m}\perp}/\tilde{\mu}_{\mathrm{m}}^{(0)}$.

A non-monotonic Manning parameter dependence is observed by the perpendicular condensed counterion mobility $\tilde{\mu}_{\mathrm{cc},\perp}$ which we show together with the perpendicular monomer mobility $\tilde{\mu}_{\mathrm{m},\perp}$ in Fig. 4.6 (b). The perpendicular condensed counterion mobility increases from its limiting value $\tilde{\mu}_{\mathrm{cc},\perp} = -1$ and changes sign for Manning parameter $\xi_{\mathrm{M}} \approx 1$. The condensed counterions move in the direction of the PE chain. For large Manning parameter $\xi_{\mathrm{M}} > 1$ the perpendicular condensed counterion mobility assumes the value of the perpendicular monomer mobility, $\tilde{\mu}_{\mathrm{cc},\perp} = \tilde{\mu}_{\mathrm{m},\perp}$ and condensed counterions move as an entity with the PE chain. As a consequence, the perpendicular condensed counterion mobility decreases for large Manning parameter.

Effective charge model

The observed decrease of the scaled monomer mobility for large Manning parameter $\xi_{\mathrm{M}} > 1$ can be qualitatively explained within a simple model, where the decrease of the monomer mobility is ascribed to the reduction of the monomer charge due to counterion condensation. In the expression for the monomer electrophoretic mobility in the limit of vanishing PE-counterion electrostatic interactions Eq. (4.9) we replace the monomer charge $\tilde{q}_{\mathrm{m}}$ by the effective monomer charge $\tilde{q}_{\mathrm{m}}^{*} = (1-\theta)\tilde{q}_{\mathrm{m}}$ – the monomer charge minus the condensed counterion charge per monomer. Upon substitution of the

limiting expression for the fraction of condensed counterions θ Eq. (4.5) we obtain for the effective monomer mobility in the limit of vanishing PE-counterion electrostatic interactions

$$\tilde{\mu}_{\mathrm{m},*}^{(0)} = \frac{f\tilde{q}_{\mathrm{m}}}{\xi_{\mathrm{M}}\tilde{a}_{\mathrm{m}}} \tag{4.12}$$

which obeys an inverse Manning parameter dependence. As compared to simulations, Fig. 4.6 (a), Eq. (4.12) overestimates the monomer mobility which is due to the neglect of PE-counterion electrostatic interactions. A more sophisticated approach due to Manning [129, 146] accounts for the electrostatic interactions between uncondensed counterions and the charge renormalized PE chain, which results in a shift of the monomer mobility to somewhat smaller values.

Summarizing we observe two mechanisms underlying the decrease of the scaled monomer mobility with Manning parameter. The relaxation effect due to uncondensed counterions and charge renormalization due to condensed counterions.

Orientational average

The electrophoretic response of a long PE chain can be calculated from the electrophoretic response of a straight PE segment oriented parallel or perpendicular with respect to the external electric field $\tilde{\boldsymbol{E}}$. In the absence of curvature, inter-chain and end effects, and if orientation effects are negligible (*i.e.* for small field strength), the average monomer electrophoretic mobility $\tilde{\mu}_{\mathrm{m}}$ follows from the parallel and perpendicular mobilities as [126, 127]

$$\tilde{\mu}_{\mathrm{m}} = \frac{1}{3}\left(\tilde{\mu}_{\mathrm{m},\parallel} + 2\tilde{\mu}_{\mathrm{m},\perp}\right) . \tag{4.13}$$

Similar orientational averages follow for the counterion mobility $\tilde{\mu}_{\mathrm{ct}}$ and condensed counterion mobility $\tilde{\mu}_{\mathrm{ct}}$.

In Figure 4.7 we plot the scaled monomer mobility $\tilde{\mu}_{\mathrm{m}}/\tilde{\mu}_{\mathrm{m}}^{(0)}$, the counterion mobility $\tilde{\mu}_{\mathrm{ct}}$, the monomer mobility $\tilde{\mu}_{\mathrm{m}}$ and the condensed counterion mobility $\tilde{\mu}_{\mathrm{cc}}$, averaged over orientations according to Eq. (4.13). The contribution of the perpendicular mobility $\tilde{\mu}_{\mathrm{m},\perp}/\tilde{\mu}_{\mathrm{m}}^{(0)}$ dominates over the contribution of the parallel mobility $\tilde{\mu}_{\mathrm{m},\parallel}/\tilde{\mu}_{\mathrm{m}}^{(0)}$ as a consequence of the orientational average. This entails, that the dependence of the scaled monomer mobility $\tilde{\mu}_{\mathrm{m}}/\tilde{\mu}_{\mathrm{m}}^{(0)}$ on charge separation $\tilde{b}$ and monomer radius

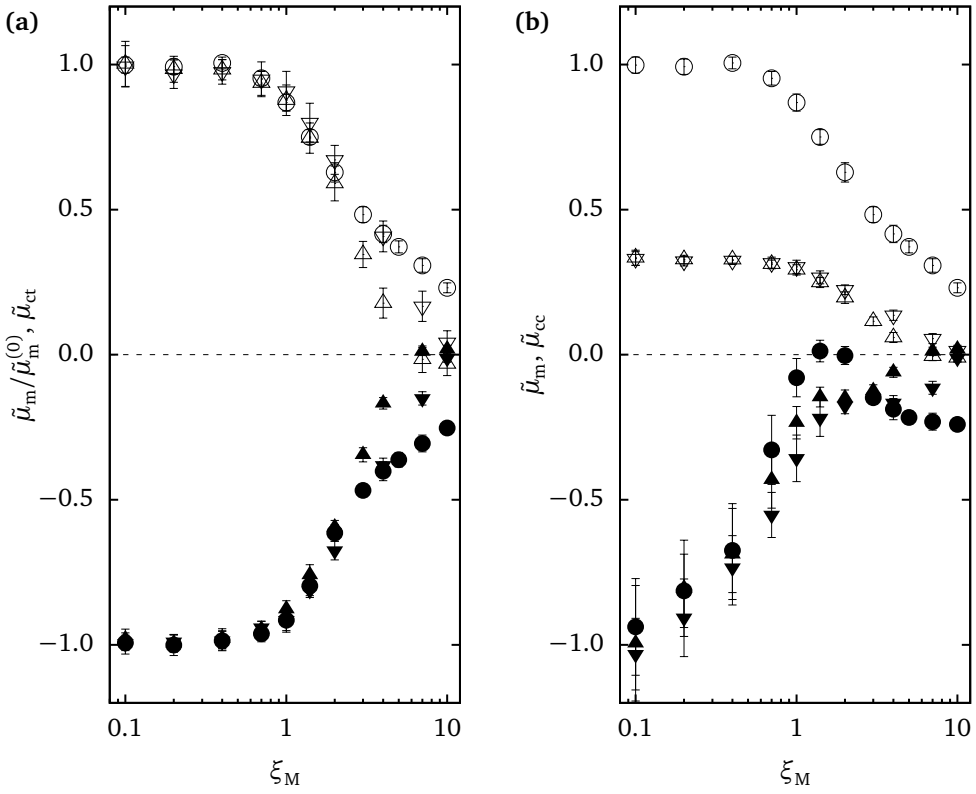

Figure 4.7.: Free-draining simulations. Orientationally averaged mobilities (model A – circles, model C_1 – triangles up, model C_2 – triangles down). (a) Scaled monomer mobility $\tilde{\mu}_m/\tilde{\mu}_m^{(0)}$ (open symbols) and counterion mobility $\tilde{\mu}_{ct}$ (filled symbols) as a function of Manning parameter ξ_M. (b) Monomer mobility $\tilde{\mu}_m$ (open symbols) and condensed counterion mobility and $\tilde{\mu}_{cc}$ (filled symbols) as a function of Manning parameter ξ_M.

$\tilde{a}_m$ is partially wiped out as compared to the parallel scaled monomer mobility $\tilde{\mu}_{m,\parallel}/\tilde{\mu}_m^{(0)}$. Nevertheless the PE model dependence is still present for large Manning parameter $\xi_M > 1$.

Conversely the non-monotonic Manning parameter dependence of the condensed counterion mobility $\tilde{\mu}_{cc}$ is decreased as compared to the perpendicular condensed counterion mobility $\tilde{\mu}_{cc,\perp}$ shown in Fig. 4.6. The condensed counterions do not move as an entity with the PE chain. Trivially, the inverse Manning parameter dependence of the perpendicular scaled monomer mobility $\tilde{\mu}_{m,\perp}/\tilde{\mu}_m^{(0)}$ explained on the basis of the effective monomer charge Eq. (4.12) does not pertain to the orientationally averaged scaled monomer mobility $\tilde{\mu}_m/\tilde{\mu}_m^{(0)}$.

4.2.3. Non-draining dynamics – hydrodynamic friction

Under non-draining dynamics a moving particle exerts a drag force on all other particles. The consequences are twofold. On the one hand, for particles moving in opposite direction the drag force leads to enhanced hydrodynamic friction and retarded particle motion. This entails the *hydrodynamic screening effect* in PE electrophoresis, where long-range hydrodynamic interactions are (partially) screened due to oppositely moving particles. On the other hand, for particles moving in the same direction the drag force leads to reduced hydrodynamic friction and accelerated particle motion. The latter effect is known as the *hydrodynamic entraining effect*.

In order to bring out these two effects we consider the electrophoretic response of the cell model under parallel and perpendicular field using non-draining BD simulations. As for the free-draining case, we consequently calculate and discuss the orientational average.

Parallel field

In Figure 4.8 we show the scaled monomer mobility $\tilde{\mu}_{\mathrm{m},\parallel}/\tilde{\mu}_{\mathrm{m}}^{(0)}$, the counterion mobility $\tilde{\mu}_{\mathrm{c},\parallel}$, the monomer mobility $\tilde{\mu}_{\mathrm{m},\parallel}$, and the condensed counterion mobility $\tilde{\mu}_{\mathrm{cc},\parallel}$. In the limit of vanishing PE-counterion electrostatic interactions $\xi_{\mathrm{M}} \to 0$ the parallel scaled monomer mobility $\tilde{\mu}_{\mathrm{m},\parallel}/\tilde{\mu}_{\mathrm{m}}^{(0)}$ under non-draining dynamics is substantially higher than the parallel scaled monomer mobility under free-draining dynamics, cf. Fig. 4.5 (a). In this limit, the parallel scaled monomer mobility decreases non-linearly with monomer radius $\tilde{a}_{\mathrm{m}}$. Also, we note a weak increase with charge separation $\tilde{b}$. The parallel scaled monomer mobility under non-draining dynamics $\tilde{\mu}_{\mathrm{m},\parallel}/\tilde{\mu}_{\mathrm{m}}^{(0)}$ already decreases for small Manning parameter $\xi_{\mathrm{M}} < 1$, in contrast to the parallel scaled monomer mobility under free-draining dynamics. Similar to the parallel scaled monomer mobility under free-draining dynamics, the parallel scaled monomer mobility under non-draining dynamics shows a strong charge separation dependence for large Manning parameter $\xi_{\mathrm{M}} > 1$. Summarizing the PE model dependence, for small Manning parameter $\xi_{\mathrm{M}} < 1$ the parallel scaled monomer mobility under non-draining dynamics differentiates according to monomer radius $\tilde{a}_{\mathrm{m}}$, whereas for large Manning parameter $\xi_{\mathrm{M}} > 1$ the parallel scaled monomer mobility differentiates according to charge separation $\tilde{b}$.

In the limit of vanishing PE-counterion electrostatic interactions the parallel counterion mobility $\tilde{\mu}_{\mathrm{ct},\parallel}$ under non-draining dynamics assumes the same value as the parallel counterion mobility under free-draining dynamics, cf. Fig. 4.5. However, under non-draining dynamics the parallel counterion

mobility already increases for small Manning parameter $\xi_M < 1$. The increase of the counterion mobility is strongest for model *A* with the smallest monomer radius $\tilde{a}_m$ and weakest for model C_2 with the largest monomer radius, in stark contrast to the counterion mobility under free-draining dynamics. Due to the locally varying solvent velocity induced by the motion of distant counterions and monomers, under non-draining dynamics the approximate equality between the counterion mobility $\tilde{\mu}_{ct,\parallel}$ and the scaled monomer mobility $\tilde{\mu}_{m,\parallel}/\tilde{\mu}_m^{(0)}$ no longer holds.

The parallel condensed counterion mobility $\tilde{\mu}_{cc,\parallel}$ under non-draining dynamics changes dramatically as compared to parallel condensed counterion mobility under free-draining dynamics, cf. Fig. 4.5 (b). In the limit of vanishing PE-counterion electrostatic interactions the parallel counterion mobility $\tilde{\mu}_{cc,\parallel}$ is substantially increased, PE model dependent, and even positive for the PE models with small and intermediate charge separation $\tilde{b}$, namely models *A*, B_1, and B_2! For these models, the hydrodynamic drag force due to the PE chain overcomes the external electric force acting on a condensed counterion. The parallel condensed counterion mobility $\tilde{\mu}_{cc,\parallel}$ is still different from the parallel monomer mobility $\tilde{\mu}_{m,\parallel}$, though. For PE models *A*, B_1, and B_2 the parallel condensed counterion mobility under non-draining dynamics decreases with Manning parameter, as opposed to the parallel condensed counterion mobility under free-draining dynamics. For PE models C_1 and C_2 the parallel condensed counterion mobility increases with Manning parameter after passing through a shallow minimum. This non-monotonic behavior can be understood in terms of a crossover from hydrodynamics dominated PE-counterion interactions for small Manning parameter $\xi_M < 1$ to electrostatics dominated PE-counterion interactions for high Manning parameter $\xi_M > 1$. Within this picture, the shallow minimum for intermediate Manning parameter arises from decreasing hydrodynamic and increasing electrostatic interactions.

Perpendicular field

For perpendicular field, changes of the scaled monomer mobility $\tilde{\mu}_{m,\perp}/\tilde{\mu}_m^{(0)}$ under non-draining dynamics, cf. Fig. 4.9 (a), as compared to the scaled monomer mobility under free-draining dynamics, cf. Fig. 4.7 (a), are similar to the changes observed for parallel field. For small Manning parameter $\xi_M < 1$ the perpendicular scaled monomer mobility under non-draining dynamics is higher than the perpendicular scaled monomer mobility under free-draining dynamics. The increase is not as large as for parallel field, though. For a given Manning parameter, the perpendicular scaled monomer mobility decreases non-linearly with monomer radius $\tilde{a}_m$. The decrease of the scaled monomer mobility $\tilde{\mu}_{m,\perp}/\tilde{\mu}_m^{(0)}$

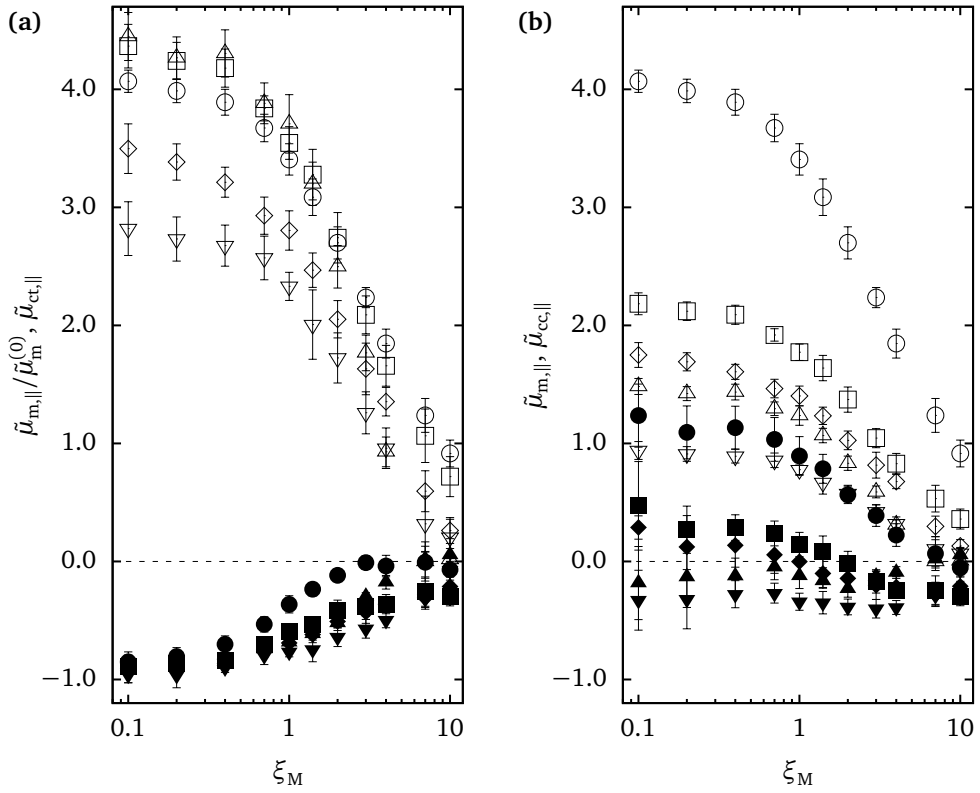

Figure 4.8.: Non-draining simulations under parallel field (model A – circles, model B_1 – squares, model B_2 – diamonds, model C_1 – triangles up, model C_2 – triangles down). (a) Scaled monomer mobility $\tilde{\mu}_m/\tilde{\mu}_m^{(0)}$ (open symbols) and counterion mobility $\tilde{\mu}_{ct}$ (filled symbols) as a function of Manning parameter ξ_M. (b) Monomer mobility mu_m (open symbols) and condensed counterion mobility $\tilde{\mu}_{cc}$ (filled symbols) as a function of Manning parameter ξ_M.

with Manning parameter follows the same characteristics as under free-draining dynamics. The approximate inverse Manning parameter dependence for large Manning parameter $\xi_M > 1$ is preserved, albeit with a prefactor that depends on the monomer radius. The charge separation dependence of the perpendicular scaled monomer mobility is negligibly small.

Similar to the situation for parallel field, PE-counterion hydrodynamic interactions are stronger the smaller the monomer radius $\tilde{a}_{m,\perp}$ and the smaller the charge separation $\tilde{b}$. This becomes apparent in the perpendicular counterion mobility $\tilde{\mu}_{ct,\perp}$ under non-draining dynamics Fig. 4.9 (a) where the perpendicular counterion mobility of model *A* increases more strongly than the perpendicular counterion mobility of model C_1 and model C_2. Further evidence is provided by the perpendicular condensed counterion mobility $\tilde{\mu}_{cc,\perp}$ under non-draining dynamics, cf. Fig. 4.9 (b), where PE-counterion hydrodynamic interactions are strongest for model *A*, resulting in a positive condensed counterion mobility over the Manning parameter range considered. For large Manning parameter $\xi_M > 1$ PE-counterion electrostatic interactions dominate and condensed counterions move as an entity with the PE chain, similar to the perpendicular condensed counterion mobility under free-draining dynamics.

A heuristic model

The effect of hydrodynamic interactions on the monomer mobility can be understood in terms of a simple argument. The opposite motion of negatively charged counterions and positively charged PE chain effects a partial cancellation of the induced flowfields – hydrodynamic interactions are screened over large distances. The length scale associated with the screening of hydrodynamic interactions is given by the Debye-Hückel screening length $\tilde{\kappa}^{-1} = 8\pi\xi_M\tilde{b}|\tilde{q}_{ct}|/|\tilde{q}_m|\tilde{V})^{-1/2}$. (Note that within this definition of the screening length the PE chain does not contribute to the electrostatic screening.) Consequently, the electrophoretic mobility of an infinitely long cylindrical PE chain can be estimated by the mobility of a cylinder of finite length $\tilde{\kappa}^{-1}$. Provided the aspect ratio of the cylinder is large, $1/\tilde{\kappa}\tilde{a}_m \gg 1$ within slender body theory the parallel monomer mobility follows as

$$\tilde{\mu}_{m,\parallel} \approx \frac{3f\tilde{q}_m}{4\tilde{a}_m}\left[2|\ln\left(\tilde{\kappa}\tilde{a}_m\right)| - 1\right], \tag{4.14}$$

and the perpendicular monomer mobility as

$$\tilde{\mu}_{m,\parallel} \approx \frac{3f\tilde{q}_m}{8\tilde{a}_m}\left[2|\ln\left(\tilde{\kappa}\tilde{a}_m\right)| + 1\right], \tag{4.15}$$

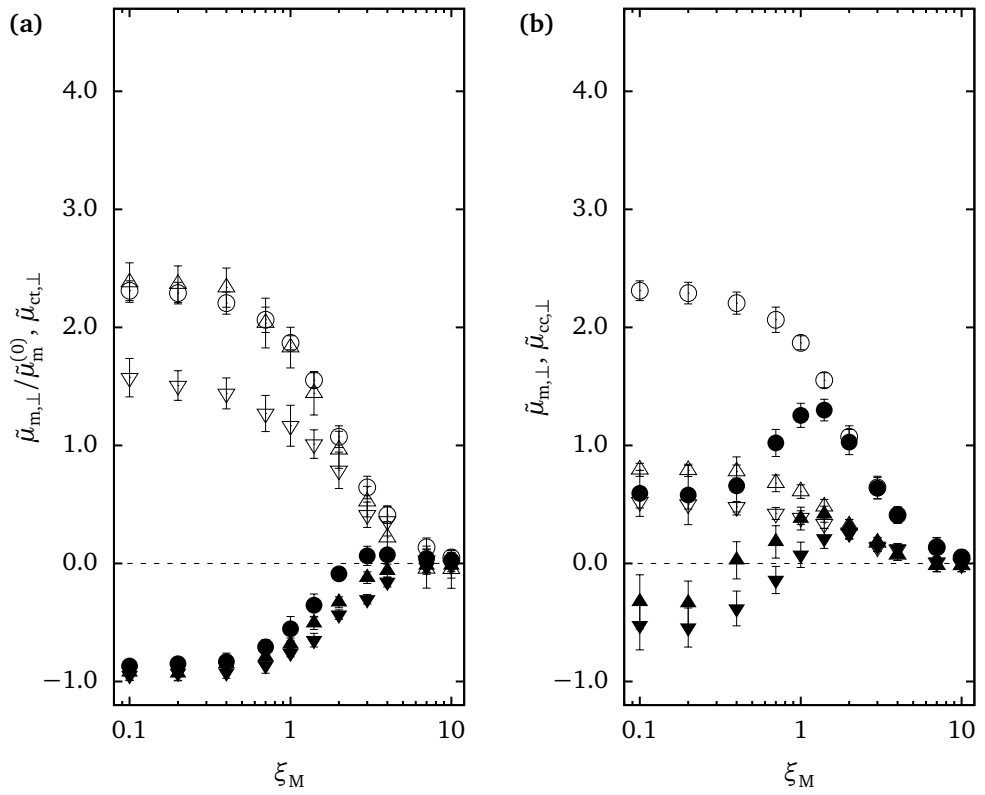

Figure 4.9.: Non-draining simulations under perpendicular field (model A – circles, model C_1 – triangles up, model C_2 – triangles down). (a) Scaled monomer mobility $\tilde{\mu}_m/\tilde{\mu}_m^{(0)}$ (open symbols) and counterion mobility $\tilde{\mu}_{ct}$ (filled symbols) as a function of Manning parameter ξ_M. (b) Monomer mobility $\tilde{\mu}_m$ (open symbols) and condensed counterion mobility and $\tilde{\mu}_{cc}$ (filled symbols) as a function of Manning parameter ξ_M.

where the cylinder radius is $\tilde{a}_m$ and the cylinder line charge density is $f\tilde{q}_m/2\tilde{a}_m$. Through the Debye-Hückel screening length both parallel and perpendicular mobility depend logarithmically on the Manning parameter, $\tilde{\kappa}^{-1} \propto \xi_M^{-1/2}$. The estimates Eq. (4.14) and Eq. (4.15) explain the small Manning parameter characteristics of the parallel and the perpendicular monomer mobility under non-draining dynamics. First, the high monomer mobility $\tilde{\mu}_m/\tilde{\mu}_m^{(0)} > 1$ due to hydrodynamic entrainment. Second, the non-linear monomer radius dependence and the decrease of the monomer mobility with Manning parameter due to hydrodynamic screening. Although for small Manning parameter the estimates give the right order of magnitude for parallel and perpendicular monomer mobility, the comparison should not be pushed too far in view of the crude approximations involved.

Orientational average

From the modeling point of view, the orientational average of parallel and perpendicular mobilities under non-draining dynamics shown in Fig. 4.10 is most relevant, since it presents our closest connection to electrophoresis experiments. At this point it seems appropriate to round up and summarize the insights gained from the analysis of BD simulations for parallel and perpendicular field direction, under free-draining and non-draining dynamics.

Based on the dominant PE-counterion interactions we can distinguish two regimes for the monomer mobility Fig. 4.10 (b): For small Manning parameter $\xi_M < 1$, PE-counterion hydrodynamic interactions are dominant. For a given Manning parameter, the monomer mobility $\tilde{\mu}_m$ increases non-linearly with inverse monomer radius $1/\tilde{a}_m$, and increases with the inverse charge separation $1/\tilde{b}$. For fixed Manning parameter and fixed monomer radius, PE chains with small charge separation move faster than PE chains with large charge separation. For large Manning parameter $\xi_M > 1$ PE-counterion electrostatic interactions are dominant. For a given Manning parameter, the monomer mobility depends non-linearly on both inverse monomer radius $1/\tilde{a}_m$ and inverse charge separation $1/\tilde{b}$.

The condensed counterion mobility $\tilde{\mu}_{cc}$ Fig. 4.10 (b) is strongly affected by the presence of the PE chain. For small Manning parameter $\xi_M < 1$ PE-counterion hydrodynamic interactions drastically increase the condensed counterion mobility. In case of model *A* with the smallest monomer radius and the smallest charge separation the condensed counterion mobility is positive over the Manning parameter range considered. Yet the condensed counterion mobility is always different from the monomer

mobility, even for large Manning parameter $\xi_M > 1$. Condensed counterions do not move as an entity with the PE chain.

Finally we want to comment on a central assumption entering Manning's electrophoresis theory [129]. Within this approach condensed counterions are assumed to move as an entity with the PE chain, as in the simple model introduced above 4.2.2. For perpendicular field, for free-draining as well as non-draining dynamics, it is correct to assume that condensed counterions move as an entity with the PE chain. Conversely, this assumption fails for parallel field, where condensed counterions assume a mobility different from the monomer mobility. Hence assuming that condensed counterions move as an entity with the PE chain for parallel field inevitably leads to an underestimate of the monomer mobility. Our statement is rooted in the cell model for a PE solution as described above. In the case of real systems one could think of other mechanisms immobilizing condensed counterions on the PE chain, such as chemical binding and solvation effects. Further, crumpling of a flexible PE chain on small length scales effects a locally inhomogeneous electrostatic potential in which condensed counterions could be trapped.

4.3. Non-Linear Response

In what follows we discuss the electrophoretic response of the cell model for a PE solution for high field strength $\tilde{E}$. In this case deviations from equilibrium of the counterion distribution function and consequent non-linear effects are to be expected. Here we consider the non-linear response of strongly charged PE models setting the Manning parameter to $\xi_M = 4$ and varying the electric field strengths over two decades according to $0.1 \leq \tilde{E} \leq 10$.

A criterion for the threshold field strength $\tilde{E}^*$ where non-linear field effects become apparent can be obtained by comparing the characteristic time-scales of diffusive and electric field driven transport. The time-scale of diffusive transport is given by $\tau_D = \zeta_{ct}^{(0)} l^2 / k_B T$, the time it takes for a counterion to diffuse over a characteristic distance l. Here $\zeta_{ct}^{(0)}$ denotes the friction coefficient of a counterion. The characteristic time-scale of the field driven transport is given by $\tau_E = l\zeta_{ct}^{(0)} / |\tilde{q}_{ct}\tilde{E}|$, the time it takes for a counterion to travel over a characteristic distance l subject to the external electric field $\tilde{E}$. If the time-scale of field driven transport τ_E falls below the time-scale of diffusive transport τ_D we expect

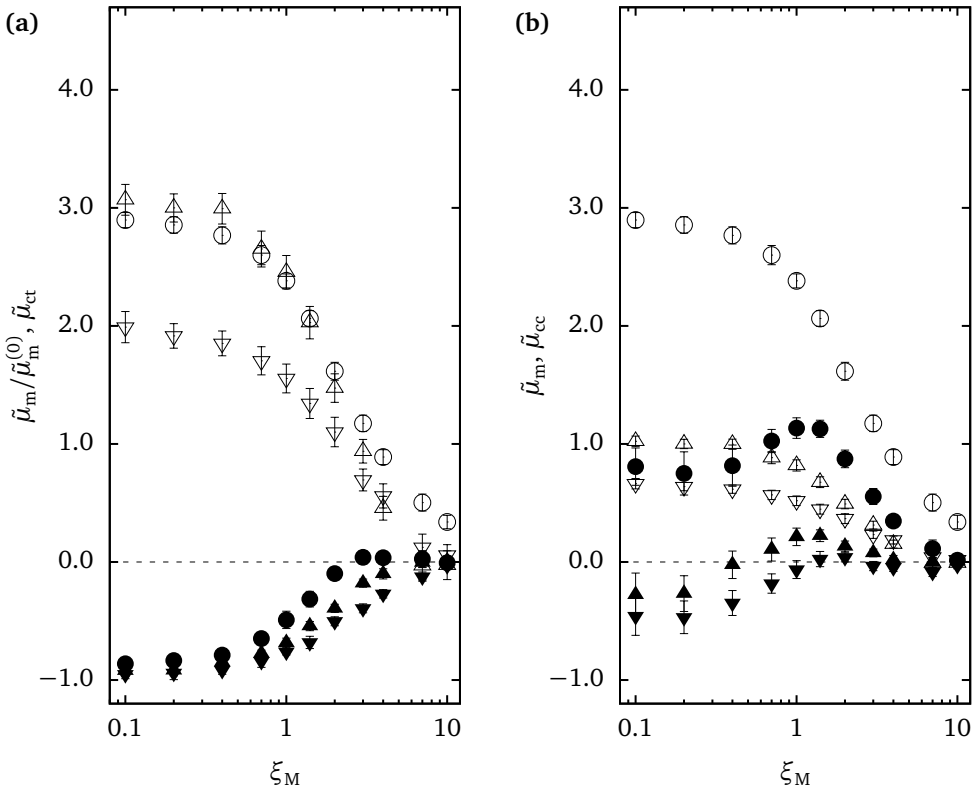

Figure 4.10.: Non-draining simulations. Orientationally averaged mobilities (model A – circles, model C_1 – triangles up, model C_2 – triangles down). (a) Scaled monomer mobility $\tilde{\mu}_m/\tilde{\mu}_m^{(0)}$ (open symbols) and counterion mobility $\tilde{\mu}_{ct}$ (filled symbols) as a function of Manning parameter ξ_M. (b) Monomer mobility $\tilde{\mu}_m$ (open symbols) and condensed counterion mobility and $\tilde{\mu}_{cc}$ (filled symbols) as a function of Manning parameter ξ_M.

non-linear field effects to set in. Equating both time-scales and solving for the threshold field strength $\tilde{E}^*$ yields a simple criterion for the threshold field strength

$$\frac{|\tilde{q}_{\mathrm{ct}}\tilde{E}|}{\mathrm{k_B}T} > \frac{1}{l}\,. \tag{4.16}$$

The characteristic length l is related to the width of the electrostatic potential experienced by the counterions. For parallel field the characteristic length is given by the charge spacing, $l_{\parallel} \sim b$, PE models with large charge separation $\tilde{b}$ are more prone to non-linear effects than PE models with small charge separation. For perpendicular field the characteristic length is given by the Debye-Hückel screening length, $l_{\perp} \sim \kappa^{-1}$, and we expect weakly screened PE solutions to be more prone to non-linear effects than strongly screened PE solutions. Within our simulations the dimensionless screening length is fixed at $\tilde{\kappa}^{-1} = 8$.

Subject to elevetated field strength the isotropy of the PE orientation is not necessarily preserved [124]. As detected within birefringence experiments PE chains commonly tend to orient parallel to the external electric field. However, depending on PE and added salt concentration perpendicular PE orientation is also possible. The latter phenomenon is known to result in an anomalous birefringence signal, which is a subject of vivid debate. Since within our approach we cannot assess the orientational distribution of the PE chain we abstain from calculating the orientationally averaged response and restrict our discussion to parallel and perpendicular PE orientation.

4.3.1. Free-draining dynamics – electrofriction

Parallel field

We perform free-draining BD simulations of PE models A, B_1, C_1, and C_2. The Manning parameter is fixed at $\xi_{\mathrm{M}} = 4$, and the field strength is varied over two decades from $\tilde{E} = 0.1$ to $\tilde{E} = 10$.

That our estimate for the threshold field strength where non-linear effects become important makes sense can be inferred from Fig. 4.11, where we plot scaled monomer mobility $\tilde{\mu}_{\mathrm{m},\parallel}/\tilde{\mu}_{\mathrm{m}}^{(0)}$, counterion mobility $\tilde{\mu}_{\mathrm{ct},\parallel}$, monomer mobility $\tilde{\mu}_{\mathrm{m},\parallel}$, and condensed counterion mobility $\tilde{\mu}_{\mathrm{cc},\parallel}$ as a function of the field strength $\tilde{E}$. The scaled monomer mobility $\tilde{\mu}_{\mathrm{m},\parallel}/\tilde{\mu}_{\mathrm{m}}^{(0)}$ increases with field strength $\tilde{E}$, where the sensitivity of the PE models to the field strength increases with charge separation $\tilde{b}$. For instance, model C_1 with charge separation $b = 6$ already increases at field strengths as low as $\tilde{E} \approx 1/6$. The

increase of the scaled monomer mobility with the field strength is analogous to the Wien effect for simple strong electrolytes [23]. For high field strengths $\tilde{E} > 1$, the scaled monomer mobility converges to its limiting value $\tilde{\mu}_{\mathrm{m},\parallel}/\tilde{\mu}_{\mathrm{m}}^{(0)} \to 1$.

For free-draining dynamics the counterion mobility is approximately equal to the negative scaled monomer mobility, $\tilde{\mu}_{\mathrm{ct},\parallel} \approx -\tilde{\mu}_{\mathrm{m},\parallel}/\tilde{\mu}_{\mathrm{m}}^{(0)}$, for the same reason as discussed in connection with the linear response, cf. Section 4.2. As before, PE-counterion electrofriction is confined to the small volume occupied by condensed counterions, which we conclude from comparison of the parallel counterion mobility $\tilde{\mu}_{\mathrm{ct},\parallel}$ Fig. 4.11 (a) and the parallel condensed counterion mobility $\tilde{\mu}_{\mathrm{ct},\parallel}$ Fig. 4.11 (b).

The explanation of the decreasing PE-counterion electrofriction is simple. The external electric potential tilts and thus effectively flattens the potential barriers a counterion close to the PE chain has to overcome when traveling along the PE chain. This is illustrated in Fig. 4.12 where we show the axial counterion density $n_{\mathrm{ct}}(z)$ Eq. (4.7) as a function of the scaled vertical coordinate z/b for two different field strengths $\tilde{E}$. At low field strength $\tilde{E} = 0.4$ counterions are strongly localized near charged monomers, cf. Fig. 4.12 (a), and electrofriction is high. Conversely, at high field strength $\tilde{E} = 4$ counterion are weakly localized, cf. Fig. 4.12 (b), and electrofriction is low.

We note in passing that the radial counterion density $n_{\mathrm{ct}}(r_\perp)$ Eq. (4.6) as well as the fraction of condensed counterions θ are not significantly affected by the field (data not shown).

Perpendicular field

For perpendicular field the characteristic length scale entering the estimate for the threshold field strength Eq. (4.16) is given by the Debye-Hückel screening length. In the present case $\tilde{\kappa}^{-1} = 8$ and we expect the electrophoretic response to be sensitive to non-linear field effects for field strengths as low as $\tilde{E} = 1/8$. Indeed, the electrophoretic response is non-linear at low field strength $\tilde{E} < 1$, cf. Fig. 4.13 where we plot scaled monomer mobility $\tilde{\mu}_{\mathrm{m},\perp}/\tilde{\mu}_{\mathrm{m}}^{(0)}$, counterion mobility $\tilde{\mu}_{\mathrm{ct},\perp}$, monomer mobility $\tilde{\mu}_{\mathrm{ct},\perp}$, and condensed counterion mobility $\tilde{\mu}_{\mathrm{cc},\perp}$ as a function of the field strength $\tilde{E}$.

Qualitatively the non-linear field dependence of the perpendicular scaled monomer mobility $\tilde{\mu}_{\mathrm{m},\perp}/\tilde{\mu}_{\mathrm{m}}^{(0)}$ and the perpendicular counterion mobility shown in Fig. 4.13 (a) is similar to the parallel scaled monomer mobility and the parallel counterion mobility, cf. Fig. 4.11. Interestingly, the dependence of the perpendicular scaled monomer mobility $\tilde{\mu}_{\mathrm{m},\perp}/\tilde{\mu}_{\mathrm{m}}^{(0)}$ on monomer radius $\tilde{a}_{\mathrm{m}}$ and charge separation $\tilde{b}$ is most pronounced for intermediate field strength.

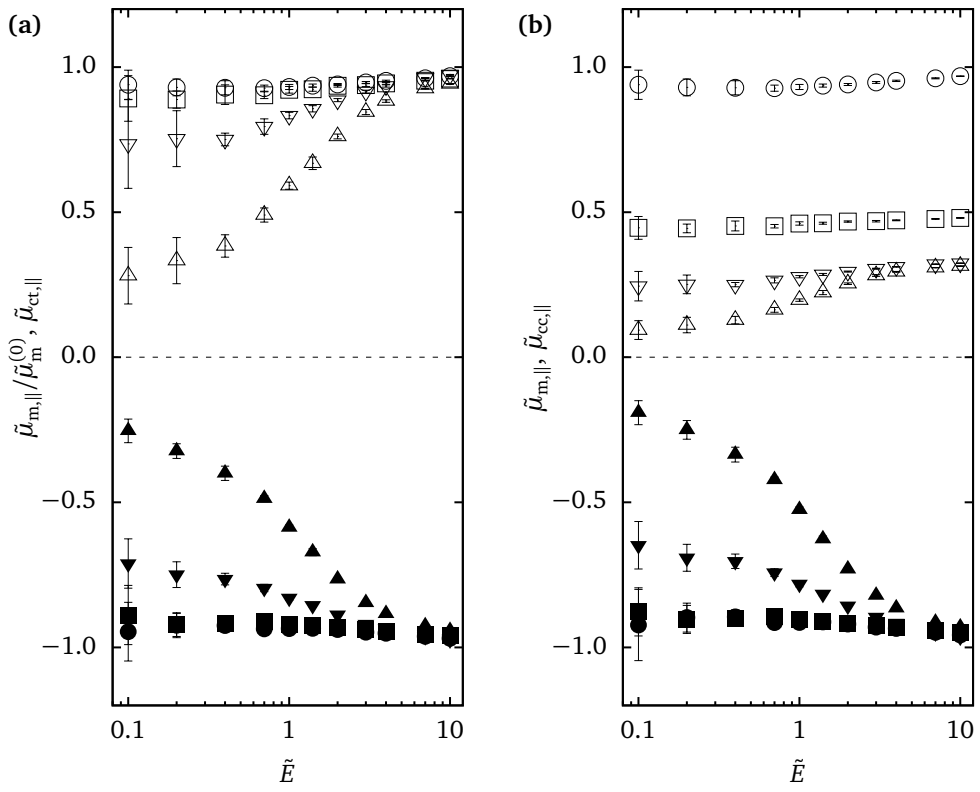

Figure 4.11.: Free-draining simulations under parallel field (model A – circles, model B_1 – squares, model C_1 – triangles up, model C_2 – triangles down). (a) Scaled monomer mobility $\tilde{\mu}_{\mathrm{m},\parallel}/\tilde{\mu}_{\mathrm{m}}^{(0)}$ (open symbols) and counterion mobility $\tilde{\mu}_{\mathrm{ct},\parallel}$ (filled symbols) as a function of field strength $\tilde{E}$. (b) Monomer mobility $\tilde{\mu}_{\mathrm{m},\parallel}$ (open symbols) and condensed counterion mobility $\tilde{\mu}_{\mathrm{cc},\parallel}$ (filled symbols) as a function of field strength $\tilde{E}$.

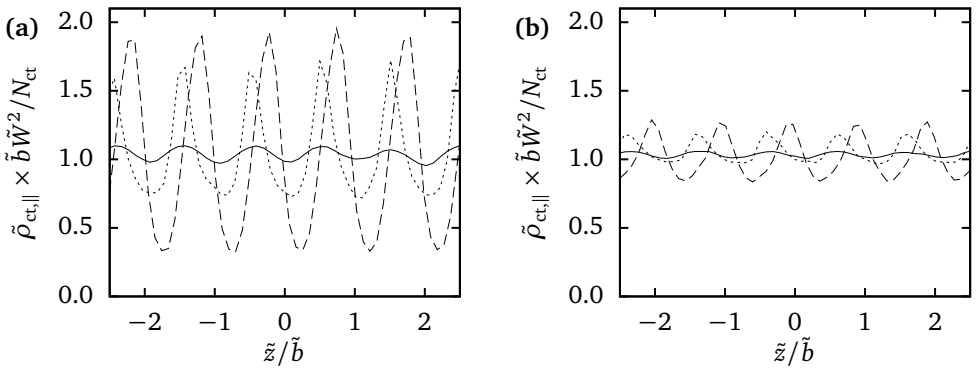

Figure 4.12.: Free-draining simulations under parallel field. Scaled radially integrated counterion density $n_{\mathrm{ct}}(z) \times bW^2$ as a function of the scaled vertical coordinate z/b. (a) At low field strength $\tilde{E} = 0.4$ counterions are strongly localized near charged monomers. (b) At high field strength $\tilde{E} = 4$ counterions are weakly localized.

For low field strength $\tilde{E} < 1$ condensed counterions move as an entity with the PE chain, the perpendicular condensed counterion mobility is positive and approximately equal to the perpendicular monomer mobility, $\tilde{\mu}_{\mathrm{cc},\perp} \approx \tilde{\mu}_{\mathrm{m},\perp}$, cf. Fig. 4.13 (b). For high field strength $\tilde{E} > 1$, the condensed counterion mobility decreases after passing through a maximum, and finally saturates at the free counterion mobility $\tilde{\mu}_{\mathrm{cc},\perp} = -1$.

The field dependence of the perpendicular monomer mobility can be explained by a similar argument as for the parallel monomer mobility. Application of the external electric potential effectively decreases the depth of the PE electrostatic potential such that counterions can escape more easily from the vicinity of the PE chain. In contrast to the parallel field case, this entails that the fraction of condensed counterions θ decreases with the field strength. This behavior is illustrated in Fig. 4.14 where we plot the fraction of condensed counterions θ as a function of the field strength $\tilde{E}$ for model A, C_1, and C_2, along with the cumulative radial counterion density n_{ct} for model A and various field strengths $\tilde{E} = 0.2, 0.4, 0.7, 1.0, 1.4, 2.0$. The fraction of condensed counterions θ decreases with field strength, cf. Fig. 4.14 (a), condensed counterions are stripped off the PE chain. As a consequence, the shoulder in the cumulative radial counterion density n_{ct} flattens with field strength, cf. Fig. 4.14 (b).

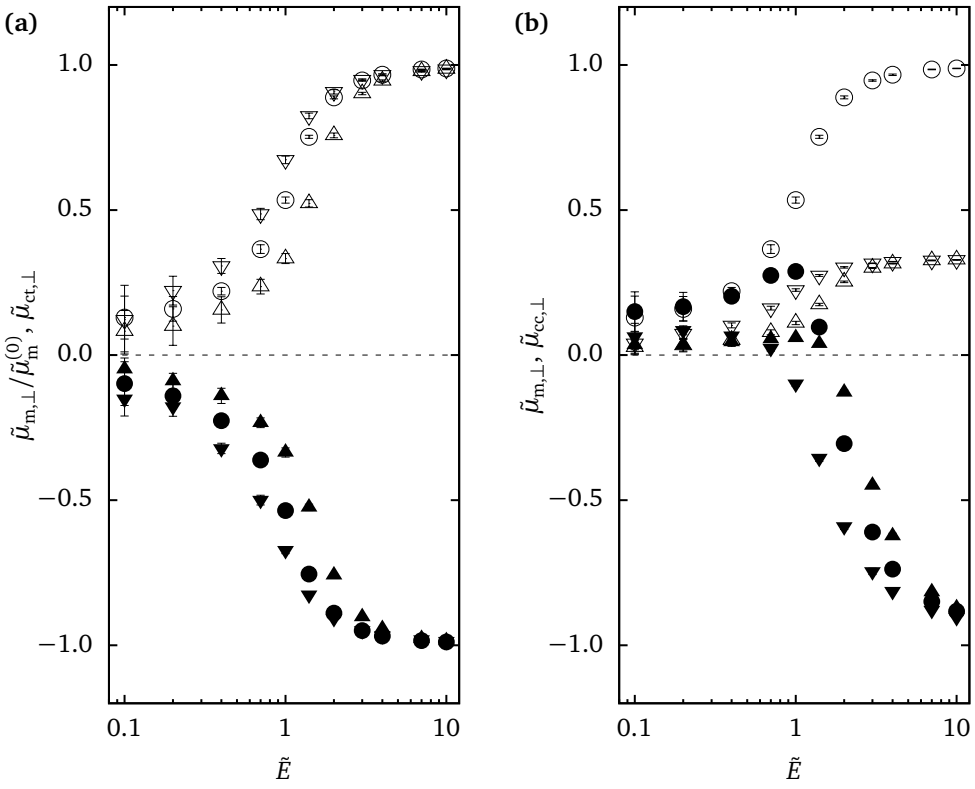

Figure 4.13.: Free-draining simulations under perpendicular field (model A – circles, model C_1 – triangles up, model C_2 – triangles down). (a) Scaled monomer mobility $\tilde{\mu}_{\mathrm{m},\perp}/\tilde{\mu}^{(0)}_{\mathrm{m},\perp}$ (open symbols) and counterion mobility $\tilde{\mu}_{\mathrm{ct},\perp}$ (filled symbols) as a function of field strength $\tilde{E}$. (b) Monomer mobility $\tilde{\mu}_{\mathrm{m},\perp}$ (open symbols) and condensed counterion mobility and $\tilde{\mu}_{\mathrm{cc},\perp}$ (filled symbols) as a function of field strength $\tilde{E}$.

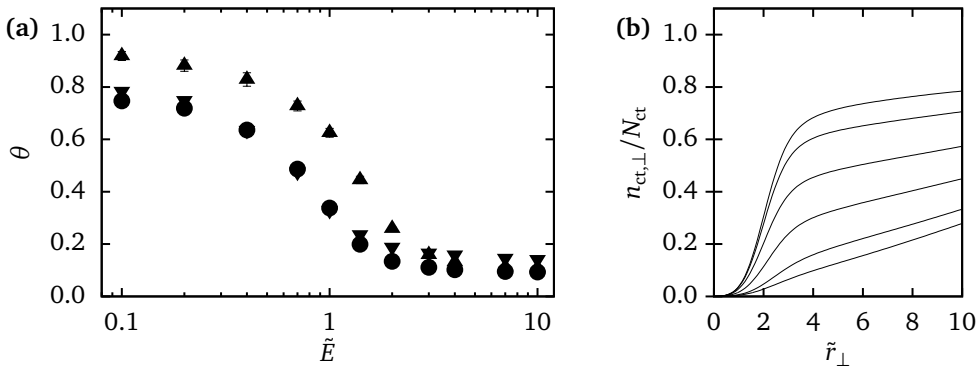

Figure 4.14.: Free-draining simulations under perpendicular field. (a) Fraction of condensed counterions θ as a function of the field strength $\tilde{E}$ (model A – circles, model C_1 – triangles up, model C_2 – triangles down). (b) Cumulative counterion density n_{ct} as a function of the radial distance $r_\perp$ from the polymer for model A. The field strengths are (from top to bottom) $\tilde{E} = 0.2, 0.4, 0.7, 1.0, 1.4, 2.0$.

4.3.2. Non-draining dynamics – hydrodynamic friction

We perform non-draining BD simulations using the mobility tensor as defined in Eq. (2.3) and Eq. (2.4). As before, the Manning parameter is fixed at $\xi_{\mathrm{M}} = 4$, and the field strength is varied in the range $0.1 \leq \tilde{E} \leq 10$.

Parallel field

Scaled monomer mobility, counterion mobility, monomer mobility, and condensed counterion mobility as a function of the strength of the parallel applied field are shown in Fig. 4.15.

The parallel scaled monomer mobility $\tilde{\mu}_{\mathrm{m},\parallel}/\tilde{\mu}_{\mathrm{m}}^{(0)}$ under non-draining dynamics increases with field strength, similar to the free-draining case Fig. 4.11, where the threshold field strength is approximately given by Eq. (4.16) with the characteristic length scale given by the charge separation $\tilde{b}$. But in contrast to the free-draining case, the parallel scaled monomer mobility does not saturate for high field strength $\tilde{E} > 1$ within the parameter range considered. For given monomer radius $\tilde{a}_{\mathrm{m}}$ the slope of the perpendicular scaled monomer mobility increases with charge separation $\tilde{b}$, cf. model A and model C_1. For given charge separation $\tilde{b}$ the slope of the perpendicular scaled monomer mobility decreases with monomer radius $\tilde{a}_{\mathrm{m}}$, cf. model C_1 and model C_2. (Note that the equality of the scaled monomer

mobility of model C_1 and model C_2 with different monomer radius $\tilde{a}_\mathrm{m}$ and same charge separation $\tilde{b}$ is mere coincidence, cf. Fig. 4.8.)

The parallel counterion mobility $\tilde{\mu}_{\mathrm{ct},\parallel}$ under non-draining dynamics decreases with field strength $\tilde{E}$, similar to the free-draining case. Within the parameter range considered no saturation of the parallel counterion mobility is observed.

PE-counterion hydrodynamic interactions are strongest for model *A* with the smallest monomer radius and charge separation, which can be inferred from the parallel condensed counterion mobility $\tilde{\mu}_{\mathrm{cc},\parallel}$ under non-draining dynamics in Fig. 4.15 (b). For model *A* the parallel condensed counterion mobility is positive and increases gradually with field strength, whereas for model C_1 and C_2 the parallel condensed counterion mobility is negative and gradually decreasing.

An important difference as compared to the free-draining parallel field case is the decrease of the fraction of condensed counterions θ with field strength, cf. Fig. 4.16. The hydrodynamic coupling between counterions close to the PE chain causes a weak effective repulsion, condensed counterions evaporate from the PE chain. This effect is also visible in the cumulative radial counterion density n_ct shown for model *A* and various field strengths $\tilde{E} = 0.2, 0.4, 0.7, 1.0, 1.4, 2.0$ in Fig. 4.16 (b). The shoulder in the cumulative radial counterion density decreases with field strength as counterions are repelled from the PE chain.

Perpendicular field

For low to intermediate perpendicular field strength non-draining dynamics yield qualitatively similar results as free-draining dynamics, cf. Fig. 4.17, with the perpendicular scaled monomer mobility $\tilde{\mu}_{\mathrm{m},\perp}/\tilde{\mu}_\mathrm{m}^{(0)}$ increasing already for low field strength. The perpendicular scaled monomer mobility increases strongly with field strength for intermediate field strength and gradually for high field strength. A likewise crossover from strong to gradual decrease can be seen in the perpendicular counterion mobility $\tilde{\mu}_{\mathrm{ct},\perp}$ In contrast to the free-draining case there is no saturation of the perpendicular scaled monomer mobility and the perpendicular counterion mobility within the parameter range considered. In the high field regime, for fixed charge separation $\tilde{b}$ the perpendicular scaled monomer mobility decreases with monomer radius $\tilde{a}_\mathrm{m}$. Apparently the anisotropy of the PE chain plays a minor role at elevated field strength as can be seen by comparing parallel scaled monomer mobility $\tilde{\mu}_{\mathrm{m},\parallel}/\tilde{\mu}_\mathrm{m}^{(0)}$ Fig. 4.15 (a) and perpendicular scaled monomer mobility $\tilde{\mu}_{\mathrm{m},\perp}/\tilde{\mu}_\mathrm{m}^{(0)}$ Fig. 4.17 (a).

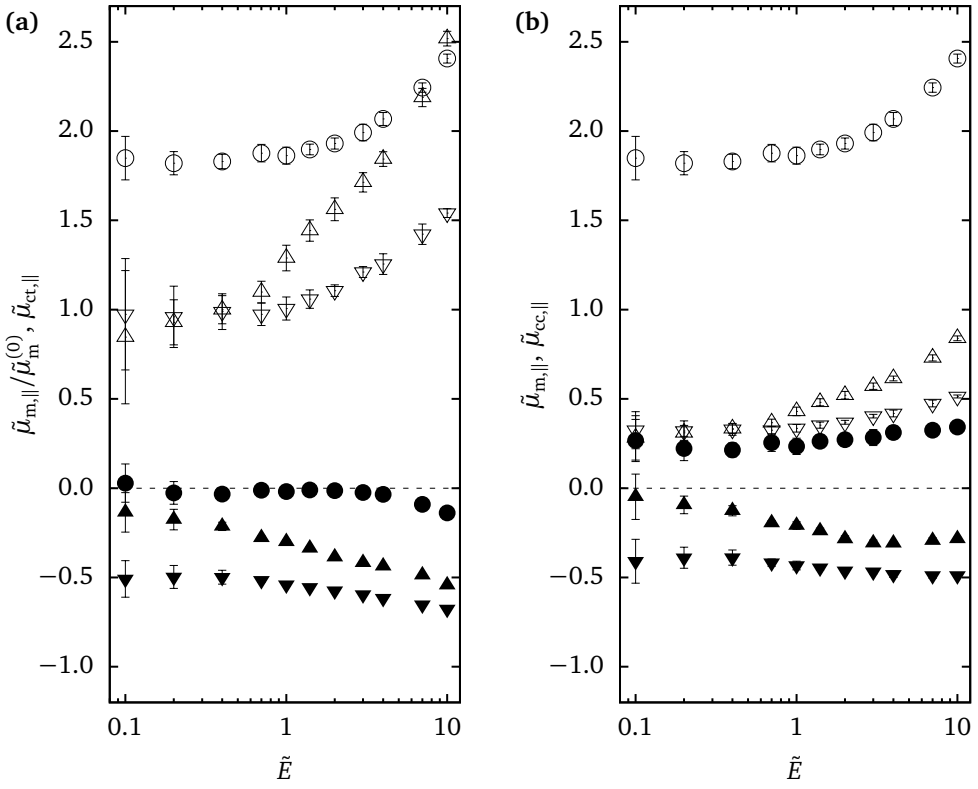

Figure 4.15.: Non-draining simulations under parallel field (model A – circles, model C_1 – triangles up, model C_2 – triangles down). (a) Scaled monomer mobility $\tilde{\mu}_{m,\parallel}/\tilde{\mu}_m^{(0)}$ (open symbols) and counterion mobility $\tilde{\mu}_{ct,\parallel}$ (filled symbols) as a function of field strength $\tilde{E}$. (b) Monomer mobility $\tilde{\mu}_{m,\parallel}$ (open symbols) and condensed counterion mobility and $\tilde{\mu}_{cc,\parallel}$ (filled symbols) as a function of field strength $\tilde{E}$.

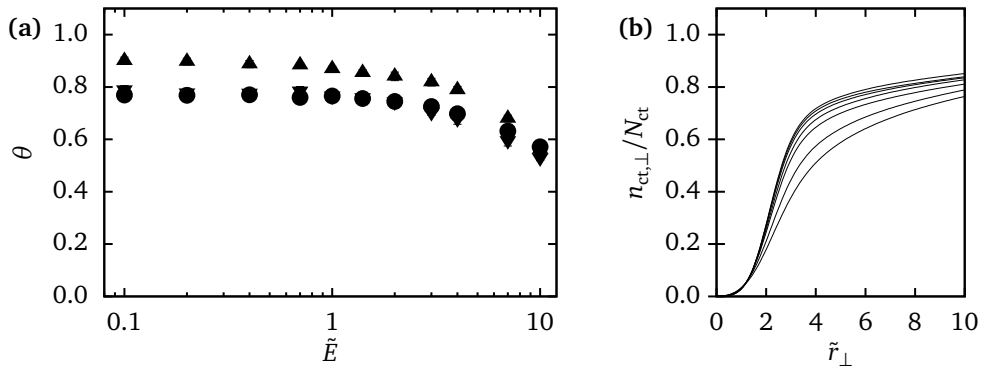

Figure 4.16.: Non-draining simulations under parallel field. (a) Fraction of condensed counterions θ as a function of the field strength $\tilde{E}$. (b) Cumulative counterion density n_{ct} as a function of the radial distance $r_\perp$ from the PE chain for model *A*. The field strengths are (from top to bottom) $\tilde{E} = 1.0, 1.4, 2.0, 3.0, 4.0, 7.0, 10.0$.

Condensed counterions move as an entity with the PE chain for small field strength $\tilde{E} < 1$ and relative to the PE chain for high field strength $\tilde{E} > 1$, cf. Fig. 4.17 (b), as for the free-draining case. Due to strong PE-counterion hydrodynamic interactions for model *A* the perpendicular condensed counterion mobility $\tilde{\mu}_{\mathrm{cc},\perp}$ is positive over the parameter range considered.

Under non-draining dynamics, the fraction of condensed counterions θ (data not shown) agrees nearly quantitatively with that found in the free-draining case, cf. Fig. 4.14, decreasing with field strength $\tilde{E}$. By comparison with Fig. 4.17 (a) we find that the crossover from strong to gradual increase of the perpendicular scaled monomer mobility $\tilde{\mu}_{\mathrm{m},\perp}/\tilde{\mu}_{\mathrm{m}}^{(0)}$ coincides with the saturation of the fraction of condensed counterions θ at around $\tilde{E} \approx 2$.

4.4. Conclusion

The BD simulations of PE chains differing in monomer-to-counterion size ratio and charge separation discussed in this Chapter clearly emphasize the influence of the PE charge architecture on the electrophoretic mobility. This is especially true for strongly charged PEs. Small PE chains with variable charge distribution ranging from random copolymers of charged and uncharged monomers to diblock copolymers present an interesting subject for further investigations.

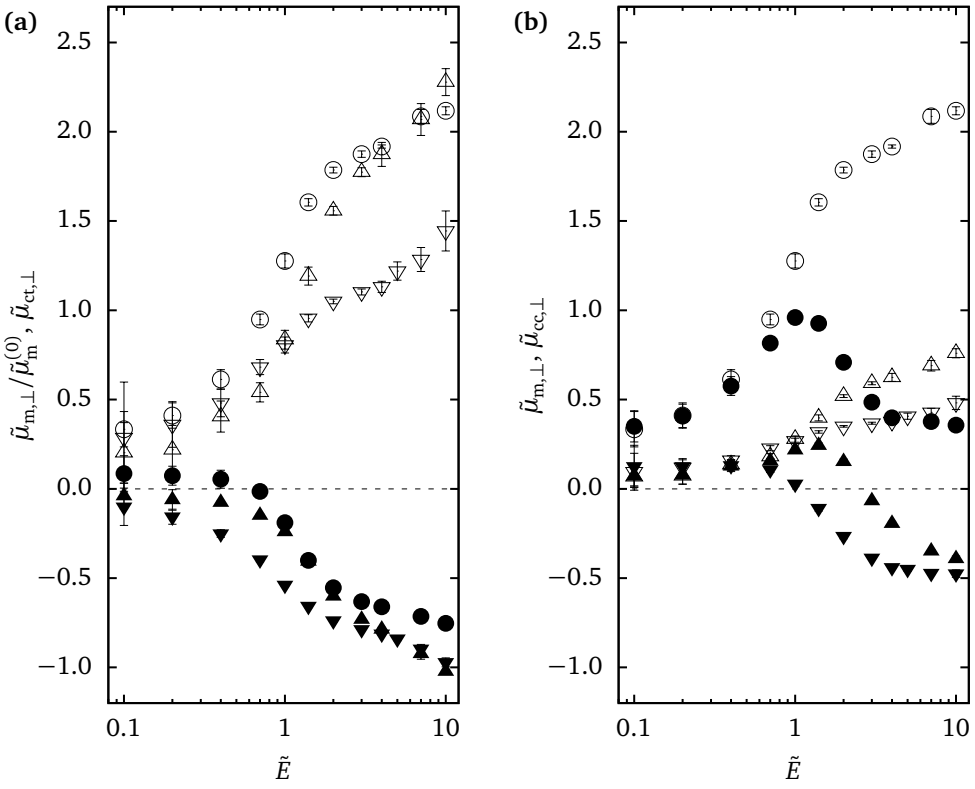

Figure 4.17.: Non-draining simulations under perpendicular field (model A – circles, model C_1 – triangles up, model C_2 – triangles down). (a) Scaled monomer mobility $\tilde{\mu}_{\mathrm{m},\perp}/\tilde{\mu}_{\mathrm{m}}^{(0)}$ (open symbols) and counterion mobility $\tilde{\mu}_{\mathrm{ct},\perp}$ (filled symbols) as a function of the field strength $\tilde{E}$. (b) Monomer mobility $\tilde{\mu}_{\mathrm{m},\perp}$ (open symbols) and condensed counterion mobility and $\tilde{\mu}_{\mathrm{cc},\perp}$ (filled symbols) as a function of field strength $\tilde{E}$.

5. Counterion dynamics at fixed charge distributions

An important method to probe PE-counterion interactions in PE solutions is provided by *tracer diffusion* [147–159], where the counterion mobility is obtained from the spread of radioactively labeled counterions over time. Within tracer diffusion experiments the variation of the counterion mobility with the strength of the PE-counterion electrostatic interactions as characterized by the Manning parameter ξ_M has been of special interest. As elaborated in Chapter 4, the Manning parameter can be varied by changing the linear charge density of the PE chain via solvent pH or copolymerization of charged and uncharged monomers [149, 150, 153, 157, 158, 158].

Experiments agree that for weakly charged PEs or low Manning parameter $\xi_M < 1$ the counterion mobility stays close to the limiting counterion mobility, that is the counterion mobility in the absence of the PE chains and at infinite dilution, independent of Manning parameter. Conversely for strongly charged PEs or high Manning parameter $\xi_M > 1$ the counterion mobility decreases with Manning parameter. More often than not the decrease of the counterion mobility has been observed to scale with the inverse Manning parameter $1/\xi_M$ [148–150, 152, 154–156, 159, 160]. The qualitatively different behavior for low and high Manning parameter has been interpreted as a signature of the counterion condensation transition [27]. From this observation it was only a small step to deduce the fraction of condensed counterions assuming the reduction of the counterion mobility to be exclusively due to counterion condensation [148, 149, 153, 156]. In this connection a vigorous debate emerged over whether or not condensed counterions are free to move along the PE chain.

Theoretical modeling approaches considered the counterion mobility within the framework of the cell-model for PE solutions [22]. This approach places an immobile, rigid PE chain in a periodically replicated cell and calculates the mobility of the neutralizing counterions from the free or driven diffusion of the counterions in the periodic electrostatic potential set up by the PE chain [24, 161–166]. No interactions other than electrostatic interactions are included, *i.e.* the dynamics is assumed to be

free-draining. For counterion diffusion in periodic potentials solution strategies have been worked out in seminal publications by Lifson and Jackson [161] for one dimension, and Jackson and Coriell [24] for arbitrary dimensions. (Also note the instructive derivation of the one dimensional solution in Ref. [167].) Whereas the one dimensional diffusion problem can be solved in closed form [161, 167], diffusion in arbitrary dimensions requires the solution of a complicated boundary value problem. For this case simple expressions for upper and lower bounds of the counterion mobility have been developed, which obtain the counterion mobility from a functional of the equilibrium electrostatic potential [24, 168]. The validity of further simplifications based on linearized electrostatic interactions was restricted to low Manning parameters and hence proved to be of limited applicability [162].

A breakthrough with respect to the calculation of the counterion mobility was accomplished by Manning including nonlinear electrostatics within the framework of the counterion condensation (CC) model [27, 163]. As a crucial assumption of CC theory, the fraction of condensed counterions is assumed to be immobilized on the PE chain. For a line charge representation of the PE chain Manning analytically obtained the counterion mobility averaged over orientations of the PE chain with respect to the external electric field under no-salt and added-salt conditions. For high Manning parameter CC theory reproduces the inverse Manning parameter decrease of the counterion mobility observed in experiment. Because of its favorable agreement with experimental observations, but not least because of its appealing simplicity, Manning's solution was highly embraced by the experimental community. However, on the basis of analytical and numerical solutions for the counterion mobility calculating electrostatic interactions from the non-linear Poisson-Boltzmann (PB) equation [164, 165], Manning was criticized to systematically underestimate the counterion mobility. The origin of this shortcoming is contained in the immobility assumption for condensed counterions; in the absence of interactions other than electrostatic ones condensed counterion move unhindered along the line charge, in contrast to Manning's assumption. While mobile condensed counterion are consistent with the modeling approach, we cannot exclude that in real systems interactions exist such that condensed counterions are indeed trapped on the PE chain. Nevertheless, the scaling of the decrease of the counterion mobility with inverse Manning parameter is confirmed within PB theory, which can be understood as a partial and *a posteriori* justification of Manning's assumption.

Currently neither PB nor the CC approach handles the discrete nature of the charge distribution on PE chains in an appropriate way. While in case of PB theory this shortcoming is due to the lack of

analytical solutions of the PB equation for in homogeneously charged cylinders or linear charge arrays, in the case of CC theory the reason is more fundamental since there inhomogeneities of the charge distribution are treated on the linear level only.

Outline

We start this chapter with a review of the linear response framework for the counterion mobility developed by Jackson and Coriell [24]. Within the scope of this approach upper and lower bounds of the counterion mobility are expressed as a functional of the equilibrium electrostatic potential. We numerically calculate upper and lower bound of the counterion mobility from the PB electrostatic potential of a charged cylinder. Likewise we calculate the counterion mobility at a linear array of charged spheres within CC theory. For comparison we perform free-draining BD simulations of a cell model, cf. Chapter 4, where, in contrast to Chapter 4, the PE chain is immobile and rigid. From simulations of PE models A, C_1 and C_2 defined in Chapter 4 varying in monomer-to-counterion size ratio and charge separation we obtain the counterion mobility in the linear-response limit, as well as the field-dependent counterion mobility.

We show that within both PB and CC theory the general features of the perpendicular counterion mobility at homogeneously charged PE chains can be reproduced. For the parallel counterion mobility the applicability of both approaches is limited. Whereas the PB theory overestimates the parallel counterion mobility at inhomogeneously charged PEs, the CC theory underestimates the counterion mobility at homogeneously charged PEs. In case of the CC theory the immobility assumption for condensed counterions at the PE chain is wrong for homogeneously and weakly inhomogeneously charged cylinders in the absence of other interactions than electrostatic ones.

As a first step towards the inclusion of the effect of an inhomogeneous charge distribution we calculate the counterion mobility from the strong coupling (SC) potential. This approach is promising for counterions at strongly inhomogeneous charge distributions where correlations between counterions and discrete charges on the PE chain become important. For the parallel counterion mobility nice agreement between BD simulations and SC theory is found. In contrast, for the perpendicular counterion mobility the SC approach fails due to an overestimation of correlations between counterions and charged monomers.

We calculate an approximation of the counterion mobility at high field strength which is similar to the upper bound due to Jackson and Coriell. Substitution of the SC potential for the equilibrium potential yields good agreement for the parallel counterion mobility and strongly inhomogeneous potentials, and less good agreement for the perpendicular case.

5.1. The mobility ratio in the linear response limit

In the following we discuss a general solution strategy for the counterion mobility ratio $f_\mu = \mu_{\mathrm{ct}}/\mu_{\mathrm{ct}}^{(0)}$ at an immobile, rigid PE chain, valid in the linear response worked out by Jackson and Coriell [24]. We consider the microscopic counterion current

$$\boldsymbol{j}(\boldsymbol{r}) = -\frac{q_{\mathrm{ct}}\mathrm{k_B}T}{\zeta_{\mathrm{ct}}}\left\{\boldsymbol{\nabla} n_{\mathrm{ct}}(\boldsymbol{r}) + \frac{q_{\mathrm{ct}} n_{\mathrm{ct}}(\boldsymbol{r})}{\mathrm{k_B}T}\boldsymbol{\nabla}\left[\phi(\boldsymbol{r}) - \boldsymbol{r}\cdot\boldsymbol{E}\right]\right\}, \tag{5.1}$$

where $n_{\mathrm{ct}}(\boldsymbol{r})$ denotes the local counterion density. The microscopic counterion current Eq. (5.1) is determined by counterion diffusion against a local concentration gradient $\boldsymbol{\nabla} n_{\mathrm{ct}}(\boldsymbol{r})$ and the electric force $-q_{\mathrm{ct}}\boldsymbol{\nabla}\left[\phi(\boldsymbol{r}) + \boldsymbol{r}\cdot\boldsymbol{E}\right]$ due to the electrostatic potential of the fixed PE charge density $\phi(\boldsymbol{r})$ and the external electric field $\boldsymbol{E}$. In equilibrium, the local counterion density is given by a Boltzmann distribution

$$n_{\mathrm{ct}}^{(0)}(\boldsymbol{r}) = n_{\mathrm{ct},0}\exp\left[-\frac{q_{\mathrm{ct}}\phi^{(0)}(\boldsymbol{r})}{\mathrm{k_B}T}\right], \tag{5.2}$$

where $\phi^{(0)}(\boldsymbol{r})$ is the equilibrium potential, and

$$n_{\mathrm{ct},0} = \frac{1}{V}\int \mathrm{d}^3 r\, n_{\mathrm{ct}}^{(0)}(\boldsymbol{r}) \tag{5.3}$$

is a normalization constant. (Commonly the equilibrium potential is shifted such that $n_{\mathrm{ct},0}$ is the bulk counterion density.)

For small field strength E we can linearize the local counterion density and the electrostatic potential according to

$$n_{\mathrm{ct}}(\boldsymbol{r}) = n_{\mathrm{ct}}^{(0)}(\boldsymbol{r})\left[1 + g_1(\boldsymbol{r})E\right] \tag{5.4}$$

and

$$\phi(\boldsymbol{r}) = \phi^{(0)}(\boldsymbol{r})\left[1 + g_2(\boldsymbol{r})E\right]. \tag{5.5}$$

Here we introduced two auxiliary functions $g_1(\boldsymbol{r})$ and $g_2(\boldsymbol{r})$. Inserting the linearized local counterion density Eq. (5.4) and the linearized electrostatic potential Eq. (5.5) into the microscopic counterion current Eq. (5.1) we obtain to linear order in the field strength

$$\boldsymbol{j}(\boldsymbol{r}) = -\frac{q_{\mathrm{ct}}^2 n_{\mathrm{ct}}^{(0)}(\boldsymbol{r}) E}{\zeta_{\mathrm{ct}}} \left[\boldsymbol{\nabla} g(\boldsymbol{r}) + \hat{\mathbf{n}}_{\boldsymbol{E}}\right] . \tag{5.6}$$

In this context $\hat{\mathbf{n}}_{\boldsymbol{E}} = \boldsymbol{E}/E$ denotes a unit vector in the direction of the external electric field, and the auxiliary function $g(\boldsymbol{r})$ is defined as

$$g(\boldsymbol{r}) = -\frac{\mathrm{k_B}T}{q_{\mathrm{ct}}} \left[g_1(\boldsymbol{r}) + \frac{q_{\mathrm{ct}}}{\mathrm{k_B}T} \phi^{(0)}(\boldsymbol{r}) g_2(\boldsymbol{r}) \right] . \tag{5.7}$$

The macroscopic current in the direction of the external electric field follows from the projected microscopic current $\hat{\mathbf{n}}_{\boldsymbol{E}} \cdot \boldsymbol{j}(\boldsymbol{r})$ averaged over a macroscopic volume according to $J = \int_V \mathrm{d}^3 r\, \hat{\mathbf{n}}_{\boldsymbol{E}} \cdot \boldsymbol{j}(\boldsymbol{r})/V$ which results in

$$J = -\frac{q_{\mathrm{ct}}^2 n_{\mathrm{ct},0} E}{\zeta_{\mathrm{ct}}} \left[1 + \frac{1}{V} \int_V \mathrm{d}^3 r\, \mathrm{e}^{-q_{\mathrm{ct}}\phi^{(0)}(\boldsymbol{r})/\mathrm{k_B}T} \left(\hat{\mathbf{n}}_{\boldsymbol{E}} \cdot \boldsymbol{\nabla}\right) g(\boldsymbol{r}) \right] \tag{5.8}$$

where we applied the normalization condition of the equilibrium counterion density Eq. (5.3). Connection to the mobility ratio can be made by recalling that $J = q_{\mathrm{ct}} n_{\mathrm{ct},0} \langle v_{\mathrm{ct}} \rangle = q_{\mathrm{ct}} n_{\mathrm{ct},0} \mu_{\mathrm{ct}} E$. Hence we find

$$f_\mu = 1 + \frac{1}{V} \int_V \mathrm{d}^3 r\, \mathrm{e}^{-q_{\mathrm{ct}}\phi^{(0)}(\boldsymbol{r})/\mathrm{k_B}T} \left(\hat{\mathbf{n}}_{\boldsymbol{E}} \cdot \boldsymbol{\nabla}\right) g(\boldsymbol{r}) . \tag{5.9}$$

The mobility ratio Eq. (5.9) depends on the equilibrium electrostatic potential through the Boltzmann factor $\exp\left[-q_{\mathrm{ct}}\phi^{(0)}(\boldsymbol{r})/\mathrm{k_B}T\right]$ and the auxiliary function $g(\boldsymbol{r})$. The latter can be determined by taking the divergence of the local current Eq. (5.6), $\boldsymbol{\nabla} \cdot \boldsymbol{j}(\boldsymbol{r}) = 0$, from which it follows that

$$\boldsymbol{\nabla}^2 g(\boldsymbol{r}) - \boldsymbol{\nabla} \frac{q_{\mathrm{ct}}\phi^{(0)}(\boldsymbol{r})}{\mathrm{k_B}T} \cdot \boldsymbol{\nabla} g(\boldsymbol{r}) = \left(\hat{\mathbf{n}}_{\boldsymbol{E}} \cdot \boldsymbol{\nabla}\right) \frac{q_{\mathrm{ct}}\phi^{(0)}(\boldsymbol{r})}{\mathrm{k_B}T} . \tag{5.10}$$

Equation (5.10) is a three-dimensional second order inhomogeneous differential equation which is prohibitively difficult to solve analytically. A viable approximation scheme is derived in the seminal publication of Jackson and Coriell [24]. Accordingly an *upper bound* to the mobility ratio Eq. (5.9)

can be obtained by averaging the equilibrium potential $\phi^{(0)}(\boldsymbol{r})$ over directions perpendicular to the external electric field. Let $\boldsymbol{E} = E\boldsymbol{e}_z$, then the one-dimensional effective potential $\overline{\phi^{(0)}}(z)$ is defined by

$$\mathrm{e}^{-q_{\mathrm{ct}}\overline{\phi^{(0)}}(z)/\mathrm{k_B}T} = \frac{1}{l_x l_y}\int_{l_x}\int_{l_y}\mathrm{d}x\mathrm{d}y\,\mathrm{e}^{-q_{\mathrm{ct}}\phi^{(0)}(\boldsymbol{r})/\mathrm{k_B}T}\,, \tag{5.11}$$

where l_x and l_y denote the dimensions perpendicular to the external electric field. The now one-dimensional Eq. (5.10) can be solved easily leading to the estimate

$$f_\mu^{\mathrm{upp}} = \left[\frac{1}{l_z^2}\int_{l_z}\mathrm{d}z\,\mathrm{e}^{-q_{\mathrm{ct}}\overline{\phi^{(0)}}(z)/\mathrm{k_B}T}\int_{l_z}\mathrm{d}z\,\mathrm{e}^{q_{\mathrm{ct}}\overline{\phi^{(0)}}(z)/\mathrm{k_B}T}\right]^{-1}. \tag{5.12}$$

A *lower bound* to the mobility ratio Eq. (5.9) is given by

$$f_\mu^{\mathrm{low}} = \left[\frac{1}{V^2}\int_V \mathrm{d}^3r\mathrm{e}^{-q_{\mathrm{ct}}\phi^{(0)}(\boldsymbol{r})/\mathrm{k_B}T}\int_V \mathrm{d}^3r\mathrm{e}^{q_{\mathrm{ct}}\phi^{(0)}(\boldsymbol{r})/\mathrm{k_B}T}\right]^{-1}. \tag{5.13}$$

Equations (5.12) and (5.13) are exact bounds for the counterion mobility ratio that follow from a variational calculation [24]. The upper bound Eq. (5.12) depends on the direction of the external electric field, whereas the lower bound Eq. (5.13) does not. Given the equilibrium potential $\phi^{(0)}(\boldsymbol{r})$ both upper bound Eq. (5.12) and lower bound Eq. (5.13) to the mobility ratio can be numerically evaluated at reasonable expenditure.

In what follows we analyze the approximations to the mobility ratio f_μ^{upp} Eq. (5.12) and f_μ^{low} Eq. (5.13) for equilibrium electrostatic potentials from Poisson-Boltzmann (PB) mean field theory [169, 170], counterion condensation (CC) theory [27], and strong-coupling (SC) theory [171, 172]. For this purpose we consider a cell model, where the PE is modeled as a homogeneous or inhomogeneous linear charge density and the external electric field is applied either parallel or perpendicular with respect to the PE main axis. Our special attention will be turned towards the influence of an inhomogeneous charge distribution on the mobility ratio. In the course of this, for both numerical evaluation and graphical representation it will prove useful to introduce a dimensionless equilibrium electrostatic potential $\tilde{\phi}^{(0)}(\tilde{\boldsymbol{r}}) = q_{\mathrm{ct}}\phi^{(0)}(\boldsymbol{r})/\mathrm{k_B}T$ and to rescale all lengths by some characteristic length a according to $\tilde{\boldsymbol{r}} = \boldsymbol{r}/a$. Using dimensionless variables the upper bound then follows as

$$f_\mu^{\mathrm{upp}} = \left[\frac{1}{\tilde{l}_{\tilde{z}}^2}\int_{\tilde{l}_{\tilde{z}}}\mathrm{d}\tilde{z}\,\mathrm{e}^{-\overline{\tilde{\phi}^{(0)}(\tilde{z})}}\int_{\tilde{l}_{\tilde{z}}}\mathrm{d}\tilde{z}\,\mathrm{e}^{\overline{\tilde{\phi}^{(0)}(\tilde{z})}}\right]^{-1}, \tag{5.14}$$

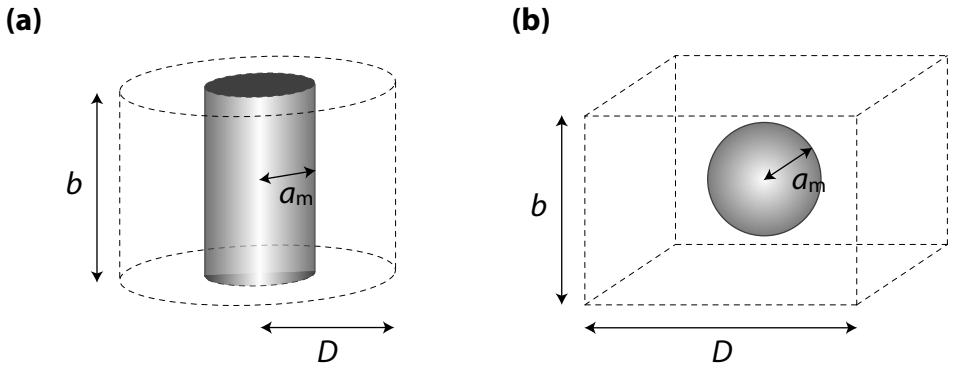

Figure 5.1.: (a) Cell model for a homogeneously charged cylinder. (b) Cell model for a linear array of charged spheres. Periodic boundary conditions apply in the vertical direction.

and the lower bound as

$$f_\mu^{\text{low}} = \left[\frac{1}{\tilde{V}^2} \int_{\tilde{V}} \mathrm{d}^3\tilde{r} \mathrm{e}^{-\tilde{\phi}^{(0)}(\tilde{\boldsymbol{r}})} \int_{\tilde{V}} \mathrm{d}^3\tilde{r} \mathrm{e}^{\tilde{\phi}^{(0)}(\tilde{\boldsymbol{r}})} \right]^{-1} . \tag{5.15}$$

5.2. Cell model for homogeneous or inhomogeneous PE charge density

For the numerical evaluation of Eqns. (5.14) and (5.15) we consider a cell model where the PE is modeled either as a homogeneous or inhomogeneous linear charge density, cf. Fig. 5.1. In the former case, a cylindrical surface charge density $q_\mathrm{m} n_\mathrm{m}(\boldsymbol{r}) = q_\mathrm{m}\delta(r_\perp - a_\mathrm{m})/2\pi b r_\perp$, where $r_\perp$ is the radial distance from the vertical axis and a_m the cylinder radius, centered around the vertical axis and embedded in a cylindrical cell of height b and radius D is chosen. In the latter case a spherical surface charge density $q_\mathrm{m} n_\mathrm{m}(\boldsymbol{r}) = q_\mathrm{m}\delta(r - a_\mathrm{m})/4\pi r^2$, where r denotes the radial distance from the origin of the cell and a_m the sphere radius, embedded in a rectangular cell of height b and width D. In both cases the cell geometry is highly anisotropic, with dimensions D perpendicular to the extension of the PE charge density exceeding the parallel dimension b. The latter defines the line charge density q_m/b of a homogeneous charge density and equals the charge separation b of an inhomogeneous charge density. Periodic boundary conditions apply along the vertical direction.

The external electric field $\boldsymbol{E}$ is applied either parallel or perpendicular to the linear charge density. From the resulting parallel and perpendicular mobility ratio $f_{\mu,\parallel}$ and $f_{\mu,\perp}$, respectively, the orientationally averaged mobility ratio can be obtained according to

$$f_\mu = \frac{1}{3}\left(f_{\mu,\parallel} + 2f_{\mu,\perp}\right) . \tag{5.16}$$

5.3. Comparison with simulations

For comparison we perform free-draining BD simulations of a cell model, cf. Chapter 4, where, in contrast to Chapter 4, the PE chain is immobile and rigid. We calculate the counterion mobility from the counterion electrophoretic response with respect to an external electric field directed parallel or perpendicular to the PE axis. Different PE models are considered, varying in monomer-to-counterion size ratio and charge separation, in order to bring out the effect of the chain architecture on the counterion mobility. For simplicity we reiterate the specification of the three PE models studied here: model *A* is a PE chain where every single monomer of radius $\tilde{a}_\mathrm{m} = 1$ is charged (charge fraction $f = 1$ and charge separation $b = 2$); model C_1 is a PE chain where every third monomer of radius $\tilde{a}_\mathrm{m} = 1$ is charged (charge fraction $f = 1/3$ and charge separation $b = 6$); model C_2 is a PE chain where every single monomer of radius $\tilde{a}_\mathrm{m} = 3$ is charged (charge fraction $f = 1$ and charge separation $b = 6$). Snapshots of the PE models can be found in Fig. 4.2.

5.4. The equilibrium potential within mean-field theory

The mean-field equation for the equilibrium electrostatic potential $\phi^{(0)}(\boldsymbol{r})$ is given by the Poisson-Boltzmann (PB) equation,

$$\boldsymbol{\nabla}^2\phi(\boldsymbol{r}) = -\frac{q_\mathrm{m} n_\mathrm{m}(\boldsymbol{r})}{\epsilon\epsilon_0} - \frac{q_\mathrm{ct} n_{\mathrm{ct},0}}{\epsilon\epsilon_0}\exp\left[\frac{-q_\mathrm{ct}\phi(\boldsymbol{r})}{\mathrm{k_B}T}\right] , \tag{5.17}$$

where the first term accounts for the fixed charge density $n_\mathrm{m}(\boldsymbol{r})$ (charges on the PE chain) and the second term accounts for the counterion density $n_\mathrm{ct}(\boldsymbol{r})$ which obeys the Boltzmann distribution Eq. (5.2). The Poisson-Boltzmann equation Eq. (5.17) is a second order non-linear partial differential equation whose solutions are known in a limited number of cases only [173].

5.4.1. Potential of a homogeneously charged cylinder

In case of an infinitely long homogeneously charged cylinder of radius a_m embedded in a cylindrical cell of radius D, cf. Fig. 5.1 a solution of the Poisson-Boltzmann equation Eq. (5.17) has been worked out by Alfrey *et al.* [169] and Fuoss *et al.* [170]. Depending on the threshold

$$\Lambda = \frac{\ln(D/a_\mathrm{m})}{1+\ln(D/a_\mathrm{m})} \tag{5.18}$$

the equilibrium electrostatic potential takes on different functional forms, namely

$$\frac{q_\mathrm{ct}\phi(\boldsymbol{r})}{\mathrm{k_B}T} = \begin{cases} \ln\left\{\frac{\kappa^2 r_\perp^2}{2\beta^2}\sinh^2\left[\beta\ln\left(\frac{r_\perp}{a_\mathrm{m}}\right)+\operatorname{arccoth}\left(\frac{\xi_\mathrm{M}-1}{\beta}\right)\right]\right\} & \xi_\mathrm{M}\leq\Lambda \\ \ln\left\{\frac{\kappa^2 r_\perp^2}{2\beta^2}\sin^2\left[\beta\ln\left(\frac{r_\perp}{a_\mathrm{m}}\right)+\operatorname{arccot}\left(\frac{\xi_\mathrm{M}-1}{\beta}\right)\right]\right\} & \xi_\mathrm{M}\geq\Lambda\,. \end{cases} \tag{5.19}$$

Here $\kappa^2 = q_\mathrm{ct}^2 n_{\mathrm{ct},0}/\epsilon\epsilon_0\mathrm{k_B}T$ is the Debye-Hückel screening parameter, $r_\perp$ the perpendicular distance from the cylinder axis, and the parameter β follows from the transcendental equation

$$\xi_\mathrm{M} = \begin{cases} \frac{1-\beta^2}{1-\beta\coth\left[-\beta\ln(D/a_\mathrm{m})\right]} & \xi_\mathrm{M}\leq\Lambda \\ \frac{1+\beta^2}{1-\beta\cot\left[-\beta\ln(D/a_\mathrm{m})\right]} & \xi_\mathrm{M}\geq\Lambda\,. \end{cases} \tag{5.20}$$

In Figure 5.2 we plot upper bound $f_{\mu,\perp}^\mathrm{upp}$ Eq. (5.14) and lower bound $f_{\mu,\perp}^\mathrm{low}$ Eq. (5.15) to the perpendicular mobility ratio calculated using the PB potential of a homogeneously charged cylinder Eq. (5.19) as a function of the Manning parameter ξ_M. The cylinder radius is $\tilde{a}_\mathrm{m}=\sqrt{3}$ while the cell radius is fixed at $\tilde{D}=30$. We notice that the difference between upper and lower bound to the mobility ratio is small, *i.e.* the approximations are quite good. The mobility ratio reflects the expected behavior starting out at $f_{\mu,\perp}=1$ for low Manning parameter $\xi_\mathrm{M}\ll 1$, decreasing gently for $\xi_\mathrm{M}\leq 1$ and steeply for $\xi_\mathrm{M}\geq 1$ be for leveling off to $f_{\mu,\perp}=0$ for high Manning parameter $\xi_\mathrm{M}\gg 1$. Increasing the cylinder radius $\tilde{a}_\mathrm{M}$ reduces the slope of the decrease, but only marginally so. Needless to say, for a homogeneously charged cylinder the parallel mobility ratio is $f_{\mu,\parallel}=1$, independent on Manning parameter ξ_M. Comparison of the perpendicular counterion mobility ratio with free-draining BD simulations yields good agreement with model *A* over nearly the entire Manning parameter range. The overestimate of the mobility ratio can partially be ascribed to additional friction due to the repulsive soft-sphere potential applied within simulations. Agreement is less good for model C_1 with larger charge separation b.

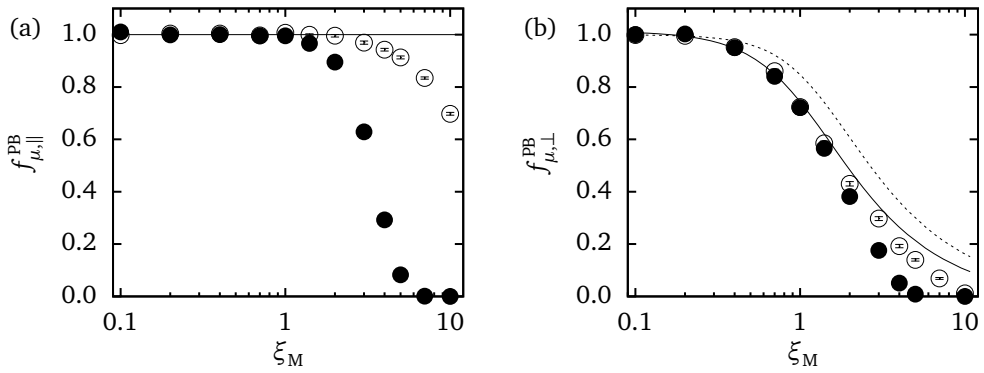

Figure 5.2.: Parallel and perpendicular mobility ratio of counterions at a homogeneously charged cylinder calculated within PB theory as a function of the Manning parameter ξ_M. Lines are numerical solutions of Eqns. (5.14) (upper bound) and (5.15) (lower bound) using the PB potential Eq. (5.19) with cylinder radius $\tilde{a}_m = \sqrt{3}$ and cell radius $\tilde{D} = 30$. Open symbols correspond to simulation results for model *A*, filled symbols to simulations results for model C_1. a) Parallel mobility ratio $f^{PB}_{\mu,\parallel}$. b) Perpendicular mobility ratio $f^{PB}_{\mu,\perp}$.

5.5. The equilibrium potential within counterion condensation theory

Unfortunately, for an inhomogeneously charged cylinder to date no closed-form solution of the PB equation Eq. (5.17) has been published. This is regrettable, since numerical solutions of the PB equation for counterions at an inhomogeneously charged cylinder report enhanced counterion localization at the cylinder surface as compared to solutions of the PB equation for counterions at homogeneously charged cylinders [140], which consequently should decrease both perpendicular and parallel mobility ratio in accord with simulations. In this connection an extension of the perturbative solution procedure introduced by Lukatsky *et al.* [138] for the PB equation of an inhomogeneously charged plane to the PB equation of an inhomogeneously charged cylinder could be promising.

A way out of this dilemma is offered by *counterion condensation theory* [27]. The central idea is that renormalization of the PE charge q_m by the Manning parameter ξ_M allows for the linearization of the PB equation which in turn considerably facilitates solution finding. In so doing, the short-range nonlinear behavior of the PB equation is subsumed in the PE charge renormalization, while the long-range linear behavior is calculated from the linearized PB equation. More detailed, one distinguishes weakly charged PEs characterized by Manning parameter $\xi_M < 1$ and strongly charged PEs characterized by Manning parameter $\xi_M > 1$. For weakly charged PEs the linearized PB equation is solved with the

bare PE charge q_m and the total counterion density $n_{\mathrm{ct},0}$. For strongly charged PEs the linearized PB equation is solved with the effective PE charge $q_\mathrm{m}^* = q_\mathrm{m}/\xi_\mathrm{M}$ – the bare PE charge reduced by the charge of the condensed counterions – and the effective counterion density $n_{\mathrm{ct},0}^* = n_{\mathrm{ct},0}/\xi_\mathrm{M}$ – the density of the UN condensed counterions.

5.5.1. Solution of the linearized Poisson-Boltzmann equation

For weakly charged PEs, *i.e.* for $|q_\mathrm{ct}\phi(\boldsymbol{r})/\mathrm{k_B}T| < 1$, the Boltzmann factor entering the PB equation Eq. (5.17) can be linearized,

$$\boldsymbol{\nabla}^2\phi(\boldsymbol{r}) = -\frac{q_\mathrm{m} n_\mathrm{m}(\boldsymbol{r})}{\epsilon\epsilon_0} - \frac{q_\mathrm{ct} n_{\mathrm{ct},0}}{\epsilon\epsilon_0}\left[1 - \frac{q_\mathrm{ct}\phi(\boldsymbol{r})}{\mathrm{k_B}T}\right]. \tag{5.21}$$

Expanding the electrostatic potential and the fixed charge density in Fourier series according to $\phi(\boldsymbol{r}) = \sum_{\boldsymbol{k}} \phi_{\boldsymbol{k}} \exp(\mathrm{i}\boldsymbol{k}\cdot\boldsymbol{r})$ and $n_\mathrm{m}(\boldsymbol{r}) = \sum_{\boldsymbol{k}} n_{\mathrm{m},\boldsymbol{k}} \exp(\mathrm{i}\boldsymbol{k}\cdot\boldsymbol{r})$, where the summation runs over lattice vectors $\boldsymbol{k} = (2\pi l/W, 2\pi m/W, 2\pi n/b)$ of the rectangular Wigner-Seitz cell, and solving for the electrostatic potential results in

$$\phi_{\boldsymbol{k}} = \frac{q_\mathrm{m}}{\epsilon\epsilon_0}\frac{1}{k^2+\kappa^2} n_{\mathrm{m},\boldsymbol{k}}, \quad k \neq 0. \tag{5.22}$$

Note that we omit a uniform background charge by excluding solutions for wavelength $k = 0$. All that remains is the calculation of the Fourier coefficients of the fixed charge density defined as

$$n_{\mathrm{m},\boldsymbol{k}} = \frac{1}{V}\int_V \mathrm{d}^3 r\, n_\mathrm{m}(\boldsymbol{r}) \exp(-\mathrm{i}\boldsymbol{k}\cdot\boldsymbol{r}). \tag{5.23}$$

We evaluate the fixed charge density within the cell model of a linear charge array considering the charge density of a sphere of radius a_m centered at the origin of the cell

$$n_\mathrm{m}(\boldsymbol{r}) = \frac{\delta\left(r - a_\mathrm{m}\right)}{4\pi r^2}. \tag{5.24}$$

The corresponding Fourier coefficients read

$$n_{\mathrm{m},\boldsymbol{k}} = \frac{1}{V}\frac{\sin(ka_\mathrm{m})}{ka_\mathrm{m}}, \tag{5.25}$$

and the electrostatic potential Eq. (5.22) becomes

$$\frac{q_{\mathrm{ct}}}{\mathrm{k_B}T}\phi_{\boldsymbol{k}} = -\frac{\kappa^2 \sin(ka_{\mathrm{m}})}{ka_{\mathrm{m}}(k^2+\kappa^2)}, \quad k \neq 0\,. \tag{5.26}$$

As a matter of fact we require the electrostatic potential in position space for the calculation of upper bound Eq. (5.12) and lower bound Eq. (5.13) to the mobility ratio. But in this case the weak equilibrium potential $\phi^{(0)}(\boldsymbol{r})$ allows for further simplification of the mobility ratio f_μ Eq. (5.9) and the auxiliary function $g(\boldsymbol{r})$ Eq. (5.10) which is conveniently done in Fourier space as we will presently see.

5.5.2. A linearized solution for the mobility ratio

Following Manning [162, 163] we introduce a dummy parameter λ into the equilibrium potential replacing $\phi^{(0)}(\boldsymbol{r}) \to \lambda\phi^{(0)}(\boldsymbol{r})$ and expand the auxiliary function $g(\boldsymbol{r})$ in powers of the parameter λ,

$$g(\boldsymbol{r}) = \lambda g_1(\boldsymbol{r}) + \lambda^2 g_2(\boldsymbol{r}) + \ldots\,. \tag{5.27}$$

Inserting the expansion of the auxiliary function Eq. (5.27) into Eq. (5.10) and retaining only terms up to linear order in the parameter λ we get

$$\boldsymbol{\nabla}^2 g_1(\boldsymbol{r}) = \left(\hat{\mathbf{n}}_{\boldsymbol{E}} \cdot \boldsymbol{\nabla}\right) \frac{q_{\mathrm{ct}}}{\mathrm{k_B}T}\phi^{(0)}(\boldsymbol{r}) \tag{5.28}$$

which can easily be solved in Fourier space. Accordingly we introduce Fourier expansions for the equilibrium potential $\phi(\boldsymbol{r}) = \sum_{\boldsymbol{k}} \phi_{\boldsymbol{k}} \exp(\mathrm{i}\boldsymbol{k}\cdot\boldsymbol{r})$ and the auxiliary function $g_1(\boldsymbol{r}) = \sum_{\boldsymbol{k}} g_{1,\boldsymbol{k}} \exp(\mathrm{i}\boldsymbol{k}\cdot\boldsymbol{r})$ to obtain the Fourier coefficients of the auxiliary function

$$g_{1,\boldsymbol{k}} = -\mathrm{i}\frac{\boldsymbol{k}\cdot\hat{\mathbf{n}}_E}{k^2}\phi^{(0)}_{\boldsymbol{k}}, \quad \boldsymbol{k} \neq 0\,. \tag{5.29}$$

Finally we linearize the Boltzmann factor and the auxiliary function $g(\boldsymbol{r})$ in the mobility ratio Eq. (5.9) and once again expand the equilibrium potential $\phi^{(0)}(\boldsymbol{r})$ and the auxiliary function $g_1(\boldsymbol{r})$ in Fourier series. To leading order we arrive at

$$f_\mu = 1 - \sum_{\boldsymbol{k}\neq 0} \frac{(\hat{\mathbf{n}}_E \cdot \boldsymbol{k})^2 |q_{\mathrm{ct}}\phi_{\boldsymbol{k}}/\mathrm{k_B}T|^2}{k^2}, \tag{5.30}$$

where we set the dummy parameter to $\lambda = 1$. Hence for low equilibrium potential the mobility ratio is expressed as a sum over the squared absolute values of the Fourier coefficients of the equilibrium potential $\phi^{(0)}(\boldsymbol{r})$.

The mobility ratio below the counterion condensation threshold $\xi_{\mathrm{M}} < 1$

Below the counterion condensation threshold all we need to do is to insert the Fourier coefficients of the equilibrium potential as obtained from the linearized Poisson-Boltzmann equation Eq. (5.26) in the mobility ratio Eq. (5.30),

$$f_{\mu}^{\mathrm{CC}} = 1 - \sum_{\boldsymbol{k}\neq 0} \frac{\kappa^4 (\hat{\mathbf{n}}_E \cdot \boldsymbol{k})^2 \sin(k a_{\mathrm{m}})^2}{a_{\mathrm{m}}^2 k^4 (k^2+\kappa^2)^2}\,. \tag{5.31}$$

As before the summation runs over lattice vectors $\boldsymbol{k} = (2\pi l/W, 2\pi m/W, 2\pi n/b)$ of the rectangular cell. The magnitude of the mobility ratio f_{μ}^{CC} Eq. (5.31) is regulated by the bulk counterion density and the strength of the electrostatic interactions through the Debye-Hückel screening length κ^{-1}. A substantial decrease becomes apparent only for high screening.

The mobility ratio above the counterion condensation threshold $\xi_{\mathrm{m}} > 1$

Above the counterion condensation threshold $\xi_{\mathrm{m}} > 1$ the mobility ratio f_{μ} is obtained from a weighted average of the mobility ratio of condensed counterions $f_{\mu,\mathrm{cc}}$ and uncondensed counterions $f_{\mu,\mathrm{uc}}$,

$$f_{\mu} = \theta f_{\mu,\mathrm{cc}} + (1-\theta) f_{\mu,\mathrm{uc}}\,. \tag{5.32}$$

Here $\theta = 1 - 1/\xi_{\mathrm{M}}$ denotes the fraction of condensed counterions. As stated before, when considering the mobility ratio of the uncondensed counterions CC theory involves the following replacements: (1) the PE charge q_{m} is replaced by the effective PE charge $q_{\mathrm{m}}^{*} = q_{\mathrm{m}}/\xi_{\mathrm{M}}$, (2) the counterion density $n_{\mathrm{ct},0}$ is replaced by the effective counterion density $n_{\mathrm{ct},0}^{*} = n_{\mathrm{ct},0}/\xi_{\mathrm{M}}$. In the present case this amounts to replacing the Debye-Hückel screening parameter κ in Eq. (5.31) according to $\kappa_{*}^2 \to \kappa^2/\xi_{\mathrm{M}}$. The resulting mobility ratio for uncondensed counterions reads

$$f_{\mu,\mathrm{uc}} = 1 - \sum_{\boldsymbol{k}\neq 0} \frac{(\kappa^4/\xi_{\mathrm{M}}^2)(\hat{\mathbf{n}}_E \cdot \boldsymbol{k})^2 \sin(k a_{\mathrm{m}})^2}{a_{\mathrm{m}}^2 k^4 \left(k^2 + \kappa^2/\xi_{\mathrm{M}}\right)^2}\,. \tag{5.33}$$

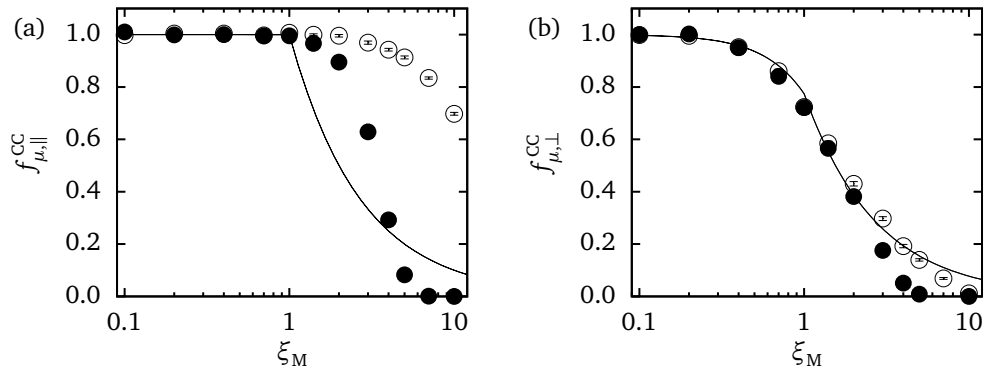

Figure 5.3.: Mobility ratio of counterions at an array of charged spheres calculated within CC theory as a function of the Manning parameter ξ_M. Lines are numerical solutions of Eqns. (5.31) and (5.35) with sphere radius $\tilde{a}_m = \sqrt{3}$, cell height $\tilde{b} = 2$, and cell width $\tilde{W} = 60$. Open symbols correspond to simulation results for model *A*, filled symbols to simulations results for model C_1. a) Parallel mobility ratio $f_{\mu,\parallel}^{CC}$. b) Perpendicular mobility ratio $f_{\mu,\perp}^{CC}$.

For condensed counterions it is assumed that *condensed counterions move as an entity with the PE chain*,

$$f_{\mu,\mathrm{cc}} \equiv 0\,. \tag{5.34}$$

This is a key assumption within Manning's theory. The total mobility ratio f_μ for Manning parameter $\xi_M > 1$ follows from Eq. (5.32) as

$$f_\mu^{\mathrm{CC}} = \frac{1}{\xi_M}\left[1 - \sum_{\boldsymbol{k}\neq 0} \frac{(\kappa^4/\xi_M^2)(\hat{\mathbf{n}}_E\cdot\boldsymbol{k})^2 \sin(ka_m)^2}{a_m^2 k^4\left(k^2+\kappa^2/\xi_M\right)^2}\right]. \tag{5.35}$$

Rewriting the Debye-Hückel screening parameter as $\kappa^2 = 4\pi\xi_M b/V$ we clearly see that the Manning parameter dependence of the mobility ratio f_μ^{CC} Eq. (5.35) is solely contained in the prefactor $(1-\theta) = 1/\xi_M$, the fraction of uncondensed counterions. Put differently, for $\xi_M > 1$ the electrofriction between uncondensed counterions and the fixed charges, that is the term in square brackets in Eq. (5.35), remains constant, whereas the mobility ratio f_μ^{CC} decreases due to the decreasing fraction of uncondensed counterions.

In Figure 5.3 we plot the mobility ratio of counterions at an array of charged spheres calculated within CC theory as a function of the Manning parameter ξ_M. In accord with our previous observation, the parallel mobility ratio rests $f_{\mu,\parallel}^{CC} = 1$ for low Manning parameter $\xi_M \leq 1$ before decreasing as

$f_{\mu,\parallel}^{CC} = 1/\xi_M$ for high Manning parameter $\xi_M > 1$. The perpendicular mobility ratio $f_{\mu,\perp}^{CC}$ is weakly decreasing for low Manning parameter $\xi_M \leq 1$ and decreasing as $f_{\mu,\parallel}^{CC} \propto 1/\xi_M$ for high Manning parameter $\xi_M > 1$. Neither direction shows a pronounced dependence on the sphere radius $\tilde{a}_m$ or the cell height $\tilde{b}$. Comparison with simulation results clearly reveals the failure of the CC theory for the parallel mobility ratio where the mobility ratio is grossly underestimated for high Manning parameter. In contrast to this, agreement between theory and simulation results is excellent in case of the perpendicular mobility ratio.

Two comments are in order. First, the *ad hoc* assumption for the mobility ratio of the condensed counterions Eq. (5.34) is disputable. In order for the condensed counterions to move with the PE chain the electrostatic potential ought to be strongly inhomogeneous. But generally speaking this is the case in perpendicular direction only. In parallel direction the charge spacing b has to be larger than the monomer radius a_m for the mobility ratio to be affected. Second, the influence of sphere radius and cell height cannot be brought out within CC theory since they are included on the linear level only.

5.6. The equilibrium potential within strong coupling theory

Within the asymptotic strong-coupling (SC) theory valid for strongly charged soft matter the electrostatic potential takes on a particularly simple form; in fact the SC potential is determined by the interaction of a single counterion with the fixed charge density [171, 172, 174, 175]. Although for homogeneously charged systems the crossover from the PB regime to the SC regime is found to be quite slow [28, 171, 175], in light of strong correlation effects in inhomogeneously charged systems [139, 140] we think the calculation of the mobility ratio from the SC potential is worth trying. The more so since at the present state it is the only possibility to include the effect of an inhomogeneous charge distribution into the mobility ratio on a non-linear level.

5.6.1. Strong coupling potential for a linear charge array

For the present discussion we simplify the cell model for the inhomogeneous charge distribution by considering a linear array of point charges. We abstain from the application of periodic boundary

conditions in all but one direction which we choose to be the z-direction. The electrostatic potential due to the charge array is given by the infinite sum

$$\phi(\boldsymbol{r}) = \frac{q_\mathrm{m}}{4\pi\epsilon\epsilon_0} \sum_{m=-\infty}^{+\infty} \frac{1}{\sqrt{r_\perp^2 + (z-mb)^2}} \tag{5.36}$$

which is clearly divergent. Convergence can be enforced, though, by introducing a constant reference potential into Eq. (5.36) according to

$$\phi(\boldsymbol{r}) = \frac{q_\mathrm{m}}{4\pi\epsilon\epsilon_0} \sum_{m=-\infty}^{+\infty} \left[\frac{1}{\sqrt{r_\perp^2 + (z-mb)^2}} - \frac{1}{\sqrt{r_{\perp,0}^2 + (z_0-mb)^2}} \right] . \tag{5.37}$$

The potential Eq. (5.37) is now convergent and equates to Eq. (5.36) up to an irrelevant constant, which depends on the choice of the reference state $\boldsymbol{r}_0 = (\boldsymbol{r}_{\perp,0}, z_0)$. Applying methods developed in Ref. [131] Eq. (5.37) can be cast into a rapidly convergent series,

$$\frac{q_\mathrm{ct}\phi(\boldsymbol{r})}{\mathrm{k_B}T} = 2\xi_\mathrm{M} \ln\left(\frac{r_\perp}{b}\right) - 4\xi_\mathrm{M} \sum_{m=1}^{+\infty} \mathrm{K}_0\left(2\pi m \frac{r_\perp}{b}\right) \cos\left(2\pi m \frac{z}{b}\right) , \tag{5.38}$$

which again equates to Eq. (5.36) up to an irrelevant constant. Here $\mathrm{K}_0(x)$ stands for a modified Bessel function of the second kind, characterized by faster than exponential decay for not too small arguments, $\mathrm{K}_0(x) \propto \mathrm{e}^{-x}/\sqrt{x}$ for $x \gg 1/4$ [176]. From the asymptotic form of the modified Bessel function we can infer that the perpendicular range of the charge inhomogeneity is given by the charge spacing b, as might have been expected. At large perpendicular separation from the linear charge array $r_\perp > b$ the charge inhomogeneity appears to be smeared out and the logarithmic potential of a line charge is recovered. Conversely, at small perpendicular separation from the linear charge array $r_\perp < b$ the charge inhomogeneity becomes noticeable and the line charge potential is modified by sinusoidal contributions. Due to the short range of the potential inhomogeneity we expect mostly the contribution of condensed counterions to the mobility ratio to be affected.

As a side effect of the rapid decay of the modified Bessel function in Eq. (5.38) discarding all but the $m = 1$ contribution of the sum already provides a quite good approximation to the SC potential,

$$\frac{q_\mathrm{ct}\phi(\boldsymbol{r})}{\mathrm{k_B}T} = 2\xi_\mathrm{M} \ln\left(\frac{r_\perp}{b}\right) - 4\xi_\mathrm{M}\mathrm{K}_0\left(2\pi \frac{r_\perp}{b}\right) \cos\left(2\pi \frac{z}{b}\right) . \tag{5.39}$$

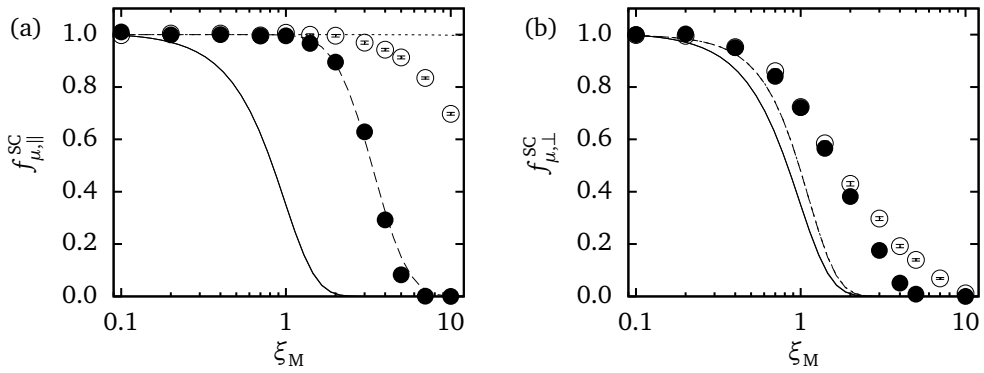

Figure 5.4.: Mobility ratio of counterions at an array of point charges calculated within SC theory as a function of the Manning parameter ξ_M. Lines are numerical solutions of Eqns. (5.14) and (5.15) using the SC potential Eq. (5.39) with a cylindrical cut-off radius $\tilde{a}_m = \sqrt{3}$, cell height $\tilde{b} = 2$ (dotted line) or cell height $\tilde{b} = 6$ (dashed line), and cell width $\tilde{D} = 60$. The solid lines denotes the lower bounds Eq. (5.15). Open symbols correspond to simulation results for model *A*, filled symbols to simulations results for model C_1. a) Parallel mobility ratio $f^{SC}_{\mu,\parallel}$. b) Perpendicular mobility ratio $f^{SC}_{\mu,\perp}$.

In Figure 5.4 we plot upper bound $f^{\text{upp}}_{\mu,\perp}$, $f^{\text{upp}}_{\mu,\parallel}$ Eq. (5.14) and lower bound $f^{\text{low}}_{\mu,\perp}$, $f^{\text{low}}_{\mu,\parallel}$ Eq. (5.15) to the perpendicular and parallel mobility ratio calculated using the SC potential of a linear charge array Eq. (5.39) as a function of the Manning parameter ξ_M. In the upper panel the radius of the enclosing cylinder is $\tilde{a}_m = \sqrt{3}$ and the charge spacing is varied from $\tilde{b} = 2$ over $\tilde{b} = 4$ to $\tilde{b} = 6$. In Figure 5.5 the radius of the enclosing cylinder is varied simultaneously with the charge spacing as ($\tilde{a}_m = \sqrt{3}, \tilde{b} = 2$) and ($\tilde{a}_m = \sqrt{7}, \tilde{b} = 6$). The cell radius is fixed at $\tilde{D} = 30$. As before, in case of the perpendicular mobility ratio the difference between upper and lower bound to the mobility ratio is small, whereas it is large in case of the parallel mobility ratio. (Remember that the lower bound to the mobility ratio is the same, regardless of the direction of the external electric field.) The perpendicular mobility ratio is independent of the charge separation b, and only marginally dependent on the radius of the enclosing cylinder a_m. As compared to the PB and CC theories, its decrease starts out earlier and proceeds more steeply, already converging to zero at $\xi_M > 2$. Clearly, this property is due to the increased attraction of counterions towards the fixed charges within SC theory. Conversely, the parallel mobility ratio (to be precise, the upper bound to the parallel mobility ratio) exhibits a pronounced dependence on the charge spacing b and the radius of the enclosing cylinder a_m. At fixed radius a_m the parallel mobility ratio decreases with increasing charge spacing b. Likewise at fixed charge spacing the parallel mobility ratio increases with increasing radius.

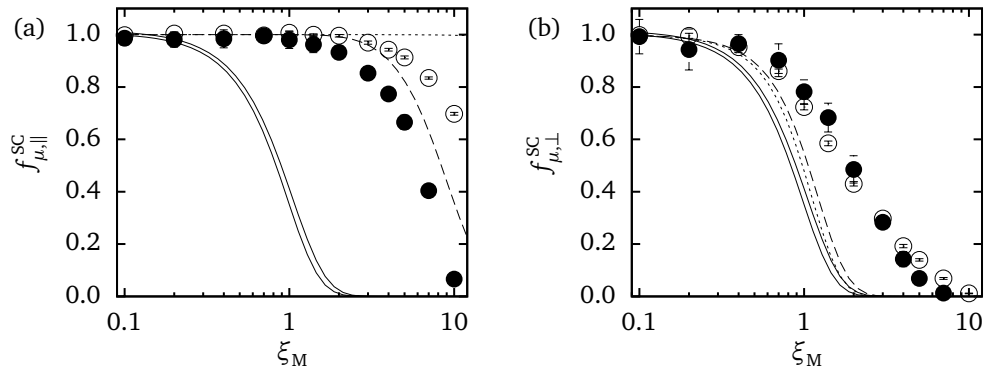

Figure 5.5.: Mobility ratio of counterions at an array of point charges calculated within SC theory as a function of the Manning parameter ξ_M. Lines are numerical solutions of Eqns. (5.14) and (5.15) using the SC potential Eq. (5.39) with a cylindrical cut-off radius $\tilde{a}_m = \sqrt{3}$ and cell height $\tilde{b} = 2$ (dotted line) or a cylindrical cut-off radius $\tilde{a}_m = \sqrt{7}$ and cell height $\tilde{b} = 6$ (dashed line). The solid lines denotes the lower bounds Eq. (5.15). The cell width is $\tilde{W} = 60$. Open symbols correspond to simulation results for model *A*, filled symbols to simulations results for model C_2. a) Parallel mobility ratio $f^{SC}_{\mu,\parallel}$. b) Perpendicular mobility ratio $f^{SC}_{\mu,\perp}$.

5.7. Non-linear response – solution in one dimension

If we reconsider the expression for the microscopic counterion current $\boldsymbol{j}(\boldsymbol{r})$ Eq. (5.1) we note, that in one dimension the microscopic counterion current is actually constant. Taking advantage of the periodicity of the local counterion density $n_{ct}(\boldsymbol{r})$ Eq. (5.1) hence can easily be integrated [177]. To this end we introduce an effective one dimensional potential $\overline{V}(z)$ defined by

$$\mathrm{e}^{-q_{ct}\overline{V}(z)} = \frac{1}{l_x l_y}\int_{l_x}\int_{l_y} \mathrm{d}x\mathrm{d}y\, \mathrm{e}^{-q_{ct}V(\boldsymbol{r})}, \tag{5.40}$$

that is we average the potential $V(\boldsymbol{r}) = \phi(\boldsymbol{r}) - zE$ over directions perpendicular to the external electric field $\boldsymbol{E} = E\,\hat{\mathbf{e}}_z$. With the effective one dimensional potential $\overline{V}(z)$ Eq. (5.40) the solution for the mobility ratio becomes

$$f_\mu = \frac{\mathrm{k_B}T}{q_{ct}l_z E}\frac{l_z^2\left(1-\mathrm{e}^{-q_{ct}l_z E/\mathrm{k_B}T}\right)}{\int_0^{l_z}\mathrm{d}z\,\mathrm{e}^{-q_{ct}\overline{V}(z)/\mathrm{k_B}T}\left[\int_0^{l_z}\mathrm{d}z\,\mathrm{e}^{q_{ct}\overline{V}(z)/\mathrm{k_B}T} - \left(1-\mathrm{e}^{-q_{ct}l_z E/\mathrm{k_B}T}\right)\int_0^{z}\mathrm{d}z\,\mathrm{e}^{q_{ct}\overline{V}(z)/\mathrm{k_B}T}\right]}. \tag{5.41}$$

The mobility ratio depends on the external electric field through the dimensionless combination $q_{ct}l_z E/\mathrm{k_B}T$ which compares the potential drop over one period of the electrostatic potential l_z with thermal en-

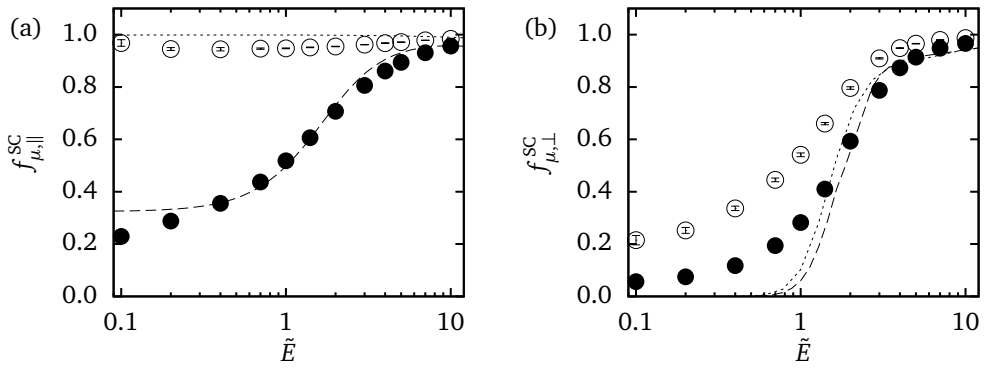

Figure 5.6.: Mobility ratio of counterions at an array of point charges calculated within SC theory as a function of the rescaled field strength $\tilde{E}$. Lines are numerical solutions of Eq. (5.41) or Eq. (5.42) using the SC potential Eq. (5.39) with a cylindrical cut-off radius $\tilde{a}_\mathrm{m} = \sqrt{3}$, cell height $\tilde{b} = 2$ (dotted line) or cell height $\tilde{b} = 6$ (dashed line), and cell width $\tilde{W} = 60$. Open symbols correspond to simulation results for model *A*, filled symbols to simulations results for model C_1. a) Parallel mobility ratio $f^{SC}_{\mu,\parallel}$. b) Perpendicular mobility ratio $f^{SC}_{\mu,\perp}$.

ergy. In the limit of low field strength $q_\mathrm{ct} l_z E/\mathrm{k_B}T \ll 1$ the mobility ratio Eq. (5.41) reduces to the upper bound to the mobility ratio Eq. (5.12). In the opposite limit $q_\mathrm{ct} l_z E/\mathrm{k_B}T \gg 1$ the mobility ratio simplifies to [177]

$$f_\mu = \frac{\mathrm{k_B}T}{q_\mathrm{ct} l_z E} \left[\frac{1}{l_z} \int_0^{l_z} \mathrm{d}z \, \frac{1}{-q_\mathrm{ct} \partial_z \overline{V}(z)/\mathrm{k_B}T} \right]^{-1} . \tag{5.42}$$

which ultimately tends to $f_\mu = 1$.

In Fig. 5.6 we plot parallel and perpendicular mobility ratio calculated using the SC potential of a linear charge array Eq. (5.39) at Manning parameter $\xi_\mathrm{M} = 4$ as a function of the dimensionless field strength $\tilde{E}$. The radius of the enclosing cylinder is $\tilde{a}_\mathrm{m} = \sqrt{3}$ and the charge spacing is varied from $\tilde{b} = 2$ over $\tilde{b} = 4$ to $\tilde{b} = 6$. The cell radius is fixed at $\tilde{D} = 30$. In both cases the mobility ratio for low field strength $\tilde{E} \ll 1$ starts out at its linear response value and increases with the field at $\tilde{E} \approx 1$ before saturating at one for high field strength $\tilde{E} \gg 1$. In case of the parallel mobility ratio onset and slope of the increase strongly depend on the charge separation $\tilde{b}$ and the cylinder radius $\tilde{a}_\mathrm{m}$. For a given Manning parameter ξ_M the onset of the increase is at lower field strength and the slope of the increase is steeper for larger charge separation $\tilde{b}$ and smaller radius a_m. These differences are less pronounced in case of the perpendicular mobility ratio. Similar to the linear response case, we find the parallel mobility ratio to be satisfactorily described within SC theory, especially at large charge

separation. SC theory fails to describe the perpendicular mobility ratio except for at high field strength when the mobility ratio has almost saturated.

5.8. Conclusion

In this Chapter we focused on the free-draining electrophoretic mobility of counterions at immobile charge distributions as a model system for the relaxation effect. By combination of a classic approximation which calculates the counterion mobility from the equilibrium electrostatic potential [24] with a recent theory for the electrostatics of strongly interacting soft matter systems, the SC theory [174], we were able to calculate the Manning parameter dependent decrease of the parallel counterion mobility at a linear charge array, where the classical CC approach fails. In case of the perpendicular mobility, where the discrete nature of the charge distribution plays a minor role, CC theory outweighs SC theory which overestimates correlations. While the failure of CC theory in case of the parallel mobility is systematic, the development of approximative solutions of the PB equation at a linear charge array could be promising for both parallel and perpendicular counterion mobility.

6. Salt-induced counterion mobility anomaly in polyelectrolyte electrophoresis

We study the electrokinetics of a single polyelectrolyte chain in salt solution using hydrodynamic simulations. The salt-dependent chain mobility compares well with experimental DNA data. The mobility of condensed counterions exhibits a salt-dependent change of sign, an anomaly that is also reflected in the counterion excess conductivity. Using Green's function techniques this anomaly is explained by electrostatic screening of the hydrodynamic interactions between chain and counterions.

Previous theoretical approaches combined mean-field electrostatics with low Reynolds number hydrodynamics. Solutions of the electrokinetic equations were obtained numerically [178] or analytically using counterion-condensation theory [129] and account for the experimentally measured salt dependent electrophoretic mobilities of biopolymers such as DNA or synthetic PEs. Counterions in the immediate vicinity of the PE chain were assumed to stick to and move along with the PE under the action of the applied electric field. This assumption becomes crucial for the conductivity of PE solutions, and indeed inconsistencies between experimental mobility and conductivity studies are documented in literature, pointing to some basic riddles in the coupling of PE and counterion dynamics in electric fields [179]. Pioneering explicit-water all-atomistic simulations of PEs in electric fields have been performed [180]. Due to the immense computational demand they are restricted to elevated field strengths, short PEs, and short simulation times. Implicit-solvent simulations have quite recently addressed the molecular-weight-dependent PE mobility in the salt-free case [124, 125] and yielded good agreement with experiments.

Outline

In the present Chapter we use coarse-grained implicit-solvent hydrodynamic simulations, cf. Chapter 2 and study the salt-dependent electrophoretic response of a single PE. By replicating the PE periodi-

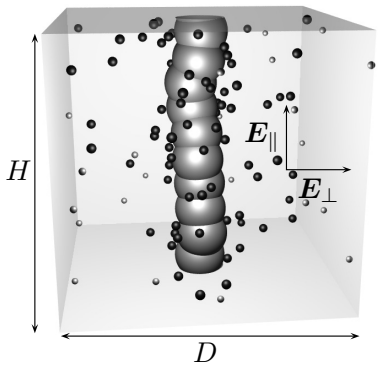

Figure 6.1.: Simulation cell for a DNA segment with counterions (dark grey) and coions (light grey). Periodic boundary conditions are applied along the projected end-to-end distance H of the DNA segment. The external electric field is applied either parallel ($\boldsymbol{E}_{||}$) or perpendicular ($\boldsymbol{E}_{\perp}$) to the PE axis.

cally we eliminate finite-chain-length effects. We concentrate on the salt-dependent interplay of PE versus counterion mobility in the infinite chain limit and show that the condensed counterion mobility changes sign as a function of salt concentration. For low salt, counterions stick to the PE and move along in the electric field in agreement with the canonic viewpoint. For high salt, on the other hand, the motion decouples and counterions move opposite to the PE. This anomaly is captured by an analytic theory developed here for weakly charged chains based on the electrostatically screened hydrodynamic interaction tensor. For DNA our simulations reproduce experimental salt-dependent mobilities without fitting parameters and predict an experimentally measurable anomaly of the counterion excess conductivity. The counterion anomaly is also directly accessible by NMR experiments [181] or PE conductivity studies in nanopores or nanochannels [182].

6.1. Modeling DNA electrophoresis

In our hydrodynamic simulations we consider a PE consisting of charged beads together with neutralizing counterions and added symmetric salt, cf. Fig. 6.1. The vertical box height H and lateral width D are fluctuating while keeping the volume HD^2 and thus the concentration of monomers c_{m}, neutralizing counterions c_{nct} and salt ion pairs c_{s} fixed.

The PE electrophoretic mobility $\mu_{\mathrm{m}} = \langle v_{\mathrm{m}} \rangle / E$ follows from the average monomer velocity along the electric field direction. In the absence of curvature, inter-chain and end effects (*i.e.* for high enough salt concentrations) and if orientation effects are negligible (*i.e.* for small electric fields), μ_{m} follows from

the parallel and perpendicular mobilities as $\mu_m = (\mu_m^{||} + 2\mu_{m,\perp})/3$. In the simulations we accordingly determine $\mu_m^{||}$ and $\mu_{m,\perp}$ separately by applying electric fields parallel and perpendicular to the PE axis and measuring the corresponding velocities. Possible non-linear effects have been carefully checked, cf. Appendix A. The ionic strength includes contributions from the neutralizing counterions and is defined as $I = (c_{nct}q_{ct}^2 + c_s q_{ct}^2 + c_s q_{co}^2)/2$.

In order to model DNA in aqueous NaCl solution at 20 °C we use Stokes radii of Na^+ and Cl^- as $a_{ct} = 1.84$ Å and $a_{co} = 1.29$ Å as obtained from limiting conductivities, an estimate of $a_m = 10.47$ Å for the DNA radius and valencies $q_{ct} = 1$, $q_{co} = -1$ and $q_m = -6$. The choice of monomer separation $b = a_m$ ensures a linear charge density of $q_m/b \simeq 0.57$ Å^{-1}. Although no bending rigidity is present in the model, the segment is sufficiently straight due to electrostatic repulsions, as appropriate for DNA (cf. Fig. 6.1). The simulation cell comprises 10 DNA monomers, 60 neutralizing counterions and 24 salt pairs. The ionic strength is varied over the range $I = 19 - 468$ mM by adjusting the cell width D. The field strengths applied are $E_{||} = 27.5 \times 10^6$ V/m and $E_\perp = 5.5 \times 10^6$ V/m. We use $\epsilon = 5$ for the LJ strength, $K/a_{ct}^2 = 100$ for the bond stiffness, and $\eta = 1.003 \times 10^{-3}$ Pa s for the viscosity of water. The Langevin time-step is $0.06 - 0.12$ ps and simulations are typically run for $0.3 - 4.1$ μs.

6.2. Counterion mobility anomaly

DNA electrophoretic mobility

In Fig. 6.2a we plot the DNA electrophoretic mobility μ_m as a function of the ionic strength, I, together with experimental data for long DNA from Refs. [106, 183]. Noting that there are no free fitting parameters and given the substantial scatter in the experimental data, we conclude that our coarse-grained DNA model is quite accurate. The mobility μ_m decreases with increasing I which will be rationalized in terms of hydrodynamic screening effects below. We additionally show theoretical results from Stigter [178] and Manning [129].

Counterion mobility

Theoretically, only little attention has been paid to electric field-induced counterion dynamics in PE solutions. In this context the phenomenon of counterion condensation at highly charged PEs that are characterized by a Manning parameter $\xi_M = q_{ct}q_m\ell_B/b > 1$ has to be taken into account. For highly

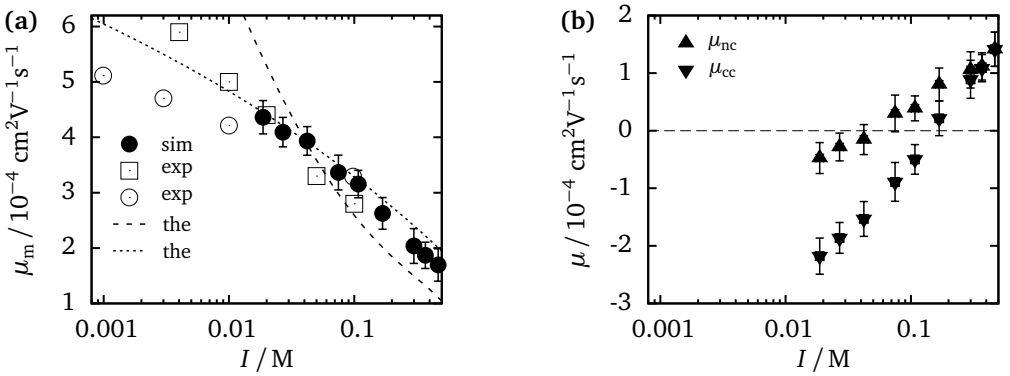

Figure 6.2.: Hydrodynamic simulations of DNA in aqueous NaCl solution of various ionic strengths I at 20 °C. a) Electrophoretic DNA mobility μ_m as obtained from simulations (filled symbols) and experiments (Ref. [183] - open squares; Ref. [106] - open circles) as a function of I, compared to theories by Stigter [178] (dashed line) and Manning [129] (dotted line). b) Mobility of neutralizing counterions μ_{nc}, and condensed counterions μ_{cc}.

charged PEs such as DNA ($\xi_M = 4.17$) electrostatic attraction of counterions towards the PE overcomes entropic repulsion giving rise to increased accumulation of counterions in the very vicinity of the PE [27, 28]. In particular, the assumption that condensed counterions stick to the PE [129, 178] has not been scrutinized, despite experimental evidence that condensed counterions are not immobilized on the PE surface [184]. In Fig. 6.2b we show the electrophoretic mobility of two counterion ensembles, first condensed counterions within a distance $r_\perp^* = a_m + 4a_{ct} = 17.8$ Å from the DNA axis (μ_{cct}) and secondly the set of counterions closest to the DNA axis that neutralize the DNA charge (μ_{nct}). At low ionic strength the hydrodynamic drag exerted by the DNA on the counterions exceeds the external electric force and the mobility for both sets is negative, *i.e.* the counterions are dragged along by the PE. At high ionic strength the hydrodynamic interactions are sufficiently screened so that the electric field dominates and the counterions move opposite to the DNA. In fact, a salt and PE charge density dependent sign reversal of the electrophoretic counterion mobility has been inferred from transference experiments some time ago [184]. Direct measurements of counterion electrophoretic mobilities can in principle be performed with pulsed field gradient NMR [181].

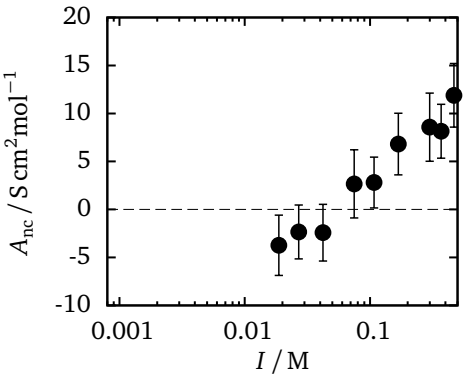

Figure 6.3.: Hydrodynamic simulations of DNA in aqueous NaCl solution of various ionic strengths I at 20 °C. Counterion excess conductivity A_{nc} according to Eq. (6.1).

Conductivity increment

We define the excess contribution of the counterions to the conductivity of a PE solution as

$$A_{nct} = (\sigma - q_m e c_m \mu_m - \sigma_s^0)/c_{nct} \tag{6.1}$$

where σ and σ_s^0 denote the specific conductivities of the salt solution with and without the PE chain, respectively. In our simulations, σ results from the separate electrophoretic contributions as $\sigma/e = q_{ct}c_{nct}\mu_{nct} - q_m c_m \mu_m + q_{ct}c_s\mu_{ct} - q_{co}c_s\mu_{co}$, while the pure electrolyte conductivity σ_0 is obtained from separate simulations as $\sigma_s^0 = q_{ct}c_s\mu_{ct}^0 - q_{co}c_s\mu_{co}^0$. As seen in Fig. 6.3, the counterion excess conductivity A_{nct} increases with increasing salt concentration and changes sign, and thus directly reflects the salt-dependent counterion mobility anomaly for the experimentally easily accessible conductivity.

6.3. Linear theory for the retardation effect

6.3.1. Solution of the Stokes equations with Debye-Hückel force distribution

To gain further insight, we now shift to weakly charged PEs (Manning parameter $\xi_M < 1$), where the ion distribution around a PE is correctly described by linear Debye-Hückel (DH) theory and the electrophoretic mobilities of PE and ions can be constructed using Green's functions [92]. The DH

ionic charge distribution around a sphere of radius a and surface charge density $q\mathrm{e}/4\pi a^2$ is for $\kappa a < 1$ given by

$$n(r) = q\mathrm{e}\frac{\delta(r-a)}{4\pi a^2} - \begin{cases} q\mathrm{e}\frac{\kappa^2 \mathrm{e}^{-\kappa(r-a)}}{4\pi r(1+\kappa a)}, & r \geq a\,, \\ 0\,, & r < a\,, \end{cases} \tag{6.2}$$

where $\kappa^{-1} = (8\pi\ell_{\mathrm{B}} I)^{-1/2}$ is the Debye screening length. At vanishing Reynolds number the stationary flow field $\boldsymbol{u}(\boldsymbol{r})$ originating from a force density $\boldsymbol{f}(\boldsymbol{r})$ acting on a viscous incompressible solvent follows from the Stokes equations,

$$\begin{aligned} \eta\Delta\boldsymbol{u} - \nabla p + \boldsymbol{f} &= 0\,, \\ \nabla\cdot\boldsymbol{u} &= 0\,, \end{aligned} \tag{6.3}$$

where η denotes the solvent viscosity, and p the pressure. In the case of a force density $\boldsymbol{f}(r) = n(r)\boldsymbol{E}$ due to an external electric field $\boldsymbol{E}$ acting on the Debye-Hückel charge distribution Eq. (6.2), the Stokes equations Eq. (6.3) can be solved in closed form. With the definition $\boldsymbol{u}(\boldsymbol{r}) =: \boldsymbol{G}(\boldsymbol{r})\, q\mathrm{e}\boldsymbol{E}$ we find for the tensor elements $G_{\alpha\beta}(\boldsymbol{r})$ $(\alpha,\beta = x,y,z)$ at distance $r < a$ from the center of the force distribution

$$G^{<}_{\alpha\beta} = \frac{\delta_{\alpha\beta}}{6\pi\eta a(1+\kappa a)}\,, \tag{6.4}$$

and at distance $r > a$

$$\begin{aligned} G_{\alpha\beta}(\boldsymbol{r}) = \frac{\mathrm{e}^{-\kappa(r-a)}}{4\pi\eta r(1+\kappa a)} \left(\frac{1+\kappa r+\kappa^2 r^2}{\kappa^2 r^2} - \frac{6+6\kappa a+2\kappa^2 a^2}{6\kappa^2 r^2}\,\mathrm{e}^{\kappa(r-a)} \right) \\ \times \left(\delta_{\alpha\beta} - 3\frac{x_\alpha x_\beta}{r^2} \right) + \frac{\mathrm{e}^{-\kappa(r-a)}}{2\pi\eta r(1+\kappa a)}\,\frac{x_\alpha x_\beta}{r^2}\,. \end{aligned} \tag{6.5}$$

Note that the no-slip boundary condition on the sphere surface is automatically satisfied. The corresponding pressure $p(\boldsymbol{r})$ at distance $r < a$ is given by

$$p^{<}(\boldsymbol{r}) = 0\,, \tag{6.6}$$

and at distance $r > a$

$$p(\boldsymbol{r}) = q\mathrm{e}\frac{(1+\kappa r)\,\mathrm{e}^{-\kappa(r-a)}}{4\pi r^3(1+\kappa a)}\,x_\alpha E_\alpha\,. \tag{6.7}$$

In the limit of zero salt $\kappa \to 0$, the Stokes solution for a translating sphere is recovered [185]. For vanishing radius $a \to 0$, Eq. (6.5) reduces to a previously derived expression [133]. Noting that Eq. (6.5) fulfills the no-slip condition on the sphere's surface, its electrophoretic mobility follows from $\mu_s = qe\, G_{xx}(r = a)$ as

$$\frac{\mu_s}{qe\mu_0} = \frac{1}{1+\kappa a}, \tag{6.8}$$

which is the classical result derived by Debye and Hückel [185]. Here $\mu_0 = 1/6\pi\eta a$ is the Stokes mobility.

6.3.2. Electrophoretic mobility of a linear chain of weakly charged spheres

To leading order in the ratio of sphere radius a and distance r the hydrodynamic coupling tensor between two spheres of charge qe and radius a located at $\boldsymbol{r}$ and at $\boldsymbol{r}'$ both moving under the influence of an external electric field $\boldsymbol{E}$ can be obtained from a multipole expansion [185] as

$$\mu_{ss}^{\alpha\beta}(\boldsymbol{r}) = qe\left(1 + \frac{a^2}{6}\nabla^2_{\boldsymbol{r}'}\right) G_{\alpha\beta}(\boldsymbol{r} - \boldsymbol{r}'). \tag{6.9}$$

The electrophoretic mobility of a charged sphere including the coupling to an arbitrary assembly of charged spheres subject to an external electric field can be calculated using Eq. (6.9) by summation over contributions from individual spheres. We proceed by using Eq. (6.9) to calculate the electrophoretic mobility of a linear chain of charged spheres extending along the z-axis under parallel or perpendicular orientation of the external electric field according to

$$\mu_{m,\parallel} = \mu_s + 2\sum_{j=1}^{\infty} \mu_{ss}^{zz}(r_\perp = 0, bj), \tag{6.10}$$

and

$$\mu_{m,\perp} = \mu_s + 2\sum_{j=1}^{\infty} \mu_{ss}^{xx}(r_\perp = 0, bj) \tag{6.11}$$

where $\mu_s = q\mathrm{e}\,G^<_{\alpha\beta}$ is the electrophoretic mobility of a single sphere, b denotes the distance between the centers of adjacent spheres, and $r_\perp$ the lateral distance from the chain axis. Within this approach closed-form expressions for the electrophoretic mobilities $\mu_{\mathrm{m},\parallel}$ and $\mu_{\mathrm{m},\perp}$ can be given according to

$$\mu_{\mathrm{m},\parallel} = \mu_s + \frac{1}{6\pi\eta\kappa^2 b^3(1+\kappa a)}\Big\{\left(6+6\kappa a+2\kappa^2a^2\right)\zeta(3) \\ -\mathrm{e}^{\kappa a}\left(6+\kappa^2a^2\right)\left[\kappa b\,\mathrm{Li}_2\left(\mathrm{e}^{-\kappa b}\right)+\mathrm{Li}_3\left(\mathrm{e}^{-\kappa b}\right)\right]\Big\} \tag{6.12}$$

and

$$\mu_{\mathrm{m},\perp} = \frac{1}{2}\left(3\mu_s-\mu_{\mathrm{m},\parallel}\right) - \frac{\mathrm{e}^{\kappa a}\left(6+\kappa^2a^2\right)\ln\left(1-\mathrm{e}^{-\kappa b}\right)}{12\pi\eta b\,(1+\kappa a)}, \tag{6.13}$$

where $\mathrm{Li}_s(z) = \sum_{k=1}^{\infty} z^k/k^s$ is the polylogarithm function, and $\zeta(s) = \sum_{n=1}^{\infty} 1/n^s$ the Riemann zeta function. Performing the orientational average $\mu_\mathrm{m} = (\mu_{\mathrm{m},\parallel} + 2\mu_{\mathrm{m},\perp})/3$ we finally get

$$\frac{\mu_\mathrm{m}}{q\mathrm{e}\mu_0} = \frac{\mu_s}{q\mathrm{e}\mu_0} - \frac{a(6+\kappa^2a^2)}{3b\,(1+\kappa a)}\,\mathrm{e}^{\kappa a}\,\ln\left(1-\mathrm{e}^{-\kappa b}\right). \tag{6.14}$$

In the limit of low screening, $\kappa a \to 0$, Eq. (6.14) decays logarithmically with increasing ionic strength as $\mu_\mathrm{m}/q\mathrm{e}\mu_0 = -2(a/b)\ln(\kappa b)$, in accord with previous results for weakly charged PEs [92, 129]. In the same fashion the perpendicular and parallel distance-dependent ion mobilities follow as

$$\mu^\perp_{\mathrm{co/ct}}(r_\perp, z) = \mu_s \pm \sum_{j=-\infty}^{+\infty} \mu^{xx}_{\mathrm{ss}}(r_\perp, z+bj) \tag{6.15}$$

and

$$\mu^\parallel_{\mathrm{co/ct}}(r_\perp, z) = \mu_s \pm \sum_{j=-\infty}^{+\infty} \mu^{zz}_{\mathrm{ss}}(r_\perp, z+bj), \tag{6.16}$$

respectively; the plus/minus sign applies to coions/counterions.

In Fig. 6.4 we compare the foregoing theoretically predicted electrophoretic mobilities of monomers and ions (obtained by summing over contributions from 23 spheres) to the hydrodynamic simulations of a weakly charged PE with Manning parameter $\xi_\mathrm{M} = 0.4$ in a field of strength $aq\mathrm{e}E/\mathrm{k_B}T = 0.2$. The simulation cell comprises 24 PE monomers, 24 neutralizing counterions and 24 salt pairs with equal radii $a_\mathrm{m} = a_\mathrm{co} = a_\mathrm{ct} \equiv a$, valencies $q_\mathrm{m} = q_\mathrm{co} = -q_\mathrm{ct} \equiv q$ and monomer spacing $b = 2a$. For intrinsically flexible PEs, the straight PE conformation in our simulations and theory is realistic only

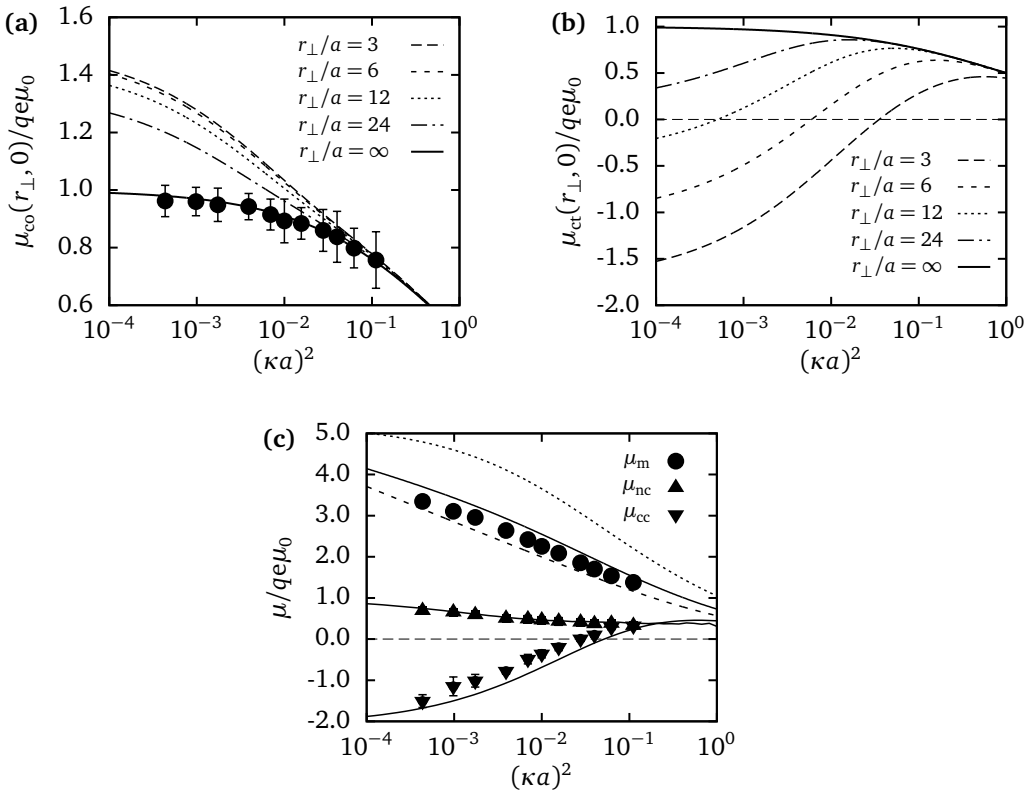

Figure 6.4.: Results for a weakly charged PE with Manning parameter $\xi_M = q_{ct}q_m\ell_B/b = 0.4$. a) Coion mobility $\mu_{co}(r_\perp,0)$ for various fixed distances $r_\perp$ from the PE as a function of $(\kappa a)^2$. The hydrodynamic drag exerted by the PE on the coions increases their mobility as compared to the case without PE, Eq. (6.14) ($r_\perp/a \to \infty$, solid line). The latter compares well with hydrodynamic simulations of a simple salt solution (filled symbols). b) Counterion mobility $\mu_{ct}(r_\perp,0)$ at distance $r_\perp$ from the PE which exhibits a sign change. For small $r_\perp$ and low salt, counterions are dragged along with the PE ($\mu_{ct}(r_\perp,0) < 0$). c) Comparison of theoretical predictions (solid lines) and hydrodynamic simulations (filled symbols) for the PE mobility μ_m, neutralizing counterion mobility μ_{nct} and condensed counterion mobility μ_{cct}. The condensed counterion mobility changes sign. We also show the parallel and perpendicular PE mobilities $\mu_m^\parallel$ (dotted line) and $\mu_m^\perp$ (short dashed line).

for low enough salt concentration as long as the effective persistence length is larger than the screening length. In Fig. 6.4a,b we show the orientationally averaged coion and counterion mobilities

$$\mu_{\mathrm{co/ct}}(r_\perp, 0) = \frac{1}{3}\left[2\mu^{\perp}_{\mathrm{co/ct}}(r_\perp, 0) + \mu^{\parallel}_{\mathrm{co/ct}}(r_\perp, 0)\right] \tag{6.17}$$

for fixed vertical coordinate $z = 0$ and various fixed distances $r_\perp$ from the PE as a function of the rescaled salt concentration $(\kappa a)^2 \sim c_s$. The mobilities of coions are increased and those of counterions are decreased by the presence of the PE. This entraining effect is larger for smaller salt concentration and smaller $r_\perp$. The ion mobilities for $r_\perp = \infty$ reflect pure electrolyte friction effects and in Fig. 6.4a compare very well with simulation results for a simple salt solution. In Fig. 6.4c we compare analytical predictions for the PE mobility μ_{m}, the neutralizing counterion mobility μ_{nct}, and the condensed counterion mobility μ_{cct} (obtained from counterions within a shell of $r^*_\perp = 5a$ around the PE) with the simulations. Here μ_{nct} and μ_{cct} are obtained from $\mu_{\mathrm{ct}}(r_\perp, 0)$ by spatially averaging over the DH counterion distribution around a straight chain of charged spheres at fixed vertical coordinate $z = 0$. With increasing salt concentration, μ_{cct} changes its sign, similar to the DNA results (cf. Fig. 6.2b). This shows that the salt-induced counterion mobility anomaly is not restricted to the non-linear regime and is fully explained by screening effects of the hydrodynamic coupling tensor.

Our simulation method neglects local solvation and DNA structural effects. The good agreement between experimental and simulation results could imply that those effects are of minor importance for the electrokinetic behavior. Nevertheless, an extension of the model to more realistic charge distributions is should be pursued.

7. Summary

The physics of PE solutions is a fascinating subject with still many open questions to answer. The aim of the present thesis is to contribute to the understanding of PE dynamics in electric fields using coarse grained BD simulations and complementary analytical calculations.

In Chapter 3 we studied the frequency dependent dielectric susceptibility for various PE concentrations and lengths. As an exiting result, we could show that the relaxation process with the smallest relaxation time is due to the relaxation of condensed counterions at a single PE chain, while the relaxation process with the largest relaxation time is related to the correlated relaxation of condensed counterions. A detailed analysis of the scaling behavior of this relaxation process has to be left for future investigations.

In close analogy to experiments which highlight the important influence of the discrete nature of the charge distribution on PE chains [20, 21] we discussed the electrophoretic response of an extended PE segment of varying charge architecture in the spirit of the cell model of PE solutions [22] in Chapter 4. In the experimentally relevant linear-response limit, we showed that the influence of the monomer-to-counterion size ratio and the charge separation indeed can be substantial, where the influence of the charge separation is strongly anisotropic. A thorough discussion of electrostatic and hydrodynamic effects was given.

The calculation of the relaxation effect for counterions at fixed charge distributions was central to Chapter 5. Electrofriction experienced by counterions moving parallel to the corrugated potential due to charged monomers could be explained using an approximation of the diffusion problem and the SC electrostatic potential.

By choosing appropriate coarse-graining parameters experimental salt-dependent DNA mobilities could be reproduced within BD simulations of the cell model in Chapter 6. The observed counterion-mobility anomaly was captured by an analytic theory developed for weakly charged chains based on the electrostatically screened hydrodynamic interaction tensor.

Parts of this thesis have been published in peer-reviewed journals, or manuscripts for such contributions are in preparation. These contributions include:

- S. Fischer, A. Naji, and R. R. Netz. Salt-Induced Counterion-Mobility Anomaly in Polyelectrolyte Electrophoresis, *Phys. Rev. Lett.* 101, 176103 (2008).
- S. Fischer, A. Naji, and R. R. Netz. Electrophoresis beyond the line charge model, *in preparation* (2009)
- S. Fischer, and R. R. Netz. Dielectric response in salt-free polyelectrolyte solutions, *in preparation* (2009)

A. Finite-size and non-linear field effects

Finite-size effects

Here we check for the finite-size scaling of the DNA electrophoretic mobility by varying the cell height H or its width D separately, while keeping the total particle concentration and hence the ionic strength $I = (c_{\mathrm{nct}} q_{\mathrm{ct}}^2 + c_{\mathrm{s}} q_{\mathrm{ct}}^2 + c_{\mathrm{s}} q_{\mathrm{co}}^2)/2$ fixed.

Changing the cell height H at constant cell width D leads to changes in the hydrodynamic cut-off in the field direction. Increasing H could potentially enhance the effect of hydrodynamic entrainment and hence the DNA electrophoretic mobility, as can be inferred from Fig. A.1 where we plot the DNA electrophoretic mobility μ_{m} as a function of the inverse cell height H^{-1}. At low ionic strength $I = 75$ mM (filled symbols) the DNA electrophoretic mobility slightly increases with decreasing inverse height. No such increase can be seen at high ionic strength $I = 299$ mM (open symbols) due to screening of hydrodynamic interactions over distances much smaller than the cell height. The vertical height $H \simeq 105$ Å used for data production in this work is shown as a vertical broken line in Fig. A.1 and is thus much larger than the typical screening length (which for the salt concentrations used is typically smaller than 20 Å) and thus gives rise to very little cell height dependence in the final data.

Varying the cell width D while keeping the cell height H fixed amounts to variations in the DNA monomer concentration $c_{\mathrm{m}} = N_{\mathrm{m}}/V$, where N_{m} is the number of DNA monomers in the simulation cell and V denotes its volume. In Fig. A.2 we show the DNA electrophoretic mobility μ_{m} as a function of the DNA monomer concentration c_{m} normalized by the concentration $c_{\mathrm{m}}^* = N_{\mathrm{m}}/H^3$ at ionic strength $I = 75$ mM and $I = 299$ mM. The DNA electrophoretic mobility is largely unaffected by variations of the monomer concentration, even though at high ionic strength the monomer concentration is quite high.

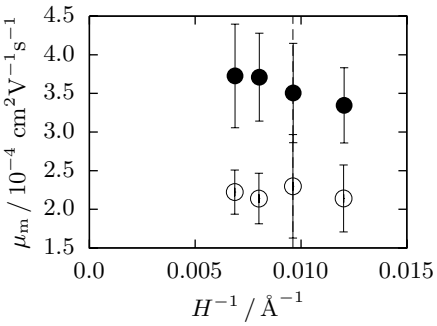

Figure A.1.: DNA electrophoretic mobility μ_m as a function of the inverse cell height H^{-1} at ionic strength $I = 75$ mM (filled symbols) and $I = 299$ mM (open symbols). At low ionic strength the DNA electrophoretic mobility decreases with increasing inverse cell height, whereas at high ionic strength the DNA electrophoretic mobility stays constant within errorbars. The vertical line at $H^{-1} = 0.0095$ Å^{-1} denotes the cell height chosen for production runs.

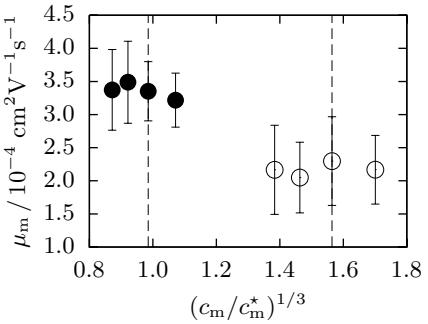

Figure A.2.: DNA electrophoretic mobility μ_m as a function of the DNA monomer concentration c_m in units of the concentration $c_m^* = N_m/H^3$ at ionic strength $I = 75$ mM (solid symbols) and $I = 299$ mM (open symbols). The DNA concentration is varied through changing the cell width D at constant cell height H. In the concentration range presented here the DNA mobility is independent of the DNA concentration within errorbars at both low and high ionic strength. The vertical lines at $c_m/c_m^* = 0.96$ and $c_m/c_m^* = 3.83$ mark the monomer concentrations chosen for production runs.

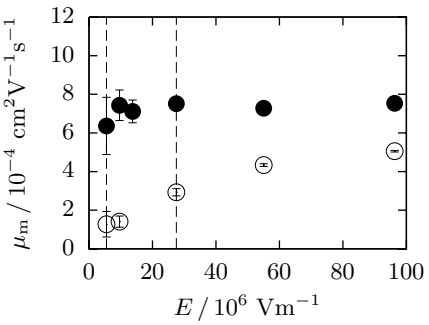

Figure A.3.: DNA electrophoretic mobility μ_m at ionic strength $I = 75$ mM as a function of parallel (filled symbols) or perpendicular (open symbols) external electric field E. For parallel field orientation the electrophoretic mobility $\mu_m^{\parallel}$ stays constant within errorbars, for perpendicular orientation the mobility $\mu_m^{\perp}$ increases with increasing field strength for $E \gtrsim 10^7$ V/m. The vertical lines correspond to $E = 5.5 \times 10^6$ V/m and $E = 27.5 \times 10^6$ V/m, which are the field strengths used for data acquisition in this work.

Non-linear field effects

In our simulations the strength of the external electric field $\boldsymbol{E}$ on the one hand has to be chosen small enough to meet the requirement of data acquisition in the linear response regime $\boldsymbol{v} \propto \boldsymbol{E}$, and on the other hand large enough to guarantee sufficient sampling of the configuration space at reasonable computational cost. In order to motivate our choice we show the DNA electrophoretic mobility μ_m as gathered from Brownian Dynamics simulations at ionic strength $I = 75$ mM as a function of the electric field strength E in Fig. A.3. The sensitivity of the electrophoretic mobility depends strongly on the orientation of the external electric field. Within the investigated range of field strengths the electrophoretic mobility under parallel orientation $\mu_m^{\parallel}$ (filled symbols) is constant within errorbars, whereas the electrophoretic mobility under perpendicular orientation $\mu_m^{\perp}$ (open symbols) increases with increasing field strength for $E \gtrsim 10^7$ V/m, *i.e.* the field dependence of the velocity becomes non-linear.

Similar behavior can be seen in Fig. A.4 where we plot the lateral radius of gyration of the neutralizing counterions

$$R_{g,nct} = \frac{1}{N_{nct}} \sqrt{\sum_{i<j} (\boldsymbol{r}_{\perp,i} - \boldsymbol{r}_{\perp,j})^2}\,, \tag{A.1}$$

where $\boldsymbol{r}_{\perp,i}$ denotes the lateral position of a counterion, and the double sum runs over the number N_{nct} of counterions closest to any DNA monomer neutralizing the DNA charge. In the linear response regime the radius of gyration of the neutralizing counterions $R_{g,nct}$ is independent of field strength

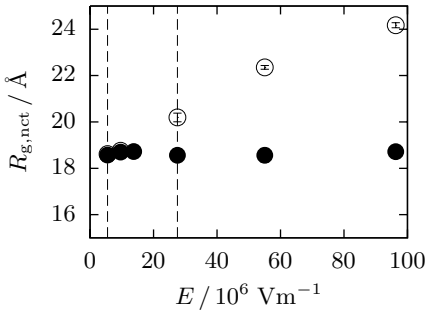

Figure A.4.: Lateral radius of gyration of neutralizing counterions $R_{g,nct}$ Eq. (A.1) at ionic strength $I =$ 75 mM as a function of parallel (filled symbols) or perpendicular (open symbols) external electric field E. $R_{g,nct}$ stays constant under parallel field orientation, for perpendicular orientation $R_{g,nct}$ increases with increasing field strength for $E \gtrsim 10^7$ V/m. The vertical lines correspond to $E = 5.5 \times 10^6$ V/m and $E = 27.5 \times 10^6$ V/m.

and orientation. For perpendicular orientation and $E \gtrsim 10^7$ V/m the radius of gyration increases with increasing field strength, that is the counterions become less tightly bound to the PE.

Concluding from the above, a convenient choice for the strength of the external electric field, which ensures the data may be gathered in the linear response regime at fair computational cost, is presented by $E_\perp = 5.5 \times 10^6$ V/m and $E_\parallel = 27.5 \times 10^6$ V/m as denoted by the vertical broken lines in Figs. A.3 and A.4, which are the field strengths used for data acquisition in this work.

Bibliography

[1] H. Dautzenberg, B. Philipp, C. Seidel, and D. Stscherbina, *Polyelectrolytes: formation, characterization, and application*, Hanser, 1994.

[2] E. Frey and K. Kroy, Ann. Phys. (Leipzig) **14**, 20 (2005).

[3] G. Gompper and M. Schick, *Soft Matter*, volume 1, chapter An Introduction to Soft Matter, Wiley-VCH, Weinheim, 2005.

[4] T. P. &. G. Company, From Pampers: Don't Spring a Leak, URL: `http://www.pg.com/science/bf_pampers.shtml`, 2009.

[5] D. Horn, Angew. Makromol. Chem. **166/167**, 139 (1989).

[6] C. Tucker and L. S. B. Goldstein, J. Bio. Chem. **272**, 9481 (1997).

[7] C. R. Calladine, H. R. Drew, B. F. Luisi, and A. A. Travers, *Understanding DNA*, Elsevier Academic Press, 3 edition, 2004.

[8] T. Tanaka and I. Nishio, Science **218**, 467 (1982).

[9] J. Lahann et al., Science **299**, 371 (2003).

[10] B. Comiskey, J. D. Albert, H. Yoshizawa, and J. Jacobson, Nature **394**, 253 (1998).

[11] N. J. Dovichi and J. Zhang, Angew. Chem. Int. Ed. **39**, 4463 (2000).

[12] D. L. Ermak and J. A. McCammon, J. Chem. Phys. **69**, 1352 (1978).

[13] W. Yu, C. F. Wong, and J. Zhang, J. Phys. Chem. **100**, 15280 (1996).

[14] R. Chang and A. Yethiraj, J. Chem. Phys. **116**, 5284 (2002).

[15] R. Chang and A. Yethiraj, J. Chem. Phys. **118**, 11315 (2003).

[16] T. Grycuk, J. Antosiewicz, and D. Porschke, J. Phys. Chem. **98**, 10881 (1994).

[17] J. Antosiewicz and D. Porschke, J. Phys. Chem. B **101**, 4478 (1997).

[18] R. R. Netz, J. Phys. Chem. B **107**, 8208 (2003).

[19] X. Schlagberger and R. R. Netz, Eur. Phys. Lett. **83**, 36003 (2008).

[20] A. Popov and D. A. Hoagland, J. Polym. Sci. B **42**, 3616 (2004).

[21] N. Anik et al., Macromolecules **42**, 2767 (2009).

[22] A. Katchalsky, Pure Appl. Chem. **26**, 327 (1971).

[23] M. Wien, Ann. Physik **83**, 327 (1927).

[24] J. L. Jackson and S. R. Coriell, J. Chem. Phys. **38**, 959 (1963).

[25] J. Rotne and S. Prager, J. Chem. Phys. **50**, 4831 (1969).

[26] H. Yamakawa, J. Chem. Phys. **53**, 436 (1970).

[27] G. S. Manning, J. Chem. Phys. **51**, 924 (1969).

[28] A. Naji and R. R. Netz, Phys. Rev. E **73**, 056105 (2006).

[29] A. Naji and R. R. Netz, Phys. Rev. Lett. **95**, 185703 (2005).

[30] C. J. F. Böttcher and P. Bordewijk, *Theory of electric polarization*, volume I, Elsevier scientific publishing company, 1978.

[31] C. J. F. Böttcher and P. Bordewijk, *Theory of electric polarization*, volume II, Elsevier scientific publishing company, 1978.

[32] S. Ikeda, H. Kumagai, and K. Nakamura, Carbohydrate Research **301**, 51 (1997).

[33] K. Ito, A. Yagi, N. Ookubo, and R. Hayakawa, Macromol. **23**, 857 (1990).

[34] Y. Katsumoto, S. Omori, D. Yamamoto, A. Yasuda, and K. Asami, Phys. Rev. E **75**, 011911 (2007).

[35] M. Mandel, Biophys. Chem. **85**, 125 (2000).

[36] A. Minakata and N. Imai, Biopolymers **11**, 329 (1972).

[37] Y. Nagamine, K. Ito, and R. Hayakawa, Langmuir **15**, 4135 (1999).

[38] Y. Nagamine, K. Ito, and R. Hayakawa, Colloids and Surfaces A **148**, 149 (1999).

[39] S. Tomić et al., Eur. Phys. Lett. **81**, 68003 (2008).

[40] S. Tomić et al., Phys. Rev. E **75**, 021905 (2007).

[41] S. Tomić et al., Phys. Rev. Lett. **97**, 098303 (2006).

[42] F. van der Touw and M. Mandel, Biophys. Chem. **2**, 231 (1974).

[43] S. Takashima, J. Mol. Biol. **7**, 455 (1963).

[44] S. Takashima, J. Phys. Chem. **70**, 1372 (1966).

[45] A. V. Dobrynin, R. H. Colby, and M. Rubinstein, Macromolecules **28**, 1859 (1995).

[46] N. Ookubo, Y. Hirai, K. Ito, and R. Hayakawa, Macromolecules **22**, 1359 (1989).

[47] F. Bordi, C. Cametti, and R. Colby, J. Phys.: Condens. Matter **16**, R1423 (2004).

[48] M. Mandel, Mol. Phys. **4**, 489 (1961).

[49] G. S. Manning, Biophys. Chem. **9**, 65 (1978).

[50] G. S. Manning, J. Chem. Phys. **99**, 477 (1993).

[51] G. S. Manning and J. Ray, Langmuir **10**, 962 (1994).

[52] J. P. McTague and J. H. Gibbs, J. Chem. Phys. **44**, 4295 (1966).

[53] A. Minakata, N. Imai, and F. Oosawa, Biopolymers **11**, 347 (1972).

[54] F. Oosawa, Biopolymers **9**, 677 (1970).

[55] F. Oosawa, *Polyelectrolytes*, Marcel Dekker, Inc., New York, 1971.

[56] S. Takashima, Biopolymers **5**, 899 (1967).

[57] F. van der Touw and M. Mandel, Biophys. Chem. **2**, 218 (1974).

[58] W. Van Dijk, F. Van der Touw, and M. Mandel, Macromolecules **14**, 792 (1981).

[59] M. Fixman, Macromolecules **13**, 711 (1980).

[60] M. Fixman, J. Chem. Phys. **72**, 5177 (1980).

[61] M. Fixman and S. Jagannathan, J. Chem. Phys. **75**, 4048 (1981).

[62] G. S. Manning, Europhys. Lett. **86**, 36001 (2009).

[63] S. Diekmann, W. Hillen, M. Jung, R. D. Wells, and D. Pörschke, Biophys. Chem. **15**, 157 (1982).

[64] C. Hornick and G. Weill, Biopolymers **10**, 2345 (1971).

[65] R. Kubo, J. Phys. Soc. Jpn. **12**, 570 (1957).

[66] A. Warashina and A. Minakata, J. Chem. Phys. **58**, 4743 (1973).

[67] J. G. Elias and D. Eden, Macromol. **14**, 410 (1981).

[68] K. Lachenmayer and W. Oppermann, J. Chem. Phys. **116**, 392 (2002).

[69] U. Mohanty and Y. Zhao, Biopolymers **38**, 377 (1996).

[70] D. C. Rau and E. Charney, Biophys. Chem. **14**, 1 (1981).

[71] M. Hogan, N. Dattagupta, and D. M. Crothers, Proc. Natl. Acad. Sci. USA **75**, 195 (1978).

[72] D. C. Rau and E. Charney, Biopphys. Chem. **17**, 35 (1983).

[73] M. Yoshida and K. Kikuchi, J. Phys. Chem. **98**, 10303 (1994).

[74] E. Washizu and K. Kikuchi, Colloids and Surfaces A: Physicochemical and Engeneering Aspects **148**, 107 (1999).

[75] E. Washizu and K. Kikuchi, J. Phys. Chem. B **110**, 2855 (2006).

[76] H. Washizu and K. Kikuchi, Chem. Phys. Lett **320**, 277 (2000).

[77] H. Washizu and K. Kikuchi, J. Phys. Chem. B **106**, 11329 (2002).

[78] J. B. Hasted, *Aqueous Dielectrics*, Chapman and Hall, 1973.

[79] S. Havriliak and S. Negami, J. Polym. Sci. **C**, 99 (1966).

[80] S. Havriliak, Jr. and S. J. Havriliak, *Dielectric and Mechanical Relaxation in Materials*, Hanser Publishers, Munich Vienna New York, 1997.

[81] R. Hilfer, J. Non-Cryst. Solids **305**, 122 (2002).

[82] K. S. Cole and R. H. Cole, J. Chem. Phys. **9**, 341 (1941).

[83] R. Metzler and J. Klafter, J. Non-Cryst. Solids **305**, 81 (2002).

[84] P. G. d. Gennes, P. Pincus, R. M. Velasco, and F. Brochard, J. Phys. (France) **37**, 1461 (1976).

[85] Y. Kalmykov, W. Coffey, and S. Titov, Physica A: Statistical Mechanics and its Applications **377**, 412 (2007).

[86] M. P. Allen and D. J. Tildesley, *Computer Simulation of Liquids*, Oxford University Press, 1988.

[87] G. S. Manning and U. Mohanty, Physica A **247**, 196 (1997).

[88] G. V. Ramanathan and C. P. Woodbury, Jr., J. Chem. Phys. **77**, 4133 (1982).

[89] M. J. Stevens and K. Kremer, Phys. Rev. Lett. **71**, 2228 (1993).

[90] M. J. Stevens and K. Kremer, J. Chem. Phys. **103**, 1669 (1995).

[91] P.-G. d. Gennes, *Scaling concepts in polymer physics*, Cornell University Press, 1979.

[92] J.-L. Barrat and J.-F. Joanny, *Theory of Polyelectroyte Solutions*, volume 94 of *Advances in Chemical Physics*, chapter 1, pages 1–66, John Wiley & sons, Inc., 1996.

[93] R. R. Netz and D. Andelman, *Encyclopedia of Electrochemistry*, chapter Polyelectrolytes in Solution and at Surfaces, pages 282–322, Wiley-VCH, Weinheim, 2002.

[94] A. Khokhlov and K. Khachaturian, Polymer **23**, 1742 (1982).

[95] J. Hayter, G. Janninck, F. Brochard-Wyart, and P. G. de Gennes, J. Physique Lettres **41**, 451 (1980).

[96] T. S. Lo, B. Khusid, and J. Koplik, Phys. Rev. Lett. **100**, 128301 (2008).

[97] R. Messina, C. Holm, and K. Kremer, Phys. Rev. E **64**, 021405 (2001).

[98] A. Tiselius, Trans. Faraday Soc. **33**, 524 (1937).

[99] A. Tiselius, *Nobel Lectures, Chemistry 1942-1962*, chapter Electrophoresis and Adsorption Analysis as Aids in Investigations of Large Molecular Weight Substances and Their Breakdown Products, Elsevier Publishing Company, Amsterdam, 1964.

[100] J. W. Jorgenson and K. D. Lukacs, Science **222**, 266 (1983).

[101] C. Heller et al., Journal of Chromatography A **806**, 113 (1998).

[102] E. Southern, Journal of Molecular Biology **98**, 503 (1975).

[103] J.-L. Viovy, Rev. Mod. Phys. **72**, 813 (2000).

[104] J. Shendure and H. Ji, Nature **26**, 1135 (2008).

[105] Q. Dong, E. Stellwagen, J. M. Dagle, and N. C. Stellwagen, Electrophoresis **24**, 3323 (2003).

[106] D. A. Hoagland, E. Arvanitidou, and C. Welch, Macromolecules **32**, 6180 (1999).

[107] U. Mohanty and N. C. Stellwagen, Biopolymers **49**, 209 (1999).

[108] E. Stellwagen and N. C. Stellwagen, Electrophoresis **23**, 1935 (2002).

[109] E. Stellwagen and N. C. Stellwagen, Biophys. J. **84**, 1855 (2003).

[110] P. D. Ross and R. L. Scruggs, Biopolymers **2**, 231 (1964).

[111] L. M. Penafiel and T. A. Litovitz, J. Chem. Phys. **96**, 3033 (1992).

[112] D. A. Hoagland, D. L. Smisek, and D. Y. Chen, Electrophoresis **17**, 1151 (1996).

[113] H. Cottet, P. Gareil, O. Theodoly, and C. E. Williams, Electrophoresis **21**, 3529 (2000).

[114] H. Cottet and P. Gareil, Electrophoresis **21**, 1493 (2000).

[115] B. Zhang, T. Hattori, and P. L. Dubin, Macromolecules **34**, 6790 (2001).

[116] R. L. Cleland, Macromolecules **24**, 4386 (1991).

[117] J. P. Meullenet, A. Schmitt, and M. Drifford, J. Phys. Chem. **83**, 1924 (1979).

[118] S. P. Strand, K. Tømmeraas, K. M. Vårum, and K. Østgaard, Biomacromolecules **2**, 1310 (2001).

[119] J. Xia, P. L. Dubin, and H. A. Havel, Macromolecules **26**, 6335 (2002).

[120] B. Staggemeier, Q. R. Huang, P. L. Dubin, Y. Morishima, and T. Sato, Anal. Chem. **72**, 255 (1999).

[121] J. Y. Gao, P. L. Dubin, T. Sato, and Y. Morishima, J. Chromatogr. A **766** (1997).

[122] L. Whitlock and L. M. Wheeler, Journal of Chromatography A **368**, 125 (1986).

[123] J. W. Klein and B. R. Ware, J. Chem. Phys. **80**, 1334 (1984).

[124] S. Frank and R. G. Winkler, Europhys. Lett. **83**, 38004 (2008).

[125] K. Grass, U. Böhme, U. Scheler, H. Cottet, and C. Holm, Phys. Rev. Lett. **100**, 096104 (2008).

[126] A. de Keizer, W. P. J. T. van der Drift, and J. T. G. Overbeek, Biophys. Chem. **3**, 107 (1975).

[127] D. Stigter, J. Phys. Chem. **82**, 1424 (1978).

[128] D. Stigter, J. Phys. Chem. **82**, 1417 (1978).

[129] G. S. Manning, J. Phys. Chem. **85**, 1506 (1981).

[130] M. Deserno and C. Holm, *Electrostatic Effect in Soft Matter and Biophysics*, chapter Cell model and Poisson-Boltzmann theory: a brief introduction, NATO Science Series, Kluwer Academic Publishers, 2001.

[131] J. Lekner, Physica A **176**, 485 (1991).

[132] R. Sperb, Mol. Simul. **20**, 179 (1998).

[133] D. Long and A. Ajdari, Eur. Phys. J. E **4**, 29 (2001).

[134] H. Hasimoto, J. Fluid Mech. **5**, 317 (1959).

[135] C. Pozrikidis, J. Eng. Math. **30**, 79 (1996).

[136] A. Bhattarai, P. Nandi, and B. Das, J. Polym. Res. **13**, 475 (2006).

[137] L. Ghimici and M. Nichifor, J. Coll. Int. Sci. **302**, 589 (2006).

[138] D. B. Lukatsky, S. A. Safran, A. W. C. Lau, and P. Pincu, Europhys. Lett. **58**, 785 (2002).

[139] A. G. Moreira and R. R. Netz, Europhys. Lett. **57**, 911 (2002).

[140] M. L. Henle, C. D. Santangelo, D. M. Patel, and P. A. Pincu, Europhys. Lett. **66**, 284 (2004).

[141] H. Falkenhagen, *Elektrolyte*, S. Hirzel Verlag Leipzig, 1953.

[142] P. M. V. Résibois, *Electrolyte Theory*, Harper & Row, 1968.

[143] Y. W. Kim and R. R. Netz, Europhys. Lett. **72**, 837 (2005).

[144] Y. W. Kim and R. R. Netz, J. Chem. Phys. **124**, 114709 (2006).

[145] R. R. Netz, Phys. Rev. Lett. **91**, 138101 (2003).

[146] G. S. Manning, J. Phys. Chem. **79**, 262 (1975).

[147] P. Ander, T. Geer, and L. Leung-Louie, Macromolecules **17**, 256 (1984).

[148] P. Ander and M. Kardan, Macromolecules **17**, 2436 (1984).

[149] P. Ander and M. Kardan, Macromolecules **17**, 2431 (1984).

[150] D. S. Dixler and P. Ander, J. Phys. Chem. **77**, 2684 (1973).

[151] R. Fernández-Prini, E. Baumgartner, S. Liberman, and A. E. Lagos, J. Phys. Chem. **73**, 1420 (1969).

[152] C. T. Henningson, D. Karluk, and P. Ander, Macromolecules **20**, 1286 (1987).

[153] J. R. Huizenga, P. F. Grieger, and F. T. Wall, J. Am. Chem. Soc. **72**, 4228 (1950).

[154] M. Kowblansky and P. Ander, J. Phys. Chem. **80**, 297 (1976).

[155] W. Lubas and P. Ander, Macromolecules **13**, 318 (1980).

[156] W. Lubas and P. Ander, Macromolecules **14**, 1058 (1981).

[157] H. Magdelenat, P. Turq, and M. Chemla, Biopolymers **13**, 1535 (1974).

[158] M. Nagasawa and S. A. Rice, J. Am. Chem. Soc. **82**, 5070 (1960).

[159] R. Trifiletti and P. Ander, Macromolecules **12**, 1197 (1979).

[160] S. Menezes-Affonso and P. Ander, J. Phys. Chem. **78**, 1756 (1974).

[161] S. Lifson and J. L. Jackson, J. Chem. Phys. **36**, 2410 (1962).

[162] G. S. Manning, J. Chem. Phys. **46**, 2324 (1967).

[163] G. S. Manning, J. Chem. Phys. **51**, 934 (1969).

[164] L. G. Nilsson, L. Nordenskioeld, P. Stilbs, and W. H. Braunlin, J. Phys. Chem. **89**, 3385 (1985).

[165] N. Yoshida, J. Chem. Phys. **69**, 4867 (1978).

[166] N. Yoshida, J. Chem. Phys. **72**, 1365 (1980).

[167] L. Gunther, M. Revzen, and A. Ron, Physica A **95**, 367 (1979).

[168] M. H. Holmes, SIAM J. Appl. Math. **50**, 839 (1990).

[169] T. Alfrey, P. W. Berg, and H. Morawetz, J. Poly. Sci. **7**, 543 (1951).

[170] R. M. Fuoss, K. A., and S. Lifson, Proc. Natl. Acad. Sci. USA **37**, 571 (1951).

[171] A. G. Moreira and R. R. Netz, Europhys. Lett. **52**, 705 (2000).

[172] R. R. Netz, Eur. Phys. J. E **5**, 557 (2001).

[173] D. Andelman, Introduction to Electrostatics in Soft and Biological Matter, in *soft condensed matter physics in molecular and cell biology*, edited by W. Poon and D. Andelman, Proceedings of the Nato ASI & SUSSP, pages 97–122, New York, 2005, Taylor & Francis.

[174] H. Boroudjerdi et al., Phys. Rep. **416**, 129 (2005).

[175] A. G. Moreira and R. R. Netz, Eur. Phys. J. E **8**, 33 (2002).

[176] M. Abramowitz and I. A. Stegun, editors, *Handbook of Mathematical Functions with Formulas, Graphs, and Mathematical Tables*, United States Department of Commerce, 1972.

[177] H. Risken, *The Fokker-Planck Equation*, Springer-Verlag, Berlin Heidelberg, 2 edition, 1996.

[178] J. A. Schellman and D. Stigter, Biopolymers **16**, 1415 (1977).

[179] D. Stigter, J. Phys. Chem. **83**, 1670 (1979).

[180] I.-C. Yeh and G. Hummer, Biophys. J. , 681 (2004).

[181] U. Böhme and U. Scheler, Macromol. Symp. **211**, 87 (2004).

[182] R. M. M. Smeets et al., Nano Lett. **6**, 98 (2006).

[183] S. L. Hartford and W. H. Flygare, Macromolecules **8**, 80 (1975).

[184] M. Nagasawa, I. Noda, T. Takahashi, and N. Shimamoto, J. Phys. Chem. **76**, 2286 (1972).

[185] S. Kim and S. J. Karrila, *Microhydrodynamics: Principles and Applications*, Dover, New York, 2005.

Danksagung

An dieser Stelle bedanke ich mich herzlich für die vielfältige Unterstützung, die mir im Verlauf meiner Promotionszeit zuteil geworden ist. Mein Dank gilt dabei besonders Herrn Prof. Dr. Roland Netz für mein interessantes Promotionsprojekt und die Begleitung meiner wissenschaftlichen Arbeit. Ein Höhepunkt meiner Promotionszeit war mein großzügig geförderter Aufenthalt in Santa Barbara, auch dafür geht mein Dank an Herrn Prof. Dr. Roland Netz. Aber vor allem unsere gemeinsamen Unternehmungen, vom Sommerfest über die Winterschule bis hin zur Weihnachtsfeier, werde ich in bester Erinnerung behalten.

Für den reibungslosen Ablauf sämtlicher verwaltungstechnischer Dinge und die Organisation unserer Social Events bedanke ich mich bei unserer Sekretärin Frau Sonja Ortner.

Ohne meine netten und hilfsbereiten Kollegen wäre meine Promotionszeit nicht halb so schön gewesen! Ich danke insbesondere Herrn Dipl. Phys. Thomas Einert für unsere gemeinsame Zeit als Zimmerkollegen an der TU München, intensive Diskussionen sowie das Korrekturlesen von Auszügen dieses Manuskripts. An Herrn Dr. Christian Sendner geht mein Dank nicht zuletzt für technische Hilfestellungen bei der Anfertigung meiner Dissertation. Ferner danke ich Herrn Dr. Andreas Serr, der in der Anfangsphase meiner Promotion ein wichtiger Ansprechpartner für mich war.

Mein besonderer Dank gilt meiner Frau Andrea und meiner Familie für ihren Rückhalt.